Nanomaterials for energy conversion and storage†

Qifeng Zhang,‡[a] Evan Uchaker,‡[a] Stephanie L. Candelaria‡[a] and Guozhong Cao*[ab]

Nanostructured materials are advantageous in offering huge surface to volume ratios, favorable transport properties, altered physical properties, and confinement effects resulting from the nanoscale dimensions, and have been extensively studied for energy-related applications such as solar cells, catalysts, thermoelectrics, lithium ion batteries, supercapacitors, and hydrogen storage systems. This review focuses on a few select aspects regarding these topics, demonstrating that nanostructured materials benefit these applications by (1) providing a large surface area to boost the electrochemical reaction or molecular adsorption occurring at the solid–liquid or solid–gas interface, (2) generating optical effects to improve optical absorption in solar cells, and (3) giving rise to high crystallinity and/or porous structure to facilitate the electron or ion transport and electrolyte diffusion, so as to ensure the electrochemical process occurs with high efficiency. It is emphasized that, to further enhance the capability of nanostructured materials for energy conversion and storage, new mechanisms and structures are anticipated. In addition to highlighting the obvious advantages of nano-structured materials, the limitations and challenges of nanostructured materials while being used for solar cells, lithium ion batteries, supercapacitors, and hydrogen storage systems have also been addressed in this review.

[a] *Department of Materials Science and Engineering, University of Washington, Seattle, WA 98195, USA. E-mail: gzcao@u.washington.edu; Fax: +1 206 543-3100; Tel: +1 206 616-9084*

[b] *Beijing Institute of Nanoenergy and Nanosystems, Chinese Academy of Sciences, Beijing, China*

† Part of the chemistry of functional nanomaterials themed issue.

‡ These authors contributed equally to this manuscript.

1. Introduction – advantages and challenges of nanomaterials for energy conversion and storage

Nanomaterials and nanostructures play a critical role in the recent advancement of some key technologies. Nanomaterials differ from microsized and bulk materials not only in the scale

Qifeng Zhang earned his PhD degree from Peking University. Currently he is Research Assistant Professor in the Department of Materials Science and Engineering at University of Washington. His research interests involve engineering nano-structured materials for applications to electrical devices, including solar cells, UV light-emitting diodes (LEDs), field-effect transistors (FETs), and gas sensors. His current research is focused on dye-sensitized solar cells (DSCs), Cu$_2$ZnSnS$_4$ (CZTS)-based thin film solar cells, quantum dot solar cells, and organic–inorganic hybrid solar cells.

Qifeng Zhang

Evan Uchaker received his B.S. from The Ohio State University in 2010, and is currently a PhD student under the supervision of Professor Guozhong Cao in the Department of Materials Science and Engineering at the University of Washington. His research interests are focused on the synthesis and characterization of nanostructured electrode archi-tectures and defect-rich materials for electrochemical energy storage devices such as Li-ion, Na-ion, and Li-air batteries.

Evan Uchaker

This journal is © The Royal Society of Chemistry 2013

Chem. Soc. Rev., 2013, **42**, 3127–3171 | **3127**

of their characteristic dimensions, but also in the fact that they may possess new physical properties and offer new possibilities for various technical applications. For example, when the characteristic dimensions of a semiconductor reduce to below a certain size, quantum confinement leads to an increased bandgap.[1,2] The bandgap can be controlled by simply varying the dimensions of the material, so the optical absorption and emission spectra can be tuned to meet the specific requirements of the desired applications.[3,4] Gold changes color to pink when the size is reduced to a few tens of nanometers due to the surface plasmon resonant absorption,[5] and finds application in enhanced surface Raman scattering.[6,7] When gold nanoparticles shrink further to less than 3 nanometers, they exhibit excellent catalytic activity due to the relatively smaller shrinkage of the d-orbitals in comparison to that of the s- and p-orbitals.[8–10]

The pervasive and wide-spread applications of nanomaterials are not necessarily due to the totally new physical properties uniquely associated with nanomaterials. The enhancement in specific surface area and associated surface energy also renders some very important applications. For example, the vapor pressure and solubility of materials change exponentially with the curvature of the surface. Nanomaterials can have solubility or vapor pressure orders of magnitude higher than their bulk counterparts,[11] so Ostwald ripening can be far more serious than in microsized materials.[12] The melting point of gold particles can be significantly lowered when the particle size reduces to the nanometer scale.[13,14] Magnetics can become superparamagnetics when the particle size reduces to the nanometer scale, corresponding to particles consisting of less than $\sim 10^5$ atoms; in such a case the surface energy becomes sufficiently large to overcome the ordering force that keeps the magnetic moments aligned.[15]

Smaller size or dimension offers a great deal of advantages and is beneficial to the advancement of existing technologies and to the exploration and development of new technologies. For example, their small size makes nanoparticles viable carriers to deliver drugs to specific targets.[16,17] The shrinking size in electronic devices has made it possible for mobile phones to serve a plethora of functions. The mechanical strength of nanomaterials is much higher than their bulk counterparts, due to the reduced number of defects.[18,19] However, the small size and large specific surface area can have adverse impacts on some applications of nanomaterials. For example, the electrical conductivity of nanowires or films with thicknesses of several nanometers can be much lower than that of their bulk counterparts due to a much shortened electron mean free path resulting predominantly from surface scattering.[20] Charge mobility in a polycrystalline semiconductor is lower than that in a single crystal, and is much lower when particles reduce to the nanometer scale.[21]

Nanomaterials offer many advantages in energy conversion and storage applications. Energy conversion and storage involve physical interaction and/or chemical reaction at the surface or interface, so the specific surface area, surface energy, and surface chemistry play a very important role. The surface impacts are not limited to the kinetics and rate only, the surface energy and surface chemistry can have appreciable or significant influences on the thermodynamics of heterogeneous reactions occurring at the interface and the nucleation and subsequent growth when phase transitions are involved. The smaller dimensions of nanomaterials may also offer more favorable mass, heat, and charge transfer, as well as accommodate dimensional changes associated with some chemical reactions and phase transitions. Nanomaterials also introduce new challenges in the application of energy conversion and storage. For example, large specific surface area offers more sites for charge recombination in photovoltaics[22,23] and smaller pores may limit the penetration of electrolyte ions in supercapacitors.[24,25]

Many excellent books and review articles have been published dealing with the fundamentals and technical approaches for the design, fabrication, and characterization of nanomaterials and nanostructures.[12,26–33] Several excellent review articles focused on specific energy-related applications of nanomaterials have been published.[34–38] Most of them have highlighted and

Stephanie L. Candelaria

Stephanie L. Candelaria earned her B.S. from the University of Arizona and is currently pursuing a PhD at the University of Washington in the Department of Materials Science and Engineering under the direction of Professor Guozhong Cao. Her research is focused on sol–gel processing and electrochemical characterization of highly porous carbon from renewable resources for supercapacitors, with particular emphasis on surface modification for improved performance.

Guozhong Cao

Guozhong Cao is the Boeing-Steiner Professor of Materials Science and Engineering, Professor of Chemical Engineering, and Adjunct Professor of Mechanical Engineering at University of Washington. He received his PhD degree from Eindhoven University of Technology, MS from Shanghai Institute of Ceramics of Chinese Academy of Sciences and BS from East China University of Science and Technology. His current research is focused on chemical processing of nanomaterials for energy related applications including solar cells, lithium-ion batteries, supercapacitors, and hydrogen storage.

demonstrated the uniqueness and advantages of nanomaterials in energy conversion and storage applications. This review article takes a few selected topic fields and focuses on the relatively recent progress in those fields, to highlight the most recent developments and the promise and limitations of nanomaterials in energy conversion and storage applications. It is the intention of the authors to provide the reader with complementary information and slightly different perspectives on nanomaterials for energy conversion and storage applications.

Specifically, the topics that will be discussed in this review article include (1) nanostructured inorganic materials for photovoltaics, (2) nanostructured electrodes for lithium ion batteries, (3) nanomaterials for supercapacitors, and (4) nanocomposites for hydrogen storage. One of the reasons these four topics were chosen for this review is the relative familiarity of the authors with these fields. Another reason is that these four fields deal with different fundamental and technical challenges, but are connected by the common use of nanostructured materials to form electrodes for electron/mass transport under an electrochemical environment involving solid–liquid interfaces.

Nanostructured inorganic materials for photovoltaic applications such as dye-sensitized solar cells and quantum dot-sensitized solar cells are typically required to have a large specific surface area so that sufficient dye molecules and quantum dots can be adsorbed onto the inorganic materials, serving as an antenna for optical absorption. The surface chemistry must be such that the dyes or quantum dots can be adsorbed favorably to form closely packed conformal monolayers, not only for maximizing photon capture, but also for minimizing the interface charge recombination. The nanostructured inorganic network must possess excellent charge mobility and long lifetime, and possibly possess some light scattering or photon trapping capability. Perfect crystallinity and minimal surface and bulk defects are desired, and the grain boundaries connecting individual nanostructures should be controlled to be as low as possible.

Nanostructured materials as electrodes for lithium ion batteries should offer a set of properties or characteristics including large specific surface area for fast interfacial *Faradaic* reaction, small distance for mass and charge transport, and small dimensions to accommodate the volume change accompanied with lithium ion insertion and extraction. However, in order to achieve high energy and power density as well as long cyclic life, nanostructured electrodes should possess more open space to accommodate more guest ions and to allow the ions to diffuse effectively; for a given chemical composition, an amorphous material may be better-suited than its crystalline counterpart, and electrodes with perfect crystallinity may be less desirable than poor crystallinity. High energy facets and surface defects may promote and catalyze the interfacial reactions and phase transitions. Bulk defects may enlarge the lattice constants and enhance the electrical conductivity. Nano-carbon coating may not only enhance the electrical conductivity of the electrode, but also introduce surface defects that promote the interfacial *Faradaic* reactions and phase transitions.

Porous nanomaterials have been used and commercialized in electric double layer capacitors (EDLCs), or supercapacitors. The capacitance is directly proportional to the total surface area, so nanopores are desirable to achieve high specific surface area; however, the small pores or apertures may exclude electrolyte ions from penetrating, or at least impose significant diffusion resistance, leading to a low power density. Impurities in porous materials can be detrimental, as they may react with the electrolyte to degrade the cyclic stability; however, other impurities may enhance the surface charge density and thus high capacity can be achieved.

Hydrogen storage in solids has different challenges: high dehydrogenation temperature, reversibility, and thermal management, just to name a few. Nanostructured materials can affect the dehydrogenation temperature and manipulate the reaction mechanisms. Appropriately designed and fabricated nanocomposites can have desired thermal conductivity to mediate the heat released or absorbed during the hydrogenation or dehydrogenation process.

This review summarizes some of the important aspects and latest developments regarding applications of nanostructured materials for energy conversion and storage in the fields mentioned above. It will be shown that the most outstanding advantage of nanostructures is their ability to create architectures with significantly larger internal surface area in view of their nano-scaled size. This feature of nanostructures enables them to be suitable for use in devices such as dye-sensitized solar cells, lithium ion batteries, supercapacitors, and hydrogen storage systems. All of these applications involve a chemical reaction that takes place at either a solid–liquid interface or a solid–gas interface. Therefore, a larger interface results in an active material with a stronger ability to induce the reaction. Besides providing large surface area, it will be shown that nanostructures have other specific merits when used for energy-related devices. For example, one-dimensional nanostructures, including nanowires/nanorods and nanotubes, have demonstrated the ability to serve as antireflection layers in solar cells and give rise to highly efficient electron transport, especially in dye-sensitized solar cells and polymer solar cells. Metal nanoparticles may generate surface plasmon resonance, and thus enhance the optical absorption of all types of solar cells. Quantum dots are a promising type of nanostructure that may potentially lead to solar cells with internal conversion efficiencies over 100% owing to the multiple exciton effect. In regard to lithium ion batteries, it will be shown that recently developed micro/nano-structures and hollow structures exhibit enhanced lithium ion intercalation capability and surface permeability in view of their distinct geometrical characteristics that facilitate electrolyte diffusion and electron/ion transport while offering a large surface area. Mesocrystals, which are a relatively new structure comprised of crystallographically oriented nanoparticles, show great promise in creating high-performance lithium ion batteries because of their more prevalent and uniform pores, compared to traditional nanoparticle films, that can ease lithium ion intercalation by decreasing the diffusion distance. Surface modification and the utilization of

defects, which are fairly new concepts to lithium ion batteries and still require further understanding, may controllably create nucleation sites at the electrode–electrolyte interface so as to promote phase transitions between the redox and charge/mass transfer processes, thus enhancing the efficiency and cycling performance of lithium ion batteries. This review will also introduce new developments in the fields of supercapacitors and hydrogen storage that employ nanostructures such as carbon nanotubes, graphene, porous conducting polymers, and metal–organic frameworks. In supercapacitors, besides the similar aforementioned effects on lithium ion batteries to provide high surface area, these nanostructures give rise to easy access for electrolyte to the active material and short diffusion distance, leading to improved energy storage. Hydrogen storage systems benefit from the use of nanostructured materials as a result of the reduced gravimetric and volumetric storage densities and additional binding sites provided by the nanostructures on the surface and within pores.

This review is composed of six sections. Section 1 gives a general introduction regarding the advantages and challenges of nanostructured materials for energy conversion and storage applications. Section 2 summarizes the applications of nanostructures in solar cells, including the multiple exciton effect of quantum dots, large internal surface area of nanocrystalline films for dye-sensitized solar cells, optical effects such as antireflection by one-dimensional nanostructures, surface plasmon resonance of metal nanoparticles, light scattering with nanocrystallite aggregates and mesoporous beads, and electron transport enhancement using one-dimensional nanostructures and three-dimensional H–P–G core–shell structures. Section 3 introduces several new nanostructures for application in lithium ion batteries, for example, spherical micro/nanostructures assembled from nanosheets, hollow nanostructures such as hollow particles, silicon nanotubes, and encapsulated nanoparticles, as well as mesocrystals of TiO_2, V_2O_5, and $LiFePO_4$. Surface modification and the manipulation of defects are also introduced as an innovative direction towards improving lithium ion battery performance. Sections 4 and 5 introduce several porous nanomaterials for applications in supercapacitors and hydrogen storage, respectively, including high surface area porous carbon, carbon nanotubes and graphene, porous conducting polymers, nanostructured metal oxides, and other carbon-based porous materials and composites. Section 6 gives general remarks, and is provided to address several important aspects and challenges that are presented in the current study of nanomaterials for energy conversion and storage applications.

The motivation of this review is to demonstrate that the performance of devices, for example the energy-related devices discussed here, is closely related to the structure of the materials, and to prove that attentive design of the structure may enable the materials to have desired function(s) or generate new mechanisms that can enhance the overall device performance. In each section, the limitations and challenges of nanostructured materials for specific applications have been outlined.

2. Nanostructured materials for solar cell applications

The basic design principle for solar cells is to increase the optical absorption of the active layer and/or reduce the electron loss during transport. Nanostructures can be employed to improve the performance of solar cells by (1) bringing about new mechanisms, such as the multiple exciton generation effect in quantum dots, (2) providing large surface area, like the nanocrystalline films used for dye-sensitized solar cells, (3) generating unique optical effects to either reduce the light loss or enhance the optical absorption, based on the methods of antireflection, surface plasmon resonance, or light scattering for example, and (4) improving the electron transport and/or collection through the use of one-dimensional nanostructures or purposely designed three-dimensional structures, such as host–passivation–guest hollow core–shell spheres. The motivation of this section is to show that the tailoring of materials to optimize light harvesting and electron transport is an effective means of creating high performance solar cells.

2.1 Quantum dots delivering new mechanisms for photovoltaics

Quantum dots are exceptionally small semiconductor nanocrystals with dimensions comparable to the Bohr radius of an exciton given by $r_{exciton} = (\varepsilon m_0/m^*)r_0$, where ε is the relative dielectric constant of the semiconductor material, m_0 is the mass of a free electron, m^* is the reduced effective mass defined by $1/m^* = 1/m_e + 1/m_h$ (where m_e and m_h are the electron and hole effective masses, respectively), and r_0 is the Bohr radius of the hydrogen atom equalling 0.529 Å.[39,40] For most semiconductors, the Bohr radius of the exciton is in the range of 1–10 nm – for example, 4.2 nm for Si, 3.1 nm for CdS, 6.1 nm for CdSe, and 2.2 nm for ZnO. However, the excitonic Bohr radii are relatively large for some semiconductors, as exemplified by 20.4 nm for PbS, 46 nm for PbSe, and 67.5 nm for InSb.[41–44] As a result of the structural characteristics of quantum dots, i.e., their dimensions are comparable to the excitonic Bohr radius of the semiconductor, the behavior of electrons in quantum dots differs from that in the corresponding bulk material, giving rise to the so-called *quantum confinement effect*. A semiconductor with a larger excitonic Bohr radius means that the quantum dots made from the material may achieve a strong confinement effect more easily.

The most common phenomenon arising from the quantum confinement effect is that the energy band gap of a quantum dot, E_g, is dependent on the particle size, which can be elucidated by $E_g \propto 1/r^2$, where r is the radius of the quantum dot. The size-dependent effect originates from the discretization of the energy levels in a semiconductor while its dimensions are smaller than the excitonic Bohr radius corresponding to the semiconductor. Such a feature of the quantum dots with tunable band gap has led to their applications in light emitting diodes (LEDs) for full-color displays,[45,46] and in quantum dot-sensitized solar cells for the generation of optical absorption at desired wavelengths (Table 1). CdS and CdSe are the materials that have been most extensively studied for quantum dot-sensitized solar cells, in

Table 1 Main achievements in quantum dot-sensitized solar cells with efficiency greater than 4%[48]

Configuration	Counter electrode	Electrolyte	Efficiency (%)
TiO_2 + CdS/CdSe/ZnS	CuS/CoS	2 M Na_2S, 0.5 M S and 0.2 M KCl in MeOH–H_2O (3 : 7 v/v)	4.1
TiO_2 + CdS/CdSe/ZnS	Sputtered Au	0.5 M Na_2S, 0.125 M S and 0.2 M KCl in MeOH–H_2O (3 : 7 v/v)	4.22
TiO_2 + CdSe/ZnS	Carbon	0.5 M Na_2S, 0.5 M S and 0.1 M KCl in MeOH–H_2O (3 : 7 v/v)	4.36
TiO_2 + CdS/CdSe/ZnS	Cu_2S	1 M S and 1 M Na_2S	4.92
TiO_2 + Sb_2S_3	Au	Poly(3-hexylthiophene)	5.06

which the quantum dots acting as sensitizer adsorb on a porous oxide nanocrystalline film to harvest light and inject electrons into the oxide. For quantum dot-sensitized solar cells, smaller quantum dots are preferred in order to possibly achieve more quantum dots adsorbed on the photoelectrode film. Smaller quantum dots have also demonstrated a higher electron injection rate than their larger counterparts.[47] However, too small quantum dots would lead to too much of a blue shift to the absorption edge and therefore lower the optical absorption of the photoelectrode film, bringing about negative impacts on the solar cells. The best solar-to-electricity conversion efficiency can be reached by optimizing both the porous structure of the oxide film and the adsorption status of the quantum dots. To this end, different fabrication methods have been investigated, mainly including successive ionic layer adsorption and reaction (SILAR), chemical bath deposition, electrochemical deposition, electrophoresis, and linker-assisted binding, or a combined use of these methods. With the CdS and CdSe quantum dot-sensitized TiO_2 nanocrystalline film passivated by ZnS and using Cu_2S as the counter electrode and an aqueous solution containing 1 M S and 1 M Na_2S as the electrolyte, an efficiency as high as 4.92% has been reported.[49] The record efficiency to date, $\sim$5.06%, was achieved with Sb_2S_3-sensitized TiO_2 nanocrystalline film, using sputtered Au film as the counter electrode and poly(3-hexylthiophene) (P3HT) as the hole transport layer.[50]

While the size-dependent effect of quantum dots is currently being extensively studied, another effect, which is thought to be more significant to solar cells, is the so-called multiple exciton generation (MEG) effect (or "carrier multiplication" (CM)). The MEG effect describes the generation of two or more excitons with one photon excitation, in contrast with the conventional case where one photon excitation can only produce a single electron–hole pair (or exciton) (Fig. 1a and b). The MEG effect is a phenomenon that can also be observed in a bulk material, however the required threshold for the energy of photons is much higher than that in the case of quantum dots. For example, for the semiconductor PbSe, the threshold energy for bulk material is as high as $6.5E_g$, whereas it is about $3.4E_g$ for PbSe quantum dots, where E_g is the energy band gap of the PbSe. (Fig. 1c).[51,52] The reasons that the MEG effect can be more easily achieved in quantum dots have been attributed to (1) the reduced cooling rate of hot-electrons in the quantum dots in view of discrete energy levels which enables the occurrence of a reversed Auger recombination process, known as impact ionization, and results in the generation of secondary electron–hole pair(s) (e^-–h^+), (2) strong carrier confinement in the quantum dots which increases the e^-–h^+ Coulomb interaction
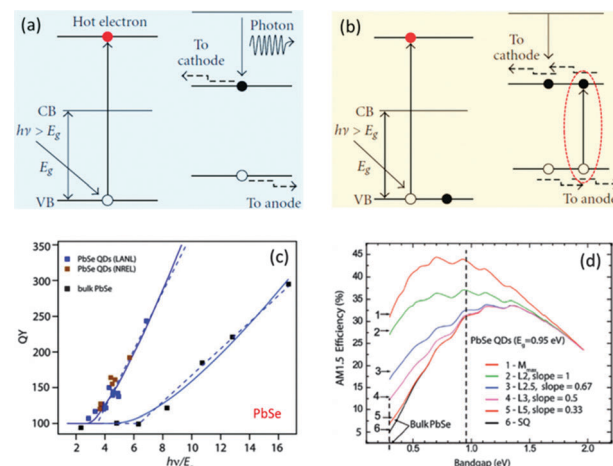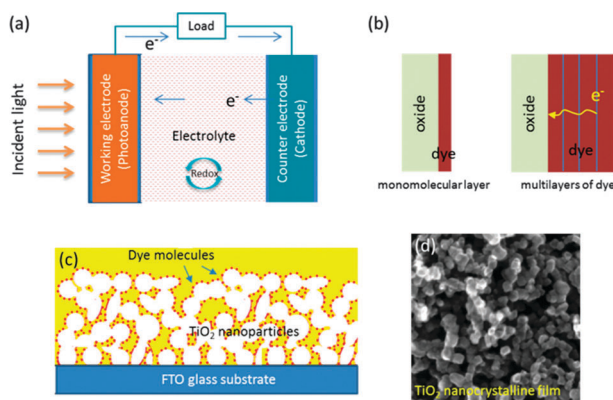

Fig. 1 MEG effect of quantum dots. (a) Photoexcitation in a bulk semiconductor that generates a single electron–hole pair and (b) in a quantum dot exhibiting the MEG effect,[55] (c) a comparison of the threshold energy of photons for the generation of multiple excitons in the quantum dots and bulk material, and (d) theoretical prediction of the maximum efficiency of quantum dot solar cells.[51] Reprinted with permission from ref. 51. Copyright 2010 American Chemical Society.

and thus facilitates the reversed Auger process resulting from the mechanism mentioned in (1), and (3) uncertain momentum in the quantum dots resulting from the momentum not being a good quantum number for three dimensionally confined carriers.[51–55]

Taking the MEG effect into account, the maximum efficiency for quantum dot solar cells has been predicted to be as high as $\sim$42% (Fig. 1d),[51,56,57] which is a value much higher than the Shockley–Queisser Efficiency Limit, $\sim$31%, for any type of bulk semiconductor-based single junction solar cell.[58] In an experimental study done by Semonin et al., an external quantum efficiency over 100% has been observed on a p–n junction solar cell based on a layer of p-PbSe quantum dots deposited on an n-ZnO thin film.[59] However, the achievement of quantum dot solar cells with MEG effect enhancement is still facing a huge challenge at the present time, partially because the excitation of the MEG effect requires photons with relatively high energy and a pump light with high power density, which natural sunlight cannot well match. There are a large number of reports appearing in the literature under the designation of "quantum dot solar cells", most of which however use the quantum dots to either form a semiconductor film serving as the active layer of the cells or act as the photosensitizer in quantum dot-sensitized solar cells to harvest the light; in either case the quantum effect is not fully involved. This lack of investigation, however, in turn leaves great opportunities for research work regarding this topic.

2.2 Nanocrystalline films providing large surface area

The evolution of dye-sensitized solar cells (DSCs) well exemplifies that solar cells can greatly benefit from the use of nanostructures while forming a film, which may provide significantly higher internal surface area than bulk material. DSCs are a type of photoelectrochemical system for solar-to-electricity conversion, which typically includes a working electrode (*i.e.*, photoanode) for light harvesting and charge separation, a counter electrode (*i.e.*, cathode) to transport the electrons received from an external circuit, and an electrolyte filled between the two electrodes that provides redox couples allowing for reduction of the photoanode (Fig. 2a). During the initial development of DSCs, the photoanode was made of a narrow band-gap semiconductor with the expectation of absorbing visible light. However, due to a small interface formed between the semiconductor photoanode and the electrolyte, the cells only achieved efficiencies in the range of 0.4–1%. Moreover, the semiconductor was found to suffer from severe corrosion due to a reaction with the electrode under operating conditions. This, in turn, inspired the use of wide band-gap oxides for the photoanode on which a layer of dye was coated as sensitizer for light harvesting and consequently transferring the electrons to the oxide (Fig. 2b). This development solved the corrosion problem since the oxides were much more stable when undergoing the photoelectrochemical reaction. However, efficiencies in the range of 2–3% achieved in the 1960s to 1980s were still quite low, although dye materials with broad absorption spectra had been developed while oxide films with rough surfaces had been adopted to increase the photoanode–electrolyte interface.[60] Increasing the thickness of dye adsorbed on the oxide also proved unsuccessful, since a multilayer adsorption of dye might indeed increase the optical absorption but the electron transport became very difficult, leading to the additionally adsorbed dye making no further contribution to the electron injection from the dye to the oxide (Fig. 2b).

An unprecedented breakthrough on DSCs was made by Grätzel *et al.* in 1991 by employing a TiO$_2$ nanocrystalline film combined with a ruthenium-based dye for photoanodes; the cell yielded 7.12% efficiency.[61] Of course, the inclusion of the ruthenium-based dye, which was newly developed and presents a high extinction coefficient and broad absorption spectrum to ~650 nm wavelength, is one of the reasons that led to such a breakthrough. However, a more important contribution derives from the extremely large internal surface area provided by the nanocrystalline film consisting of ~15 nm sized nanoparticles (Fig. 2d). It was demonstrated that the internal surface area for such a nanocrystalline film with 1 cm^2 geometric area and 10 μm thickness was as high as ~780 cm^2, meaning an ~780-fold increase in the adsorption area when compared to a planar film. As a result, the light absorption of the dye-sensitized nanocrystalline film was ~46%, in comparison with less than 1% for a planar film sensitized with the same dye. In addition to the large internal surface area offered by the nanocrystalline film, on the materials side, anatase TiO$_2$ nanoparticles with exposed (101) facets, which allow the dye molecules to form highly dense monolayer adsorption and inject electrons highly efficiently, were also thought to be an important reason for this success.[62]

Many other nanostructures besides TiO$_2$ nanoparticles, including nanoparticles, nanowires/nanorods, nanotubes, and core–shell structures of oxides such as ZnO, SnO$_2$, Nb$_2$O$_5$, and so on, have also been extensively studied for DSCs since 1991, with the expectations of not only providing a large internal surface area to the photoelectrode film, but also giving rise to other functions to enhance the optical absorption or electron transport.[64–66] Nevertheless, to date, the efficiency records of ~11–12% for DSCs are still held by TiO$_2$ nanocrystalline film in association with highly efficient dyes and optimal device structure.[67–69] Current investigations in the field of DSCs are mainly focused on the development of (1) organic dyes with higher extinction coefficient and broader absorption spectrum, and (2) advanced structures for the photoelectrode film to maximally reduce the charge recombination; charge recombination in DSCs results from the high-level exposure of the nanoparticles to the electrolyte, however it is an essential structure for the DSCs in order to give rise to large internal surface areas for dye adsorption and simultaneously allow highly efficient transport of the iodide ions (I$^-$) in the electrolyte for the reduction of photoexcited dye molecules.

2.3 Nanostructures giving rise to unique optical effects

Utilization of optical effects is an important aspect for the application of nanostructures in solar cells. According to the design principles for solar cells, *i.e.*, possibly increasing the optical absorption and reducing light loss, nanostructures have been employed to improve the performance of solar cells through, for example, the following ways: (1) serving as an *antireflection* layer to reduce the loss of incident light at the front interface of solar cells, (2) generating *surface plasmon resonance*, or (3) causing *light scattering* to enhance the optical absorption of the active layer in DSCs.

2.3.1 Antireflection. Reflection of light at the front interface of a solar cell may lead to as high as 30% loss of the incident light.

Fig. 2 Dye-sensitized solar cell (DSC). (a) The structure of a DSC, (b) dye adsorption on oxide and electron injection from dye to oxide, (c) schematic drawing showing the structure of a DSC photoelectrode film made of nanoparticles, and (d) SEM image of TiO$_2$ nanocrystalline film used in conventional DSCs.[63] Reprinted from *Journal of Photochemistry and Photobiology C: Photochemistry Reviews*, Volume 4, Issue 2, Michael Grätzel, Dye-sensitized solar cells, Pages 145–153, Copyright 2003, with permission from Elsevier.

3132 | *Chem. Soc. Rev.*, 2013, **42**, 3127–3171

This journal is © The Royal Society of Chemistry 2013

The use of an antireflection coating layer is one way of reducing the reflection of light to allow more light to transmit into the solar cell. Conventional methods for antireflection include the deposition of a single layer of antireflection film, for example MgF_2, with a quarter-wavelength thickness, or multilayer films with intentionally designed refractive indices and thicknesses to minimize the light reflection. The use of single-layer antireflection has been demonstrated to be able to lower the reflection from $\sim 30\%$ to $\sim 10\%$, while multilayer antireflection may achieve much more. However, the former is only effective for light with a certain wavelength, depending on the thickness of coating layer (the so-called "V-coating" in the literature reflects the shape of the reflectance spectrum with single-layer antireflection); moreover, a single-layer antireflection coating cannot completely eliminate reflection due to the difference in the reflection capability at the front and back interfaces of the coating layer. Multilayer antireflection may reduce the reflection in a broad spectrum range and work much more efficiently than single-layer antireflection. However there is a scarcity of materials that can fully meet the specific refractive index requirement, and the manufacturing of multilayer antireflection results in solar cells with high cost. In addition, both single-layer antireflection and multilayer antireflection involve a high temperature treatment during film deposition, which usually brings about unwanted element diffusion and thus causes degradation of the solar cell film. In this regard, the use of nanostructures for antireflection, which is both cost-effective and highly efficient in a broad spectrum range, has been attracting more and more attention over the past decade.

Antireflection using nanostructures can be achieved by growing a layer of tapered nanowire array or micro-sized hemispheres on the surface of the solar cell film. The mechanism of nanostructure-induced antireflection is that these nanostructures, with intervals on the sub-wavelength scale, function as optical gates to diffract the incident light. The tapered nanowire structure or hemisphere shape of the individual nanostructures results in a graded porosity distribution (or volume fraction) to the antireflection layer comprised of the nanostructures. Therefore, according to the *Effective Medium Theory*, the effective dielectric constant of the antireflection layer would be of a graded distribution from the top to the bottom. This accordingly results in a graded refractive index within the antireflection layer, which increases from 1 (corresponding to the refractive index of air) to the refractive index of the substrate, which is 3.8 for silicon (Fig. 3).[70] That means the nanostructures deposited on solar cell films function like a multilayer film with a gradually varied refractive index, ideally enabling the incident light to completely transmit into the solar cell film.

Tang *et al.*[70] and Nishioka *et al.*[73] reported a silver-catalyzed method for the fabrication of a tapered nanowire array on a silicon substrate based on a chemical etching process. In this method, silver nanoparticles were first deposited on the silicon substrate. The etching was performed by adding an aqueous solution containing HF and H_2O_2 on the silver nanoparticle-coated silicon substrate. Because the etching was only reactive to the exposed silicon where there was an absence of silver
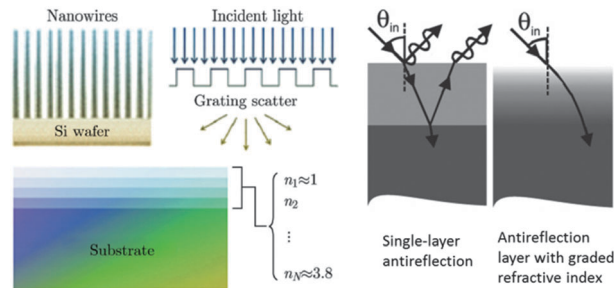

Fig. 3 Nanostructure for antireflection with graded refractive index.[70,71] Reprinted with permission from ref. 71. Copyright 2009, Wiley-VCH.

nanoparticles, such a treatment resulted in the formation of a nanowire array. It was hypothesized that the resultant silicon nanowires with tapered structure were a result of the gradually decreased concentration of H^+ in the etching solution as the etching proceeds. A 60 min etching led to the formation of 3 µm long nanowires; with them, the reflectance of the solar cell film significantly lowered, from more than 25% (in the case of no antireflection layer) to approximately 2.5% in the spectrum range from 400 nm to 1000 nm.[70] Jung *et al.* demonstrated that, after the silver-catalyzed etching, further treatment of the bunched silicon nanowire array with a KOH solution for about 60 s might lead to the formation of more tapered nanowires, which further lowered the reflectance to be less than 1% (Fig. 4a–c), resulting in an efficiency increase from 3.62% to 6.56% for silicon-based p–n junction solar cells (Fig. 4d).[72]

Chlorine (Cl_2)-based selective and anisotropic reactive ion etching (RIE) is another important method that may create cone-shaped silicon nanowire arrays. The advantage of the RIE method is that SiO_2 nanoparticles in addition to noble metal or alloy[75] nanoparticles can serve as the etching mask for the creation of silicon nanocone arrays.[74,76,77] This advantage is believed to be greatly significant from the point of view of lowering the cost of manufacturing. In the RIE method, the diameter and spacing of the nanocones are determined by the size of initial nanoparticles, their distribution density on the silicon substrate, and the etching time. The formation of cone-shaped nanowires was due to the re-deposition of the produced silicon during etching, enabling the etching rate to decrease from the top to the bottom of the nanowires. Zhu *et al.* studied the refractive index dependence on the depth of an
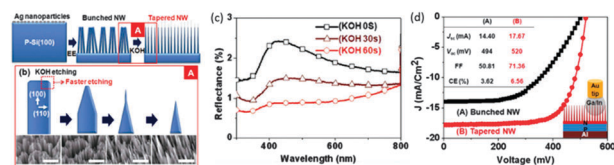

Fig. 4 Tapered silicon nanowire array for antireflection in silicon solar cells. (a), (b) Schematic drawings showing the formation of tapered silicon nanowires catalyzed by silver nanoparticles followed by a KOH treatment, (c) decrease of reflectance with increasing etching time, and (d) improved solar cell efficiency due to enhanced antireflection using tapered nanowires.[72] Reprinted with permission from ref. 72. Copyright 2010, The Optical Society (OSA).
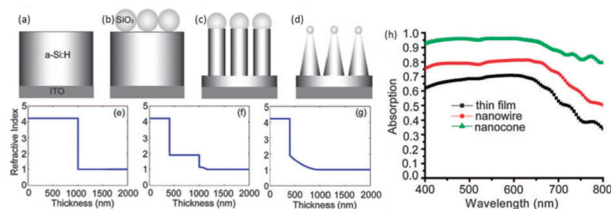
Fig. 5 Amorphous silicon nanocone array produced with a RIE method for anti-reflection. (a)–(d) The formation of nanocone array using SiO₂ nanoparticles as etching mask, (e)–(g) calculated dependence of the refractive index on the depth of the α-Si thin film, nanowire array, and nanocone array, respectively, and (h) a comparison of the optical absorption for α-Si thin film, nanowire array, and nanocone array.[74] Reprinted with permission from ref. 74. Copyright 2008 American Chemical Society.

amorphous silicon (α-Si) film, α-Si nanowire array, and α-Si nanocone array produced using the RIE method.[74] It was found that, among these films, only the α-Si nanocone array presented a graded refractive index along the axial direction of the nanocones (Fig. 5). As expected, the nanocone array achieved the most effective antireflection, giving rise to 93% optical absorption, which was significantly higher than the 75% and 64% for the nanowire array and planar thin film, respectively.

While the etching methods mentioned above target silicon-based solar cells by fabricating silicon nanostructures directly on the silicon substrate through a chemical etching approach, the growth of a layer of oxide nanowire/nanorod array is another flexible method which is compatible with both silicon and glass substrates for achieving antireflection; the latter is particularly being used in dye-sensitized solar cells, polymer solar cells, and quantum dot solar cells. ZnO nanorod arrays are one of the most widely studied one-dimensional nano-structures for application in solar cells for antireflection. Based on a well-known solution method developed by Vayssieres *et al.*[78,79] for the fabrication of the ZnO nanorod array, which employed a seed-coated substrate and an aqueous solution containing zinc nitrate and hexamethylenetetramine (HMT), Lee *et al.* found that the use of 1,3-diaminopropane (DAP) as an additive in the growth solution while adopting a long time growth (18 h) at relatively low temperature (60 °C) led to the formation of highly tapered ZnO nanowires.[80] The tapered ZnO nanowire array presented a good antireflection capability over the entire visible and near-infrared spectrum. The reflectance achieved by the highly tapered ZnO nanowire array (~1.5 μm in height) was 6.6%, which was much lower than 30.3% for a ZnO film prepared by the sol–gel method and, moreover, even lower than the 7.8% obtained for traditional single layer antireflection coating using silicon nitrate. This implies that the ZnO nanowire array is a promising candidate for antireflection coating, especially in the case of a glass substrate. Further studies revealed that the antireflection capability was closely related to the geometric parameters of the nanowires in terms of their diameter, length, sharpness, and distribution density. In work conducted by Chao *et al.*, an ~4 μm long ZnO nanorod array had an average reflectance of 9.53% in the spectral range from 350 nm to 850 nm.[81] So far, the minimum value of reflectance, which is below 0.5% as announced by Xi *et al.*,

was achieved by adopting a five-layer stacked film comprised of three layers of TiO₂ nanorod arrays at the bottom and two layers of SiO₂ nanorod arrays at the top; the thicknesses and porosities of these layers were designed to allow the film to possess the refractive indices following the modified-quintic-index profile.[82]

2.3.2 Surface plasmon resonance. Surface plasmon resonance (SPR) generated by metal nanoparticles is another effective approach that can be used to enhance the optical absorption of solar cell films, especially while considering that the aforementioned antireflection method is unsuitable for application to thin film solar cells in view of the geometric dimensions of the antireflection coating being on the sub-wavelength scale. Plasmon is a phenomenon that specifically exists in metal materials, depicting the collective longitudinal oscillation of electrons when the system is disturbed from equilibrium. Different from that in a bulk metal, when the dimensions of a metal are limited as in the case of metal nanoparticles, the oscillation of electrons leads to a deviation of the electron cloud from the geometric center of the metal and an oscillation of the electron cloud in the metal in the direction perpendicular to that of light wave propagation, forming the so-called surface plasmon resonance. According to the Fröhlich condition, the SPR reaches a maximum when the optical frequency, ω, satisfies the condition:

$$2\varepsilon_d = -\varepsilon_m(\omega) \tag{1}$$

where ε_d and ε_m are the dielectric constants of the surrounding medium and metal, respectively. Given that:

$$\varepsilon_m(\omega) = 1 - \left(\frac{\omega_p^2}{\omega^2}\right) \tag{2}$$

where ω_p is the oscillation frequency of the bulk plasmon, which is determined by the concentration of electrons, n, and the electron mass, m, according to:

$$\omega_p = \sqrt{\frac{ne^2}{\varepsilon_0 m}} \tag{3}$$

Therefore, the frequency for surface plasmon resonance, ω_{sp}, can be described as:

$$\omega_{sp} = \frac{\omega_p}{\sqrt{2\varepsilon_d + 1}} \tag{4}$$

It is evident that, for certain metals, the bulk frequency is a constant, however the SPR frequency (ω_{sp}), is a function of the dielectric constant of the surrounding medium (ε_d). A more comprehensive description of the SPR can be found elsewhere. Here, only two important formulas are listed regarding the scattering coefficient, C_{sca}, and absorption coefficient, C_{abs}, for a metal nanoparticle:

$$C_{sca} = \frac{8\pi}{3} k^4 r^6 \left| \frac{\varepsilon_m - \varepsilon_d}{\varepsilon_m + 2\varepsilon_d} \right| \propto \frac{r^6}{\lambda^4} \tag{5}$$

$$C_{abs} = 4\pi k r^3 \text{Im} \left| \frac{\varepsilon_m - \varepsilon_d}{\varepsilon_m + 2\varepsilon_d} \right| \propto \frac{r^3}{\lambda} \tag{6}$$

From eqn (5) and (6), it can be qualitatively known that the scattering and absorption caused by metal nanoparticles due to

3134 | *Chem. Soc. Rev.*, 2013, **42**, 3127–3171

This journal is © The Royal Society of Chemistry 2013
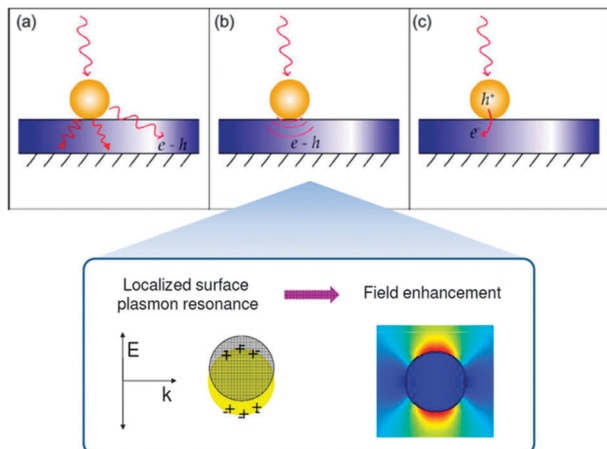
Fig. 6 Mechanisms of surface plasmon resonance enhancing optical absorption of solar cells. (a) Far field scattering leading to a prolonged optical path, (b) near field scattering causing local field enhancement, and (c) direct injection of photoexcited carriers into the semiconductor.[83] Reprinted with permission from ref. 83. Copyright 2009, The Optical Society (OSA).
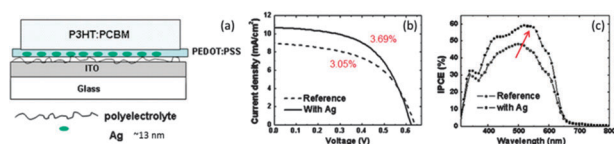

Fig. 7 Impact of (a) shape and (b) material selection of metal nanoparticles, and (c) the thickness of the underlayer on the SPR-induced optical absorption enhancement.[85] Reprinted with permission from ref. 85. Copyright 2008, American Institute of Physics.

SPR are related to the wavelength of the incident light and are proportional to the size of the nanoparticles.

SPR enhancement of the optical absorption of a solar cell film has been suggested to arise from three mechanisms (Fig. 6). The first mechanism is ascribed to far field scattering generated by the SPR, which can prolong the propagation distance of light within the solar cell film. The second mechanism is based on near field scattering that causes a local field enhancement, which may largely increase the absorption cross-section of the semiconductor as the active layer of the solar cell. The third mechanism involves the photoexcited carriers in the metal nanoparticles directly injecting into the semiconductor, making contributions to improve the photocurrent of the solar cell.[84]

Ag and Au are the most common metals that have been used in solar cells for SPR-induced optical absorption enhancement, as they do not have many interband transitions which may effectively limit their light absorption. Catchpole et al. systematically studied the SPR-induced optical absorption enhancement with Ag and Au nanoparticles deposited on a Si_3N_4 underlayer on silicon.[85] It was illustrated that the optical absorption enhancement originated from light scattering generated by the SPR of the metal nanoparticles. The fraction of incident light scattered into the substrate (i.e., silicon) was related to the shape of the nanoparticles to a large extent. A comparison of nanoparticles with cylindrical, hemispherical, and spherical shapes revealed that the cylindrical nanoparticles and hemispherical nanoparticles had a much better capability of scattering light into the substrate (Fig. 7a). The spherical nanoparticles with smaller size gave stronger scattering than the larger ones. As for the Ag and Au, it was found that the Ag hemispherical nanoparticles might lead to more scattering and therefore better enhance the optical absorption than the Au hemispherical nanoparticles (Fig. 7b). The thickness of the Si_3N_4 underlayer was also found to significantly affect the scattering. (Note: the underlayer is also called the spacer layer
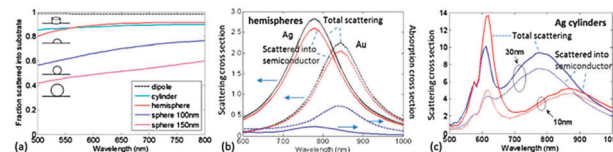
in the literature, and is adopted to provide passivation for the silicon film.) A decrease of the underlayer thickness, from 30 nm to 10 nm for example, could slightly increase the fraction of light scattered into the silicon at the wavelength of $\sim$600 nm corresponding to the quadrupole-mode excitation of SPR in Ag nanoparticles; however, decreasing the underlayer thickness largely reduced the fraction of light scattered into the silicon in the long wavelength region due to the decrease in the scattering cross-section for the dipole-mode excitation of SPR in the Ag nanoparticles (Fig. 7c). Conversely, in an experimental observation by Varlamov et al., compared with a 15 nm thick spacer layer, a 4 nm thick silicon nitride (SiN_x) spacer layer demonstrated a larger scattering cross-section and higher enhancement in the solar cell photocurrent.[86] In addition, the enhancement effect is also influenced by the distribution density of the nanoparticles. Derkacs et al. predicted that, for an amorphous silicon solar cell with tin-doped indium oxide (ITO) top electrode coated with 100 nm sized Au nanoparticles, the maximum light scattering enhancement was achieved when the particle density was $\sim$2.5 $\times$ 10^9 cm^{-2}.[87] It was explained that the existence of such an optimal particle density was due to the fact that the metal nanoparticles might unavoidably cause absorption and back scattering to the incident light, which could counterbalance the SPR enhancement to some degree.[88]

Another important application of the SPR enhancement effect is in polymer solar cells, where metal nanoparticles are typically mixed into the anode buffer layer made of poly(3,4-ethylene dioxythiophene):poly(styrene sulfonate) (PEDOT:PSS) to play a role in generating light scattering and a locally enhanced optical field to improve the optical absorption. In the literature, the use of 15 nm Au nanoparticles was reported to lead to an efficiency increase from 1.99% to 2.36% for a polymer solar cell with the configuration of ITO/PEDOT:PSS(Au)/MEH-PPV:PCBM/Al (note: MEH-PPV: poly(2-methoxy-5-(2′-ethyl-hexyloxy)-1,4-phenylene-vinylene), PCBM: [6,6]-phenyl-C61 butyric acid methyl ester).[89] In another study, $\sim$13 nm Ag nanoparticles were used for a polymer solar cell with the configuration of ITO/PEDOT:PSS(Ag)/P3HT:PCBM/Ca-Al and resulted in an efficiency improvement from 3.05% to 3.69%.[90] An apparent enhancement was observed in the spectrum of incident photon to current conversion efficiency (IPCE) for the solar cell with Ag nanoparticles embedded in the active layer, implying that the increase in the conversion efficiency originated from the Ag nanoparticles which yielded the SPR effect (Fig. 8).
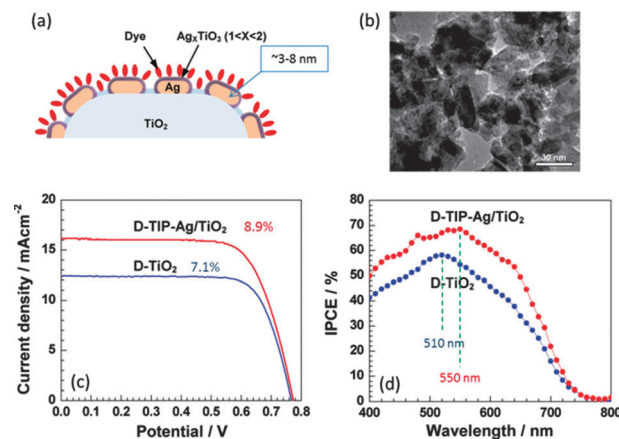
The SPR enhancement effect with metal nanoparticles has also been studied for DSCs. In work done by Jeong et al., a TiO_2

This journal is © The Royal Society of Chemistry 2013

Chem. Soc. Rev., 2013, **42**, 3127–3171 | **3135**

Fig. 8 Application of the SPR effect in polymer solar cells. (a) Structure of a polymer solar cell containing Ag nanoparticles in anode buffer layer, (b) *I*–*V* curves, and (c) IPCE spectra of polymer solar cells with and without Ag nanoparticles introduced to generate SPR enhancement.[90] Reprinted with permission from ref. 90. Copyright 2008, American Institute of Physics.

Fig. 9 Application of the SPR effect in dye-sensitized solar cells. (a) Schematic drawing showing the structure of the photoelectrode film consisting of Ag nanoparticle-coated TiO₂ sensitized by dye, (b) TEM image of Ag nanoparticles attached on TiO₂ particles, (c) *I*–*V* curves, and (d) IPCE spectra of dye-sensitized pure TiO₂ film (D-TiO₂) and dye-sensitized TiO₂ film with the attachment of titanium isopropoxide treated Ag nanoparticles (D-TIP-Ag/TiO₂).[91] Reprinted with permission from ref. 91. Copyright 2011 American Chemical Society.

nanocrystalline film, which is used in conventional DSC, was treated with a AgNO₃–EtOH solution to enable the adsorption of ∼3–8 nm sized Ag nanoparticles.[91] The film was then modified with titanium(IV) isopropoxide (TIP) to coat a thin layer of TiO₂ on the Ag nanoparticles to prevent corrosion when the Ag nanoparticles were exposed to the electrolyte and, meanwhile, allow the dye to be able to adsorb on the Ag nanoparticles (Fig. 9). Compared with 7.1% efficiency obtained for the cell without Ag nanoparticles, an ∼25% improvement in the efficiency was achieved for the cell including Ag nanoparticles (∼8.9% efficiency), and was attributed to the SPR effect due to the existence of Ag nanoparticles. The SPR effect enhanced the optical absorption by either generating light scattering to prolong the optical pathway or causing local field enhancement to increase the optical absorption cross-section of the dye. In other work performed by Photiphitak *et al.*, the optimal size for Ag nanoparticles to maximally enhance the optical absorption of the dye-sensitized TiO₂ nanocrystalline film was determined to be ∼19 nm through comparing the absorption enhancement induced by the Ag nanoparticles with different sizes.[92] It was found that the Ag nanoparticles with size larger than 19 nm might yield more intense SPR enhancement, but they could lower the internal surface area of the photoelectrode film leading to low dye adsorption and thus a decrease in the overall conversion efficiency. Ding *et al.* attached ∼5–6 nm Ag nanoparticles on 400 nm SiO₂ particles to form a core–shell nanostructure, and then embedded the core–shell nanostructure into a TiO₂ nanocrystalline film to intentionally generate light scattering using the SiO₂ particles and simultaneously introduce the SPR effect into DSCs with the Ag nanoparticles.[93] The study exhibited that the core–shell nanostructure mixed into TiO₂ nanoparticles in a volume percentage of 22% provided the maximum enhancement in the optical absorption of the photoelectrode film. The highest efficiency achieved was 4%, higher than ∼3% for pure TiO₂ nanocrystalline film and 2.7% obtained for the photoelectrode film containing 22 vol% SiO₂ particles alone, evidencing that the conversion efficiency enhancement resulted from the SPR effect induced by Ag nanoparticles.

An important merit of the SPR effect for solar cell application is that the SPR frequency, ω_{sp}, is tunable, which can be used to generate absorption enhancement at desired wavelengths. There are many methods that can be adopted to adjust the wavelength region for absorption enhancement induced by the SPR effect. First, adjustment can be achieved by choosing a suitable metal material to form the nanoparticles. This is because the SPR frequency varies for different metal materials. For example, in air, the wavelength corresponding to the SPR frequency of Ag nanoparticles is 350 nm, and it is 480 nm for Au nanoparticles. Alloys, which contain more than one metal, can be adopted to tune the SPR frequency, allowing the frequency to fall between those of individual metals.[94] Secondly, the SPR frequency can be tuned by varying the size of the metal nanoparticles. For very small nanoparticles, for example with a diameter smaller than ∼20 nm, the SPR frequency can be estimated according to eqn (4). However, increasing the particle size, for example to be larger than 100 nm in diameter for Ag nanoparticles in air, has been reported to lead to a red-shift of the SPR frequency and an enhancement in the scattering cross-section.[95] Particles that are too large will result in multipole oscillations. For 200 nm diameter Ag nanoparticles in air, besides a dipole-mode oscillation at a wavelength of ∼400 nm, a quadrupole-mode oscillation typically around ∼600 nm could be clearly observed (Fig. 10a).[95] Multipole oscillations might enhance the optical absorption of solar cells in a broader spectral range than the single dipole-mode oscillation, however the emergence of multipole oscillations diminished the scattering cross-section of each oscillation (Fig. 10a).[95]
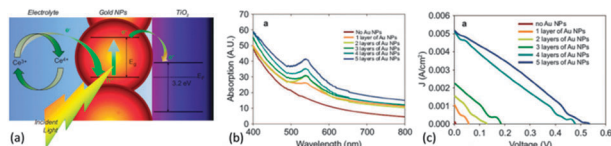
Designing the medium that surrounds the nanoparticles is another important way of tuning both the frequency and scattering cross-section of the SPR. It was demonstrated that the SPR frequency for 100 nm diameter Ag nanoparticles could change from a wavelength of ∼350 nm to ∼550 nm and ∼900 nm when the surrounding medium was air, Si₃N₄, and Si, respectively, almost covering the entire visible–near infrared spectral range (Fig. 10b).[96] Further studies revealed that changing the surrounding media for Ag nanoparticles from air to, for example, Si might lead to great enhancement of the dipole-mode oscillation in the case of small particles (with diameter less than 20 nm); however, for
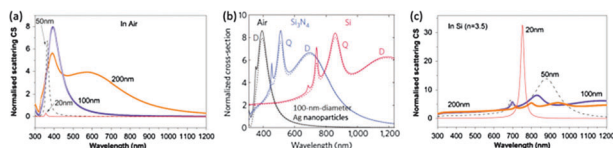
Fig. 10 Wavelength- and intensity-tunable SPR absorption enhancement. (a) SPR spectra of metal nanoparticles with different sizes in air, (b) SPR spectra of 100 nm diameter Ag nanoparticles in air, Si_3N_4, and Si, respectively, and (c) SPR spectra of metal nanoparticles with different sizes in Si.[95,96] Fig. 10a and c are reprinted from *Solar Energy Materials and Solar Cells*, Volume 94, Issue 9, S. Pillai et al., Plasmonics for photovoltaic applications, Pages 1481–1486, Copyright 2010, with permission from Elsevier. Fig. 10b is reprinted with permission from ref. 96. Copyright 2010, Nature Publishing Group.

large particles, the quadrupole-mode oscillation showed more significant enhancement compared to that of the dipole-mode oscillation (Fig. 10c).[95] While the SPR effect has been used to generally enhance the optical absorption of solar cells, its feature of tunable absorption enhancement is thought to be particularly significant to creating "transparent solar cells", which primarily rely on the absorption of near-infrared light.
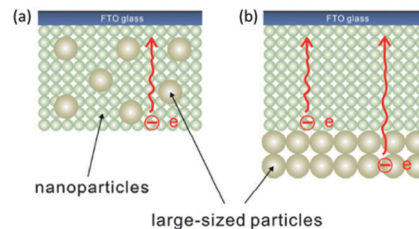
Besides the enhancement arising from the SPR-induced light scattering and local field enhancement, direct electron injection owing to SPR has also been identified as a way to improve solar cell performance. An impressive work in this regard was performed by Su et al. by developing a plasmonic solar cell, the photoelectrode of which was made of TiO_2 nanoparticles with ~ 6 nm diameter Au nanoparticles adsorbed on the surface to serve as a sensitizer for light harvesting (Fig. 11a).[97] Platinum coated ITO glass was employed as the counter electrode, and a water-based electrolyte (35% ethanol and 65% water) containing 0.1 M $Ce(NO_3)_3$ and 0.05 M $Ce(NO_3)_4$ was filled into the gap between the photoanode and the counter electrode. The optical absorption of the Au-adsorbed TiO_2 film was found to be proportional to the amount of adsorbed Au nanoparticles (Fig. 11b). As a result, the overall conversion efficiency of the solar cell also increased with increasing adsorption of the Au nanoparticles, from 0.016% for 1 layer of Au nanoparticles to 0.75% for 5 layers of Au nanoparticles (Fig. 11c). It was revealed that the photoexcited electrons near the surface of Au nanoparticles might have enough energy to overcome the Schottky barrier at the Au/TiO_2 interface, and inject into the conduction band of the TiO_2, due to the presence of SPR and overlapping of the SPR absorption band with the interband transition in gold nanoparticles.[98]

However, the details of such an interband electron transition and SPR-assisted electron injection mechanism still require further investigation.

2.3.3 Light scattering. Besides utilizing metal nanoparticles to achieve light scattering based on the SPR effect, adopting dielectric spheres that are comparable in size to the wavelengths of visible light is another method which has been extensively used for the generation of light scattering especially in DSCs. Light scattering is essential to DSCs, arising from the structure of the DSC photoelectrode film that is composed of porous oxide nanocrystalline film with dye molecules adsorbed on the surface that act as a sensitizer for light harvesting. It has been proven that a monolayer adsorption of dye molecules is optimal for DSC functionality, since the multilayered adsorption of dye molecules is ineffective for electron injection although it may increase the optical absorption of the photoelectrode film. However, in comparison with semiconductor solar cells constructed with bulk thin films, a monolayer dye adsorbed porous nanocrystalline film structure results in a relatively low optical absorption cross-section – a DSC photoelectrode film should therefore be as thick as possible so as to adsorb enough dye molecules and thus achieve sufficient absorption of the incident light. However, the practically feasible thickness for a DSC photoelectrode film is limited by the diffusion length of the electrons in the nanocrystalline oxide film; the photoelectrode film consisting of oxide nanoparticles is intentionally employed in DSCs to provide large internal surface area for dye adsorption, but it simultaneously gives rise to a large oxide/electrolyte interface, which increases the probability for charge recombination and therefore acts to shorten the diffusion length of the electrons. The optimal thickness for the DSC photoelectrode film is typically around 15 μm. However, the optical absorption of a dye-sensitized nanocrystalline oxide film with this thickness has been shown to be incomplete, i.e., there is a loss of incident light due to partial transmission from the low absorption section of the dye-sensitized nanocrystalline film. In conventional DSCs, this problem is partially circumvented by including large sized particles (~ 400 nm in diameter) in the nanocrystalline film to scatter the light and thus extend the light pathway within the photoelectrode film. One structure that is adopted in the conventional DSCs is the incorporation of large particles into the nanocrystalline film to serve as light scatterers, forming a *mixed structure* (Fig. 12a). However, embedding the large particles

Fig. 11 Plasmonic solar cell. (a) Schematic drawing showing SPR-induced electron injection from metal nanoparticles to semiconductor, (b) optical absorption spectra of Au-adsorbed TiO_2 nanoparticle films, and (c) I–V curves of plasmonic solar cells with photoelectrode films consisting of TiO_2 nanoparticles with the adsorption of different amounts of Au nanoparticles.[97] Reprinted with permission from ref. 97. Copyright 2012, Nature Publishing Group.


Fig. 12 The structures of the photoelectrode film in conventional DSCs including large particles for light scattering. (a) Mixed structure, and (b) double-layer structure.

in the nanocrystalline film would unavoidably decrease the internal surface area of the photoelectrode film, and in turn reduce the amount of dye adsorption and thereby counter-balance the optical absorption enhancement arising from light scattering. Another structure that is more commonly used for light scattering in conventional DSCs is the addition of a layer of large particles on the nanocrystalline film to form a *double-layer structure* (Fig. 12b). The light introduced from the substrate side would be reflected back to the nanocrystalline film by the large particle light scattering layer. In this way, the travelling distance of the incident light is doubled so that the optical absorption of the photoelectrode can be effectively improved. However, the double-layer structure is not thought to be perfect since (1) the electrons generated in the scattering layer under photoexcitation only make a slight contribution to the overall photocurrent because the long distance to the collecting electrode makes diffusion for these electrons difficult, (2) the existence of a large particle layer may somewhat hinder the electrolyte diffusion and thus diminish the solar cell performance, and (3) the double-layer structure is not preferred for manufacturing and lowering the cost of solar cells due to the need for additional processing steps.

Nanocrystallite aggregates of oxides are a new type of nanostructure recently developed. When the nanocrystallite aggregates are used in DSCs for photoelectrode films, it has been demonstrated that they can generate effective light scattering to prolong the light pathway in the photoelectrode film and, meanwhile, provide sufficient internal surface area comparable to that of conventional nanocrystalline films used for dye adsorption.[99–101] A study of DSCs with ZnO nano-crystallite aggregates revealed that the solar cell efficiency of ZnO nanoparticles could be improved from 2.4% to as high as 5.4% when employing the nanocrystallite aggregate structure.[99] A gradual evolution of the photoelectrode film structure from dispersed nanoparticles to partial and perfect aggregates led to a corresponding increase in the overall conversion efficiency of the cells. This increase was attributed to light scattering generated by the aggregates, leading to an extension of the traveling distance of incident light and therefore an increase in the probability of photons interacting with the dye molecules adsorbed on the ZnO nanocrystallites (Fig. 13). A further study found that the conversion efficiency had a dependence on the size and size distribution of the aggregates.[100] It was demonstrated that the photoelectrode film consisting of mono-dispersed nanocrystallite aggregates with a size closer to the wavelength of incident light exhibited higher conversion efficiency. Such results are consistent with that predicted by Mie Theory, which states that the light scattering can reach its maximum when the dimensions of the object are comparable to the light wavelength. It was also revealed that the photo-electrode film made of aggregates with broad size distribution achieved a higher efficiency than that composed of aggregates with narrow size distribution. This result was explained by considering that the photoelectrode film structure of the former was more disordered than that of the latter, resulting in more intense light scattering. The finding that nanocrystallite
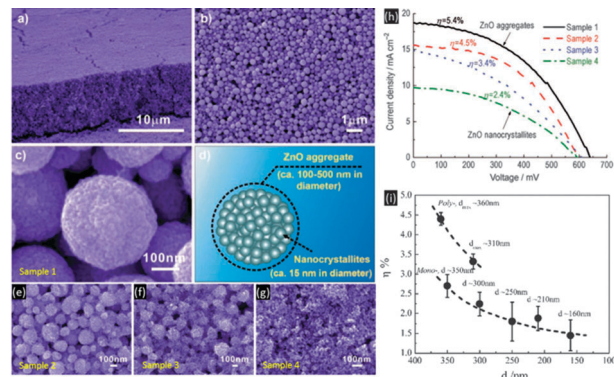
Fig. 13 DSCs with ZnO nanocrystallite aggregates. (a)–(d) Structure of the photoelectrode film (Sample 1) consisting of nanocrystallite aggregates, (e)–(g) SEM images of Samples 2 through 4: the building blocks that form the film change from aggregates to dispersed nanocrystallites, (h) I–V curves for Samples 1 through 4, and (i) efficiency dependence on size and size distribution of the aggregates.[99,100] Reprinted with permissions from ref. 99 and 100. Copyright 2008, Wiley-VCH.
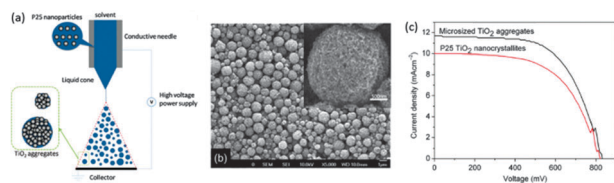
Fig. 14 Electrospray for the fabrication of nanocrystallite aggregates. (a) Sche-matic drawing showing the electrospray system, (b) SEM image of TiO_2 aggre-gates made of P25 nanoparticles, (c) I–V curves of solar cells with TiO_2 nanocrystallite aggregates and dispersed nanoparticles.[102] Reprinted with per-mission from ref. 102. Copyright 2011, American Scientific Publishers.

aggregates are able to enhance the DSC performance is a good example highlighting that solar cells can greatly benefit from nanostructured materials that are purposely designed with unique optical or electrical properties.

Electrospray is a general method that can be used for the synthesis of oxide nanocrystallite aggregates.[102,103] As an example, a schematic drawing is shown in Fig. 14a depicting the system used for the formation of a spherical agglomeration of nano-crystallites with the electrospray method. Oxide nanocrystallites are dispersed in a solvent to which a suitable surfactant is added to prevent the nanocrystallites from precipitating. The solution containing the nanocrystallites is slowly pushed out of a nozzle, where it forms a liquid droplet. By applying a high enough electric field between the nozzle and the collector (*i.e.*, grounded electrode), the liquid droplet becomes charged and splits into smaller droplets due to Coulombic repulsion. The small droplets migrate to the collector, during which the solvent in the droplets evaporates and spherical agglomerations of oxide nanocrystallites are formed. While a high voltage, V, is applied between the nozzle and the collector, the intensity of the electrostatic field at the liquid droplet, E, can be given by[104]

$$E = \frac{2V}{r \ln(4d/r)} \qquad (7)$$

3138 | *Chem. Soc. Rev.*, 2013, **42**, 3127–3171

This journal is © The Royal Society of Chemistry 2013

where r is the radius of the liquid droplet and d is the distance from the nozzle to the collector. Xi *et al.* studied the fabrication of TiO$_2$ nanocrystallite aggregates using the electrospray method starting with commercial P25 TiO$_2$ nanoparticles (Degussa, Germany).[102] The precursor solution for the spray was prepared by dispersing the P25 nanoparticles into an ethanol–water (1 : 1, v/v) mixture, to which PVP (polyvinylpyrrolidone, MW $\approx 1.3 \times 10^6$) was added to increase the viscosity of the solution and adjust the porosity of the aggregates. It was found that the size of the aggregates was mainly dependent on the nanoparticle concentration of the precursor solution and the voltage applied to the nozzle and collector. The resultant TiO$_2$ nanocrystallite aggregates achieved 5.9% efficiency when used for DSC, significantly higher than the 4.8% efficiency obtained for the dispersed P25 nanoparticles (Fig. 14c). However, the dye loading amount of the aggregate film, 38.5 nmol cm^{-2}, was found to be lower than that of the P25 nanoparticle film, 44.4 nmol cm^{-2}, due to the existence of gaps amongst the aggregates leading to a loss of some internal surface area. This strongly suggested that the improved efficiency resulted from light scattering generated by the aggregates, which greatly extended the light pathway and thus enhanced the optical absorption of the photoelectrode despite the decreased dye adsorption. A higher efficiency can be expected by filling the gaps in the aggregate film with nanoparticles to achieve sufficient dye loading.

Besides the advantage of being able to synthesize nanocrystallite aggregates, another significant merit of the electrospray method is its ability to use pre-prepared nanoparticles for the formation of aggregates, and thereby is able to retain the facets of the nanoparticles that form the aggregates. This point is critically important to a material specifically for application in DSCs, for the reason that anatase TiO$_2$ with exposed (101) facets is known to be able to achieve the highest dye loading and the most efficient electron injection compared with rutile TiO$_2$ or other facets of anatase TiO$_2$,[105] so utilization of the electrospray method allows the use of TiO$_2$ nanoparticles that are separately synthesized by a hydrothermal method, which yields TiO$_2$ nanoparticles with high crystallinity and the most ideal facets for dye loading. Therefore, superior to other methods, the electrospray process may ensure that the parameters for nanocrystallites comprising the aggregates are fully optimized.

Mesoporous TiO$_2$ beads, similar to the nanocrystallite aggregates, are a type of nanostructure that may also simultaneously provide large specific surface area and light scattering. Chen *et al.* reported a two-step method for the synthesis of mesoporous TiO$_2$ beads by first preparing amorphous TiO$_2$ spheres with a diameter of 1150 ± 50 nm through the hydrolysis of titanium isopropoxide in an ethanol solution containing hexadecylamine, KCl, and water, then followed by a solvothermal treatment of the amorphous TiO$_2$ spheres in an ethanol–water solution containing ammonia to convert the TiO$_2$ spheres to crystalline mesoporous beads.[106,107] Ammonia was used to adjust the porosity of the beads, and it was also found to affect the aspect ratio of the elongated nanocrystals that form the beads. DSC performance analysis of the mesoporous TiO$_2$ beads, which consisted of nanocrystals $\sim$18 nm in
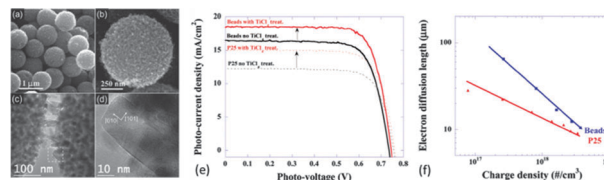
Fig. 15 Mesoporous TiO$_2$ beads for DSCs. (a)–(d) Morphology and structure of mesoporous TiO$_2$ beads, (e) a comparison of DSC performance of mesoporous TiO$_2$ beads and P25 nanoparticles, (f) longer diffusion length of electrons in mesoporous bead film than in nanoparticle film.[106,108] Fig. 15a is reprinted with permission from ref. 106. Fig. 15b and c are reprinted from ref. 108. Copyright 2010 American Chemical Society.

diameter (Fig. 15a–d), achieved an efficiency of 7.20% for a $\sim$12 μm thick photoelectrode film, considerably higher than the 5.66% obtained for the dispersed P25 nanoparticles.[107] It was believed that the mesoporous bead film might give rise to more intense light scattering than the P25 nanoparticle film (due to the agglomeration of nanoparticles), resulting in more optical absorption as well as higher conversion efficiency of the cell. In addition to the contribution by light scattering, it was also found that the photoelectrode film comprised of mesoporous beads achieved more dye loading than the film made of nanoparticles, which was ascribed to the mesoporous beads possessing a smaller nanocrystal size than the P25 nanoparticles and therefore having a larger internal surface area. In other work performed by Sauvage *et al.*, optimized mesoporous TiO$_2$ beads demonstrated an efficiency as high as 10.6%, in comparison with 8.5% obtained for P25 nanoparticles (Fig. 15e).[108] Aside from light scattering, the mesoporous beads were also suggested to be an advanced structure that could conduct electrons better than the nanoparticle film in view of the highly close packing structure of the nanocrystallites in the beads, presenting a longer electron diffusion length in the photoelectrode film of the mesoporous beads (Fig. 15f).

Besides the nanocrystallite aggregates and the mesoporous beads, multilayered hollow spheres have also recently been reported for DSC applications and show a promising structure that may generate light scattering between and in the hollow spheres. Qian *et al.* studied a DSC with TiO$_2$-modified multilayered SnO$_2$ hollow spheres, which had diameters of 1–2 μm and the shell-in-shell structure constructed with $\sim$13 nm SnO$_2$ nanocrystalltes.[109] It was found that, while the commercial SnO$_2$ nanoparticles only demonstrated 1.0% DSC conversion efficiency, the TiO$_2$-modified multilayered SnO$_2$ hollow spheres achieved an efficiency as high as 5.65%, even higher than the 5.14% efficiency value obtained for the P25 TiO$_2$ nanoparticles, although the latter possessed more dye loading (Fig. 16). It was suggested that the cell greatly benefited from the structure of the multilayered hollow spheres which scattered the light in-between the spheres and therefore enhanced the optical absorption of the photoelectrode (Fig. 16 inset). Wu *et al.* reported the synthesis of TiO$_2$ shell-in-shell hollow spheres, also presenting good light scattering behavior when used in DSCs.[110] A recent review paper summarized the existing methods for the synthesis of multilayered hollow spheres,
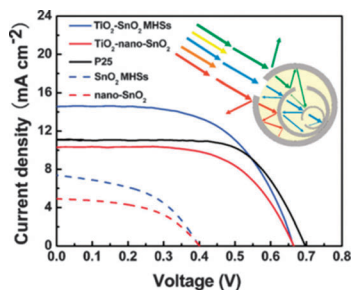
Fig. 16 Multilayered hollow spheres for DSC applications. The inset is a schematic drawing showing the light scattering in-between the hollow spheres. (TiO$_2$-SnO$_2$ MHSs: TiO$_2$-coated multilayered SnO$_2$ hollow microspheres, TiO$_2$-nano-SnO$_2$: TiO$_2$-coated SnO$_2$ nanoparticles, SnO$_2$ MHSs: multilayered SnO$_2$ hollow microspheres, nano-SnO$_2$: commercially available SnO$_2$ nanoparticles.)[109] Reprinted with permission from ref. 109. Copyright 2009, Wiley-VCH.
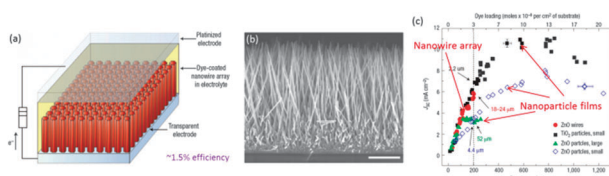
including hard-template methods, soft-template methods, template-free methods, etc.[111]

2.4 Nanostructures used in solar cells for improved electron transport and collection

2.4.1 One-dimensional nanostructures. One-dimensional nanostructures such as ZnO nanowires/nanorods and nanotubes, and TiO$_2$ nanotubes and nanorods have been extensively studied for solar cell applications, in view of their features of (1) a single crystalline phase, which means there are less defects in the material and therefore less energy loss arising from electron trapping during electron transport, (2) inorganic composition in which the electron mobility is much higher and therefore the electron transport is highly efficient in comparison with polymers, and (3) the one-dimensional structure, which provides a direct pathway for electron transport. These features of one-dimensional nanostructures are particularly important to polymer solar cells and dye-sensitized solar cells, where the single crystalline, inorganic, one-dimensional nanostructures can be utilized to reduce the recombination of photogenerated electrons with holes in the polymer (in the case of polymer solar cells) or oxidized redox couples in the electrolyte (in the case of dye-sensitized solar cells), considering that the distance for the electrons to transport from the sites where they generate to the collecting electrode in these solar cells is relatively long.

Law et al. developed a single crystalline ZnO nanowire array that was used for the first time for DSCs in order to provide direct pathways for electron transport (Fig. 17a and b).[112] The employment of a ZnO nanowire array for DSCs is based on the consideration of overcoming severe charge recombination in conventional DSCs with a photoelectrode film comprised of TiO$_2$ nanoparticles. The photogenerated electrons may have a high probability of recombining with the oxidized redox couples in the electrolyte when transporting through the TiO$_2$ nanoparticle film in a trapping–detrapping manner because of the large nanoparticle–electrolyte interface and the lack of an internal electric field in the nanoparticle film forcing the movement of electrons.[65] ZnO nanowire arrays may work towards reducing the charge recombination owing to the single crystalline nature of the nanowires and the high electron mobility of ZnO. It was observed that the electron diffusivity for individual ZnO nanowires was 0.05–0.5 cm^2 s^{-1}, which is several hundred times larger than the highest reported electron diffusion coefficients for nanoparticle films (10^{-7} to 10^{-4} cm^2 s^{-1} for TiO$_2$ and 10^{-5} to 10^{-3} cm^2 s^{-1} for ZnO) in a DSC configuration under operating conditions. The second reason for a nanowire array being superior to a nanoparticle film is the existence of an internal electric field in the nanowires along their radial direction, which can corral the electrons and accelerate their diffusion so as to lower the recombination rate of the cell. It is worth noting that such an internal electric field cannot be established in TiO$_2$ nanoparticles as small as $\sim$20 nm in diameter that are used in conventional DSCs, in view of a low electron concentration in TiO$_2$ and the size of nanoparticle being smaller than the Debye–Hückel screening length (roughly one-third of the thickness of the space-charge layer in the semiconductor that forms a junction with the electrolyte). The advantage of ZnO nanowires for electron transport in DSCs was evidenced by an experimental observation showing that the ZnO nanowire array achieved considerably higher photocurrent than the ZnO nanoparticle film under the same roughness factor; for example, at a roughness of 200, the photocurrent achieved by the nanowire array was approximately 55–75% higher than that achieved by the nanoparticle film (Fig. 17c). Furthermore, it was determined that the ZnO nanowire array was able to harvest photocurrent comparable to the TiO$_2$ nanoparticle film when they had the same roughness factor, but note that in this case the thickness of the nanowire array was far larger than that of the nanoparticle film. For example, at a roughness of 200, the ZnO nanowire array with a thickness as large as 24 μm was shown to be as equally efficient as a 2.2 μm thick TiO$_2$ nanoparticle film. In conventional DSCs, the maximum allowable thickness for a photoelectrode film made of nanoparticles is approximately 15 μm; a photoelectrode film that is too thick will decrease the overall conversion efficiency as a result of increased charge recombination, leading to a saturation of the photocurrent and a rapid drop of the open-circuit voltage. In the case of ZnO nanowires, the larger thickness allowed for the photoelectrode film implied that electron transport in the ZnO nanowires was much more efficient than in a nanoparticle film.

Although one-dimensional nanostructures have proven to be advantageous in conducting electrons, practical use of them for DSCs has not resulted in an efficiency higher than that of TiO$_2$ nanoparticles, the record efficiencies of which are $\sim$11–12% to date.

Fig. 17 ZnO nanowire DSCs. (a) Structure of a nanowire DSC, (b) cross-sectional SEM image of ZnO nanowire array, and (c) a comparison of electron transport in the nanowire array and nanoparticle films.[112] Reprinted with permission from ref. 112. Copyright 2005, Nature Publishing Group.

3140 | Chem. Soc. Rev., 2013, **42**, 3127–3171

This journal is © The Royal Society of Chemistry 2013

For DSCs with single crystalline ZnO nanowires or nanotubes, the efficiencies are typically in the range of 1.0%–2.5%.[112–116] Modifying the ZnO nanowires with a thin layer of TiO$_2$ could improve the solar cell efficiency to some degree compared to uncoated ZnO nanowires, owing to an increase in the chemical stability of ZnO in the dye solution and the establishment of an internal electric field at the ZnO/TiO$_2$ interface due to the formation of a heterojunction.[117,118]

TiO$_2$ nanotubes are another typical one-dimensional nanostructure that has also been extensively studied for DSC applications. Anodization of Ti foil is a facile method for the growth of TiO$_2$ nanotubes up to ∼220 μm in length.[119] A DSC efficiency as high as 6.9% has been reported with an array composed of ∼20 μm long nanotubes under backside illumination (i.e., illuminated from the Pt-coated FTO side. FTO: fluorine-doped tin oxide).[119] A higher efficiency of ∼7.4%, which is the record efficiency to date, was achieved by carrying out a surface modification of the TiO$_2$ nanotube array with TiCl$_4$ and treating with oxygen plasma exposure.[120]

One of the reasons that the one-dimensional nanostructures achieve lower efficiencies than TiO$_2$ nanoparticles is because of the insufficient internal surface area provided by the nanowire or nanotube arrays when they are adopted to have a length comparable to the thickness of the nanoparticle films. However, the prospect of preparing thin enough one-dimensional nanostructures while being arranged in a high density to achieve a photoelectrode film with very large internal surface area is presenting tremendous technical difficulties at this time. Increasing the length of the nanowires or nanotubes may certainly increase the internal surface area of the photoelectrode film, but the maximum allowed length is limited by the diffusion length of the electrons. Nevertheless, even if the photoelectrode films are made of one-dimensional nanostructure arrays with thicknesses comparable to the electron diffusion length, their internal surface area can be estimated to be still much lower than that of a nanoparticle film ∼15 μm in thickness consisting of ∼20 nm diameter nanoparticles. Furthermore, the fact that the merits of the TiO$_2$ nanoparticles in terms of high crystallinity and suitable facets for dye adsorption and electron injection cannot be attained with the nanowires or nanotubes is also the reason for relatively low efficiency for the DSCs with nanowires or nanotubes.

Filling the gaps between the nanowires with nanoparticles is thought to be a way that can increase the internal surface area of a photoelectrode comprised of the nanowire or nanotube array. A study conducted by Yodyingyong et al. demonstrated that solar cells constructed with an 11 μm long ZnO nanowire array and an ∼10 μm thick film consisting of ∼14 nm diameter ZnO nanoparticles both presented low conversion efficiencies, 1.58% and 1.31%, respectively (Fig. 18a–e).[66,113] However, the efficiency greatly increased to 4.23% by employing a hybrid structure comprised of an 11 μm long ZnO nanowire array mixed with ∼14 nm ZnO nanoparticles. This increase in the conversion efficiency was explained to result partially from an increase in the internal surface area of the photoelectrode due to the inclusion of additional nanoparticles, which was reflected by
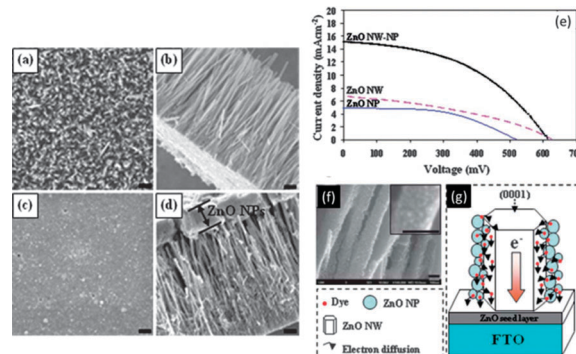
Fig. 18 ZnO nanowire–nanoparticle hybrid photoelectrode for DSCs. (a, b) SEM images of ZnO nanowire array, (c, d) SEM images of ZnO nanowire array mixed with ZnO nanoparticles, (e) I–V curves of DSCs with ZnO nanoparticles (ZnO NP), ZnO nanowire array (ZnO NW), and ZnO nanowire array mixed with ZnO nanoparticles (ZnO NW-NP), and (f, g) SEM images and schematic drawing showing the attachment of ZnO nanoparticles on ZnO nanowires and the electron transport through ZnO nanowires.[113] Reprinted with permission from ref. 113. Copyright 2010, American Institute of Physics.

a slight increase in the dye loading amount from 6.39×10^{16} to 7.48×10^{16} molecules cm^{-2} after introducing the nanoparticles. It was further hypothesized that the existence of single crystalline ZnO nanowires in the hybrid structure photoelectrode led to highly efficient electron transport and, as a result, the charge recombination in the nanowire–nanoparticle hybrid photoelectrode was much smaller than that in a nanoparticle photoelectrode (Fig. 18f and g). Compared to the photoelectrode film consisting of ZnO nanoparticles alone, the relatively open structure of the nanowire–nanoparticle hybrid photoelectrode film is believed to allow a quick infiltration of the dye solution to form a better monolayer of dye adsorption on the ZnO nanoparticles and nanowires and therefore contribute to improving the efficiency as well. A similar work was also completed by Pan et al. by combining a TiO$_2$ nanotube array with TiO$_2$ nanoparticles.[121] It was found that, compared with a DSC made of bare TiO$_2$ nanotubes, the overall conversion efficiency was enhanced by 152% through the addition of TiO$_2$ nanoparticles ∼10 nm in diameter. The degree of enhancement was dependent on the length of the TiO$_2$ nanotubes. However, it was observed that too long TiO$_2$ nanotubes led to a less significant enhancement, which was attributed to the low electron collection efficiency due to electron trapping during transport in the nanotubes.

One-dimensional nanostructures have also been studied for application in polymer solar cells, specifically inverted structure polymer solar cells. Conventional polymer solar cells are typically built on an ITO glass substrate with a sequential deposition of PEDOT:PSS as the hole transport layer (i.e., anode buffer layer, ABL), a blend of P3HT and PCBM as the active layer, an oxide thin film as the electron transport layer (i.e., cathode buffer layer, CBL), and a metal electrode as the collecting electrode (Fig. 19a). In conventional polymer solar cells, the excitons generated in the P3HT:PCBM active layer move to the interface between the P3HT and PCBM, where they dissociate into free electrons and holes due to the offset between the lowest

unoccupied molecular orbital (LUMO) levels of the P3HT and PCBM. The holes then move toward the PEDOT:PSS and ITO side, while the electrons transport to the oxide and metal electrode side. However, polymer solar cells with conventional structure suffer from a severe stability problem, arising from (1) the PEDOT in contact with ITO causing corrosion to the ITO film, and (2) the top electrode using a low work function metal in order to match the energy level requirement for electron injection. Al is a typical material that has been widely used in polymer solar cells for the top electrode. Both the corrosion of ITO film and the oxidization of the Al electrode while exposed in air may notably degrade the cell performance. Inverted structure polymer solar cells were devised with the aim to solve the aforementioned stability problem in conventional polymer solar cells by adopting an "inverted" structure. In the inverted structure polymer solar cells, the ITO glass substrate was coated with an oxide thin film instead of the PEDOT:PSS as the cathode buffer layer. On the oxide film, a blend of P3HT and PCBM, a layer of PEDOT:PSS, and a metal electrode were sequentially fabricated (Fig. 19b). The first merit of the inverted polymer solar cells is that the geometry can avoid the ITO–PEDOT:PSS contact and thereby the problem of corrosion of the ITO film that exists in conventional polymer solar cells is resolved. Secondly, in the inverted structure solar cells the material for the top electrode can be a high work function metal because here the holes transport to the metal electrode side while the electrons move toward the oxide and ITO side. With these effects resulting from the inverted structure, the chemical stability of polymer solar cells has been greatly improved. Another feature of the inverted structure polymer solar cells is that the performance of the cells heavily relies on the material, morphology, and structure of the cathode buffer layer.[122] This, in turn, gives a great opportunity for improving the solar cell performance by designing and optimizing the cathode buffer layer. ZnO, along with several other oxides, has been extensively studied to serve as the cathode buffer layer in the inverted structure polymer solar cells. The morphology of the ZnO film has been demonstrated to have a significant impact on the solar cell performance.[123] In regard to the structure influence, recent studies have suggested that one-dimensional nanostructures may be used in the inverted polymer solar cells as the cathode buffer layer to enhance the electron transport and collection.

TiO$_2$ nanorod arrays are one of the one-dimensional nanostructures that have been used in inverted polymer solar cells to enhance the performance.[66,124] In a study reported by Xi et al., the TiO$_2$ nanorod array was grown on an FTO glass substrate through a hydrothermal reaction at 150 °C by placing the FTO glass substrate into an autoclave that contained distilled water mixed with hydrochloric acid in a volume ratio of 1:1, to which 5% (by volume) titanium butoxide was added.[124] The dimensions of the TiO$_2$ nanorods were controlled by adjusting the growth time. It was found that an 85 min growth led to the formation of nanorods with diameters of 50 ± 15 nm and a length of $\sim$140 nm (referred to as TiO$_2$ NRs-1), while a 100 min growth gave rise to nanorods with diameters of 75 ± 15 nm and a length of $\sim$500 nm (referred to as TiO$_2$ NRs-2) (Fig. 20a–d).
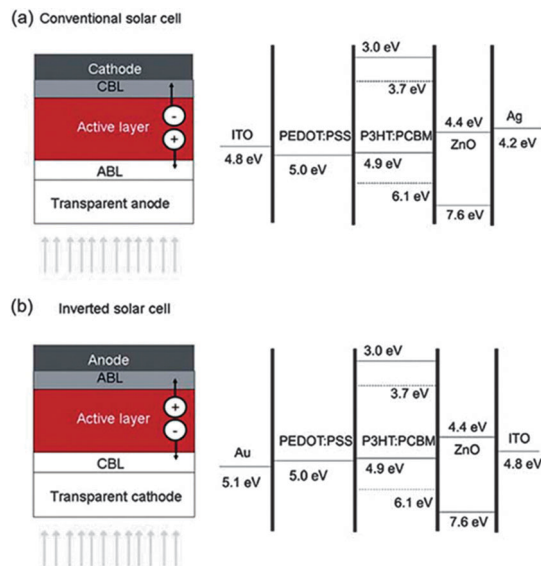

Fig. 19 Configurations and energy band structures of (a) conventional structure polymer solar cells and (b) inverted structure polymer solar cells. (ABL: anode buffer layer, CBL: cathode buffer layer).[66]

The substrates with the as-grown TiO$_2$ nanorods, which work as the cathode buffer layer (CBL), were employed to construct inverted structure polymer solar cells by a sequential deposition of PCBM, a blend of P3HT:PCBM, PEDOT:PSS, and a Ag film electrode. For comparison, a cell with a layer of TiO$_2$ dense film (referred to as TiO$_2$ DF) as the cathode buffer layer was also prepared while the other parameters remained the same. As expected, the cell with the cathode buffer layer of TiO$_2$ NRs-1, i.e., the relatively short nanorods, produced an efficiency of 3.21% that was higher than that of the 2.79% obtained for the cell with the TiO$_2$ DF cathode buffer layer. However, TiO$_2$ nanorods that are too long and too thick used for the cathode buffer layer were found to lead to a significant decrease in the conversion efficiency of the cell. This was observed for the TiO$_2$ NRs-2, which served as the cathode buffer layer, exhibiting an efficiency lower than that of the cell with the TiO$_2$ NRs-1 cathode buffer layer (Fig. 20g).

The conversion efficiency enhancement of the cell using the TiO$_2$ NRs-1 as the cathode buffer layer compared to the cell with TiO$_2$ dense film was attributed to (1) the single crystalline phase of the TiO$_2$ nanorods and (2) the higher electron mobility of the TiO$_2$ than that of any polymer, leading to the TiO$_2$ nanorods being able to conduct electrons much more efficiently than the PCBM polymer. In detail, because of the structure of the TiO$_2$ nanorods stretching into the active layer of P3HT:PCBM polymers, the photogenerated electrons might readily inject into the nanorods and directly transport to the FTO collecting electrode (Fig. 20h); this is unlike the case for a thin film cathode buffer layer, where the photogenerated electrons have to transport in the PCBM polymer before reaching the buffer layer, and therefore have a large probability to recombine with the holes in the P3HT because of the bulk heterojunction (BHJ) structure of the cell and low electron mobility of the PCBM

3142 | Chem. Soc. Rev., 2013, 42, 3127–3171

This journal is © The Royal Society of Chemistry 2013
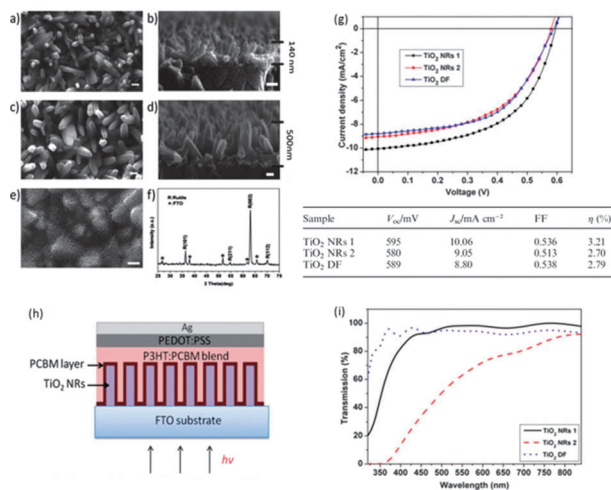
Fig. 20 TiO$_2$ nanorod array as the cathode buffer layer in inverted structure polymer solar cells. (a)–(f) Morphology and structure of TiO$_2$ nanorod array grown on an FTO glass substrate, (g) I–V curves of the cells using short TiO$_2$ nanorods (TiO$_2$ NRs-1), long TiO$_2$ nanorods (TiO$_2$ NRs-2), and TiO$_2$ dense film (TiO$_2$ DF) as the cathode buffer layer, respectively, (h) schematic drawing showing the stretching structure of an inverted solar cell using a nanorod cathode buffer layer, and (i) transmittance spectra of TiO$_2$ nanorod arrays and a film.[124] Reprinted with permission from ref. 124. Copyright 2012, Springer.
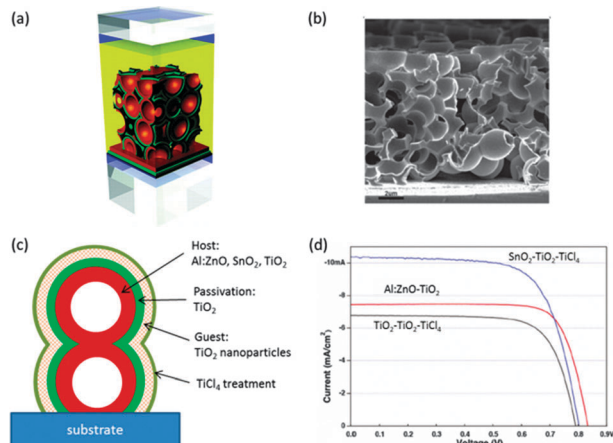
polymer. However, the nanorods that are too long would overly extend the electron transport pathway and thus increase the energy loss due to electron trapping, and nanorods that are too thick might cause a back-reflection of the light at the front interface of the cell due to scattering and therefore weaken the incident light (Fig. 20i). For this reason, the TiO$_2$ NRs-2 (*i.e.*, the long and thick nanorods) as the cathode buffer layer resulted in an efficiency lower than that for the TiO$_2$ NRs-1 (*i.e.*, the short and thin nanorods). Yodyingyong *et al.* demonstrated that the use of TiO$_2$ nanotubes, which were believed to be able to yield a larger interface between the cathode buffer layer and PCBM polymer, could collect the electrons more efficiently and achieve higher conversion efficiency in comparison to nanorods used as the cathode buffer layer in the inverted structure polymer solar cells.[125]

2.4.2 Three-dimensional host–passivation–guest (H–P–G) structure. Although TiO$_2$ in the form of nanoparticles has been announced as having the record efficiency for DSCs, the search for new materials with better electrical conduction in hope of further improving the efficiency of DSCs has never stopped. ZnO with an energy band structure similar to that of TiO$_2$ has an electron mobility of 205–300 cm^2 V^{-1} s^{-1}, much higher than that of 0.1–4 cm^2 V^{-1} s^{-1} for bulk TiO$_2$. ZnO therefore has been predicted to be the most promising candidate as an alternative of TiO$_2$ for DSC applications. However, ZnO suffers from a stability problem when soaked in ruthenium-based dyes, such as N3, N719, and black dye, which are widely used in conventional DSCs. It was found that long-term soaking of ZnO in a ruthenium dye resulted in the formation of a Zn^{2+}–dye complex instead of complete monolayer dye adsorption.[126,127] The Zn^{2+}–dye complex is inactive to electron injection, leading to poor DSC performance when compared with TiO$_2$.

Other oxides, for example SnO$_2$, also show promise. However, the dye loading for most of these oxides is very limited due to the lack of suitable surface bonds to establish connection with the ruthenium dye molecules. In addition, besides the dye adsorption problems, these high-electron-mobility oxides used in DSCs have been found to bring about serious charge recombination that is approximately 2–3 times larger than that for TiO$_2$. The idea of using a high electron mobility material for DSCs therefore does not work as expected. Such a scenario has resulted in the emergence of a three-dimensional host–passivation–guest (H–P–G) nanostructure to exploit the high-electron-mobility material for achieving highly efficient electron transport and collection in DSCs, as recently developed by Tetreault *et al.*[128]

The H–P–G structure employed microspheres of a high-mobility oxide, for example SnO$_2$ or aluminum-doped ZnO (Al:ZnO), as the *host* (H) to form the backbone of the photo-electrode film for electron transport. A layer of TiO$_2$ was coated on the high-mobility oxide core to improve the dye adsorption and establish an energy barrier to hinder the occurrence of charge recombination between the electrons in the core oxide and the oxidized redox couples in the electrolyte; such a TiO$_2$ coating shell is called the *passivation* (P) layer. To increase the internal surface area of the photoelectrode film for dye adsorption, TiO$_2$ nanoparticles were introduced to fill the gaps amongst the core–shell spheres. These interstitial TiO$_2$ nanoparticles are the so-called *guest* (G) in the H–P–G structure. Finally, a TiCl$_4$ treatment was carried out to further increase the internal surface area of the photoelectrode film and improve the connectivity between the core–shell spheres and the nanoparticles.

In the work reported by Tetreault *et al.*, the SnO$_2$ host was fabricated by a template method using polystyrene macrospheres (∼2.2 µm in diameter). These polystyrene macrospheres were eventually burnt out to enable the formation of SnO$_2$ hollow spheres with a wall thickness of approximately 90 nm. An ∼25 nm thick TiO$_2$ layer that serves as the passivation layer was coated on the SnO$_2$ spheres using atomic layer deposition (ALD). The gaps among the SnO$_2$–TiO$_2$ core–shell spheres were then filled with TiO$_2$ nanoparticles ∼17 nm in diameter. For comparison, Al:ZnO and TiO$_2$ as host materials were also studied for the formation of H–P–G structured photoelectrodes. However, the film with Al:ZnO was not treated with TiCl$_4$ in view of the dissolution of Al:ZnO in the TiCl$_4$ solution. The results of a DSC performance characterization revealed that, as expected, the photoelectrode films with the SnO$_2$ and Al:ZnO as host presented higher conversion efficiencies than the photoelectrode film with the TiO$_2$ host because of the higher electron mobility of the former over the latter (Fig. 21d and Table 2). The photoelectrode with SnO$_2$ host showed a higher efficiency than the one with Al:ZnO host due to the TiCl$_4$ treatment. It is impressive that the 842 mV open-circuit voltage achieved by the photoelectrode with SnO$_2$ host was significantly higher than the 791 mV open-circuit voltage obtained for the photoelectrode with TiO$_2$ host and those reported for TiO$_2$ nanocrystalline photoelectrodes. The higher open-circuit voltage indicates the successful suppression of charge recombination with the H–P–G structure. It is worth noting that the

This journal is © The Royal Society of Chemistry 2013

Chem. Soc. Rev., 2013, **42**, 3127–3171 | **3143**

Fig. 21 Host–passivation–guest (H–P–G) structure photoelectrode for DSC application. (a)–(c) Schematic drawing and SEM image of an H–P–G photoelectrode film, and (d) I–V curves of DSCs with SnO$_2$-hosted, Al:ZnO-hosted, and TiO$_2$-hosted photoelectrodes, respectively.[128] Reprinted with permission from ref. 128. Copyright 2011 American Chemical Society.

polystyrene macrosphere-templating method was adopted by the authors with the initial consideration of creating a photoelectrode film with large pores for solid-state dye-sensitized solar cell application, however it was opportune that the micron sized core–shell spheres were able to also generate light scattering, which contributed to improving the optical absorption of the photoelectrode and was believed to be another advantage of the H–P–G structured DSC photoelectrode.

2.5 Remarks

Based on the discussions above, it is evident that nanostructured materials improve the performance of solar cells by providing unique optical and/or electrical properties arising from their special structural characteristics. These optical or electrical properties are utilized to either increase the optical absorption of the solar cells, or improve the electron transport in the solar cell films. The optical effects of antireflection with tapered one-dimensional nanostructures and surface plasmon resonance with metal nanoparticles are efficacious in all types of solar cells. Especially in silicon-based solar cells, the antireflection has been widely used to reduce the loss of incident light, the fraction of which can be as high as ∼30% in the case of polished silicon substrates. Dye-sensitized solar cells are a good exemplification illustrating that the solar cells may greatly benefit from the nanostructures, more specifically nanoparticles. A photoelectrode film comprised of nanoparticles yields an internal surface area 1000 times larger than that of a film with bulk material for the adsorption of dye molecules, which serves for optical absorption in dye-sensitized solar cells.

The optical effect of light scattering can be utilized to enhance the optical absorption of dye-sensitized solar cells through the use of oxide nanocrystallite aggregates or mesoporous oxide beads, which provide a sufficient internal surface area for dye adsorption while forming a photoelectrode film. One-dimensional nanostructures, basically including single crystalline oxide nanowires and nanotubes, may conduct electrons well, but their use for dye-sensitized solar cells is unfortunately limited by the insufficient internal surface area of the photoelectrode film that they form. However, in polymer solar cells, especially inverted structure polymer solar cells, one-dimensional nanostructures can be employed to enhance the electron transport and collection, due to the significantly higher electron mobility of oxide nanowires or nanotubes than that of polymers. In the field of dye-sensitized solar cells, a trend is to design and synthesize three-dimensional nanostructured photoelectrodes, with emphasis on *simultaneously* increasing the optical absorption, enhancing the electron transport, and moreover satisfying the primary requirement that the photoelectrode film of a dye-sensitized solar cell must possess large enough internal surface area for dye adsorption. Quantum dot solar cells have been receiving much attention at the present time, particularly because of the multiple exciton generation effect which may allow the internal conversion efficiency of a solar cell to be over 100%. However, there are still many challenges including understanding the mechanism for the multiple exciton effect and seeking methods to lower the threshold for the generation of the multiple exciton effect so as to make it practical to create solar cells with efficiencies higher than those of existing ones.

While it has been seen that nanostructured materials indeed play a unique role in enhancing the performance of solar cells significantly, it is worth noting that the nature of nanomaterials providing a porous structure as well as a large surface area to photoelectrodes may simultaneously result in numerous boundaries in the photoelectrode films, which brings about a negative impact on the electron transport and enables it to be less efficient than crystalline thin films. Therefore, developing new nanostructures, optimizing the morphology, structure, size of building blocks of nanomaterials, and the parameters for material processing are always desired to counteract the impact of boundaries on the transport of electrons. The second challenge of using nanomaterials for energy conversion with dye- or quantum dot-sensitized solar cells is that the internal surface area of a photoelectrode film is expected to be large enough to absorb sufficient photosensitizer. However, the expansion of internal surface area is limited by the fact that exposing too much of the photoelectrode film in electrolyte may lead to increased charge recombination and thus diminish the optical absorption enhancement contributed by the additional photosensitizer. Therefore, an optimization of the porosity as

Table 2 A summary of the parameters for H–P–G photoelectrodes

H–P–G		Electron mobility of the host (cm^2 V^{-1} s^{-1})	Diffusion coefficient of the host (cm^2 s^{-1})	J_{SC} (mA cm^{-2})	V_{OC} (mV)	η
SnO$_2$–TiO$_2$–TiCl$_4$	SnO$_2$	16.5	0.423	10.4	803	5.8%
Al:ZnO–TiO$_2$	Al:ZnO	241	6.19	7.5	842	4.9%
TiO$_2$–TiO$_2$–TiCl$_4$	TiO$_2$	2.3×10^{-4} (NPs), 0.1–4 (bulk)	6×10^{-6} (NPs), 0.5 (bulk)	6.9	791	4.0%

well as the internal surface area of photoelectrode films is always an issue deserving attention. For the application of nanostructured materials in photoelectrochemical systems such as dye- or quantum dot-sensitized solar cells, the porosity of photoelectrode films is also an important factor that can affect the infiltration of electrolyte or the diffusion of redox couples. The infiltration problem of electrolyte may become particularly critical in the case of photoelectrode films consisting of nanocrystallite aggregates, in which creating large pores has been found to be difficult due to the limitations of the fabrication method.[103] Another remaining challenge of using nanostructured materials for solar cells is their incompatibility with the existing technologies for device fabrication, resulting in a low efficiency and high cost of manufacturing. This can be exemplified by the tapered nanowires or nanocone arrays, which work as an antireflection layer and present better performance in enhancing the optical absorption of solar cells compared to the conventional multilayer antireflection coating, but the nanowire or nanocone arrays are still far from practical use for antireflection, while considering that a solution-involved growth of the nanostructures is inefficient and somewhat lacks reproducibility.

To end this section, a summary of the energy band parameters of some photovoltaic materials, which are either involved in this section or are commonly used for solar cells, is provided in Table 3 to show the principles for choosing materials to construct solar cells: (1) optical absorption is primarily determined by the band gap of active materials and therefore the materials with narrow and direct band gap are preferred, and (2) the device structure should be designed by choosing materials with well-matched energy levels that may establish a suitable energy gradient allowing the charges to transport highly efficiently within the solar cell.

3. Nanostructured materials for lithium ion battery applications

A lithium ion battery consists of three major components: anode, cathode, and electrolyte. The device functions by converting a chemical potential into electrical energy *via* Faradaic reactions, which include heterogeneous charge transfer processes occurring at the surface of an electrode. The Li-ion secondary battery charging process involves an energy reversal from electrical energy to a chemical potential. These Faradaic reactions are accompanied by mass and charge transfer within the electrodes and dimensional variation; therefore, the surface area and migration distance are critical parameters that determine battery performance. The composition, crystal structure, and morphology can dictate the reaction rate and transfer processes for the electrode materials, and can be manipulated to alter the overall electrochemical performance.[129]

The development and implementation of nanostructured electrode materials has been well documented over the past decade; many excellent reviews concerning the benefits of nanostructured materials for electrochemical energy conversion and storage have already been published, to which the reader is referred.[130–132] However, nanomaterials as a whole suffer from several basic limitations that restrict their performance in energy storage applications. Thus, it is necessary to utilize either one or several exploitive techniques that can easily increase battery performance in order for renewable energy resources to achieve cost parity with traditional energy sources. The remainder of this section will highlight some of the recent developments towards tailoring nanostructures and nanostructure assemblies through the synthesis of faceted (and often high energy) structures, micro/nano-structures, mesocrystals, and the manipulation of surface chemistry for Li-ion battery electrodes with superior performance characteristics.

Table 3 Energy-band parameters of some most commonly used materials for dye- and quantum dot sensitized solar cells and polymer solar cells

Inorganic semiconductors	Band gap (eV)	Conduction band minimum (eV)	Valence band maximum (eV)
ZnO	3.2	−4.2	−7.4
TiO$_2$	3.2	−4.2	−7.4
CdS	2.4	−4.3	−6.7
CdSe	1.74	−3.49	−5.23
ZnS	3.5	−2.9	−6.4
ZnSe	2.7	−2.5	−5.2
PbS	0.4	−4.35	−4.75
PdSe	0.27	−4.93	−5.2

Organic semiconductors	Band gap (eV)	LUMO level (eV)	HOMO level (eV)
Z907	1.9	−3.6	−5.5
N719	1.7	−4.0	−5.7
N3	1.85	−3.85	−5.7
P3HT	2	−3.2	−5.2
MDMO–PPV	2.2	−3.2	−5.4
PCDTBT	1.73	−3.57	−5.3
PC$_{61}$BM	1.8	−4.2	−6.0
PC$_{71}$BM	2.2	−3.9	−6.1
ICBA	1.93	−3.74	−5.67

Electrode materials	Fermi level (eV)
ITO	−4.7
FTO	−4.4
AZO	−4.1
Al	−4.2
Ca/Al	−2.9
Au	−5.1
Ag	−4.7

Note: all energy levels are relative to vacuum energy level.

3.1 Nanostructured electrode materials for lithium ion batteries

The development and implementation of nanostructured electrode materials has led to great enhancements in Li-ion battery performance, as with many other fields.[130] The nanoscale size reduction leads to enhancements of the Li-ion battery intercalation capability by increasing the specific surface area for interfacial Faradaic reactions and the flux of Li-ions across the electrode–electrolyte interface; these effects ultimately enhance the mass and charge diffusion paths and modify the thermodynamics (compared to the bulk), which facilitates phase transitions. However, the most dominant and substantial

advantages imparted by nanostructures is drawn from their enhancement of the kinetics and related diffusivities. The Li-ion diffusion time for lithiated or non-lithiated transition metal oxides is proportional to the square of the diffusion path length:

$$t = L^2/D \qquad (8)$$

where L is the diffusion length and D the diffusion constant. The reduction of the electrode particle size into the nanometer regime tremendously improves the intercalation kinetics and ultimately enhances the overall degree of intercalation. Several studies have also revealed that the implementation of nanostructures as electrode materials has led to an enhancement of the specific capacity beyond the theoretical limits.[133,134] The increased storage capacity has been attributed to the confined dimensions of nanostructures that make the surface and grain interface effects more prominent. Ultimately, a pseudo-capacitive storage mechanism will begin accommodating lithium ions on the surface/interface of the particles when they are below a critical particle size.[133] Therefore, nanostructures of a critical size can undergo an interfacial adsorption mechanism in addition to the traditional bulk intercalation process, and it is possible to modify the nanostructured material phase transition boundary to intercalate more lithium. These studies also revealed that the Li-ion and electron potentials can be modified through the use of exceedingly small particles, producing a change in the electrode potential and overall reaction thermodynamics.[135] All of these factors make it possible for nanostructured battery electrodes to operate at a higher rate; the use of nanomaterials can also enhance the cycling performance of the material by alleviating some of the lattice strain experienced during cycling due to the (de)intercalation of lithium.[135,136]

The benefits of nanostructured metal oxide electrodes have been well documented throughout the literature. Wagemaker *et al.* compared the lithium ion intercalation performance of anatase TiO$_2$ micro- and nanoparticles.[137] The size of the anatase TiO$_2$ nanoparticles was incrementally altered in order to investigate the nano-size effects. It was determined that the Li-ion solubility was greater with decreasing particle size, and increased from 0.55 to 0.7 Li$^+$ per formula unit when the micron-sized TiO$_2$ particles were replaced with nanoparticles smaller than 40 nm. The discrepancy in the quantity of inserted Li$^+$ was ascribed to a more homogeneous, and Li-rich, phase in the nanoparticles compared with the micron-sized particles that had coexisting Li-rich/poor phases because they were too large for homogeneous Li$^+$ penetration.[138] Ganapathy *et al.* also revealed that the Li$^+$ diffusion rate limiting two-phase boundary between electrode particles has an activation energy of approximately 50 kJ mol^{-1}, but nanomaterials smaller than 40 nm did not have the phase boundary and had an activation energy of 10–25 kJ mol^{-1}.[139] Hu *et al.* also corroborated the enhanced electrochemical effects of nanostructuring TiO$_2$ as a Li-ion battery electrode material.[140] They revealed that the discrepancy in intercalated Li$^+$ could be attributed to dissimilar diffusion along the *ab*-plane, and that Li$^+$ surface storage on the nanoparticles is energetically more favorable than bulk insertion.

While anatase TiO$_2$ and its derivative structures are well-studied metal oxide electrode materials, it should be noted that layered intercalation compounds are one of the more popular device candidates amongst metal oxide electrodes. These layered compounds, for which nearly all of the research and commercialization of cathode materials has been focused, can be further designated into two classes. The first class comprises the layered compounds with an anion close-packed or nearly close-packed lattice where the electro-active transition metal ions occupy alternating layers, and lithium is inserted in the unoccupied layers. Both LiTiS$_2$ and LiCoO$_2$, the current commercial cathode of choice, are prime examples of this class of compound. The spinel structured compounds may be classified as a sub-group within this class because the transition metal ions occupy all the layers. Nanostructured Li$_{4+x}$Ti$_5$O$_{12}$ spinel has demonstrated superior electrochemical performance when compared to its bulk counterpart due to increased Li-ion occupancy.[141] These results serve as a direct reflection of the enhanced kinetics and transport properties of nanostructured electrodes because the Li$_{4+x}$Ti$_5$O$_{12}$ spinel is a zero-strain material. The second class of layered metal oxide compounds can be classified by their more open structures. Primary examples of these structures are the layered vanadium oxides and tunneled manganese dioxide; the transition-metal phosphates, such as olivine LiFePO$_4$, can also be grouped under this structural classification. The benefits of nanostructuring have been documented for these layered materials as well. Uniform films of V$_2$O$_5$ were formed on FTO substrates through a combination of cathodic deposition and catalyzed gelation. The homogeneous films were composed of microflakes that ranged from 0.5 to 1.5 μm in diameter, and each flake was composed of nanoparticles measuring 20–30 nm in diameter with 10 nm gaps separating adjacent nanoparticles.[142] Conversely, similar processing routes with the addition of a block copolymer surfactant yielded a porous V$_2$O$_5$ structure composed of nanoparticles and pores approximately 100 nm in size.[143] Not surprisingly, the smaller particle and pore size of the surfactant-free specimen led to far greater lithium intercalation capacity (405 *vs.* 275 mA h g^{-1}), rate performance (70 C *vs.* 60 C), and cyclic stability (200 *vs.* 40 cycles). Thinner films displayed similar benefits when compared to thicker films composed of the same electro-active material.

The development of silicon based anodes for Li-ion batteries has also received a considerable amount of interest over the past several years. The Li–Si binary system indicates that an individual silicon atom can accommodate the insertion of 4.4 lithium ions, yielding one of the highest known theoretical charge capacities (4200 mA h g^{-1}); additionally, the discharge potential of silicon is quite low, and it is already a highly processed material. Although this theoretical capacity value is eleven times larger than that of the current commercially used graphite anodes, the use of silicon as an anode material is limited because the insertion of 4.4 Li-ions is accompanied by a 400% volume expansion of the lattice. This tremendous expansion results in cracking and disintegration of the electrode, with active material loss *via* reduced electronic contact, giving

way to severe capacity fade. Such has been the case for past studies involving Si bulk films and micrometer-sized particles, where capacity fading and short battery lifetimes were attributed to the pulverization and loss of electrical contact between the active material and the current collector. Fortunately, the use of Si nanostructures such as nanowires can alleviate these issues because there is a critical particle size below which fractures will not propagate further. Huggins and Nix[144] calculated the critical size for particle fracture upon lithiation as:

$$h_{C} = \frac{23}{\pi} \left(\frac{3k_{IC}}{B\varepsilon_{T}} \right)^{2} \qquad (9)$$

where h_{C} is the critical crack size, K_{IC} is the fracture roughness in MPa $\sqrt{m}$, B is the biaxial Young's modulus of the material, and ε_{T} is the total strain. For silicon, the fracture toughness is 10 MPa $\sqrt{m}$, and the strain associated with the insertion of 4.4 Li^{+} per Si ($Li_{22}Si_{5}$) is approximately 400%. Therefore, the critical particle size below which fracturing supposedly does not occur is estimated to be 75 nm.

Experimentally, Li et al. showed that composite anodes of Si–C nanoparticles ranging from 50 to 100 nm in size have better cycling performance than those in the micrometer range.[145] Alloy particles within the nano-regime can accommodate a larger degree of volume variation because they often display higher plasticity and deformability. The control and tailoring of these considerations resulted in a nano-Si composite anode material with an extremely high and reversible capacity that exhibited none of the capacity fading seen in the micrometer sized material. Chan et al. went on to demonstrate that Si nanowires grown through the vapor–liquid–solid method were better able to accommodate large volume changes without the initiation of fracturing due to their small diameter, one dimensional confinement of charge transport, and enhanced contact with the current collector. Additionally, no binders or conductive additives were required to compensate for material short-comings since every nanowire was attached to the current-carrying electrode; however, the capacity retention at the 2 C rate was less than 50% of the initial capacity.[146]

While Li^{+} surface storage and increased fracture resistance are performance benefits inherent to many nanostructured electrode materials, an even more complex interaction has been observed in nano-sized $LiFePO_{4}$ because of its incomplete miscibility gap (region in a phase diagram in which two phases with nearly the same structure have no solubility in one another). Meethong et al. showed that the miscibility gap in pristine $LiFePO_{4}$ diminishes with decreasing nanoparticle size, suggesting that the miscibility gap completely disappears below some critical value.[147] The enhanced solubility of Li in nano-sized $LiFePO_{4}$ can be ascribed to the presence of multiple phases in the individual particles. The coexistence of two crystallographic phases within one particle leads to a domain-wall-related energy penalty, which is determined by the strain prompted from the difference in the lattice parameters and can destabilize the two-phase coexistence in smaller particles. Nanostructures have been utilized to increase the equilibrium

compositions and effectively reduce the lattice mismatch between coexisting phases. Therefore, the energy gain associated with phase separation will drop with decreasing particle size, and the misci-bility gap will gradually diminish.[148] The miscibility gap began to decrease while the solubility increased starting with nanoparticles approximately 100 nm in diameter, and showed a strong effect in particles smaller than 35 nm.[149] Changes in the miscibility gap were ascribed to particle size associated modifications in the molar free energy of mixing for either one or both phases. The associated particle size effects were also speculated to emerge from the relative contributions of the particle-matrix surface energy and stress, and/or the coherency or compatibility stresses in the coherently interfaced two-phase particles.[147]

Herein, the remainder of this section will focus on some of the recent developments towards tailoring nanostructures and nanostructure assemblies for fabricating electrodes that will not fall victim to the damaging effects associated with nanomaterials. In addition, the exposure of specific (and often high energy) facets, micro/nano-structures, mesocrystals, and surface/defect chemistry manipulation for Li-ion battery electrodes with superior performance characteristics will be discussed.

3.2 Exposure of specific surface facets

It has been demonstrated that the control of particular electrode material crystal facets is beneficial for lithium ion storage. These increased attributes can be ascribed to the unique surface properties of specific facets, including the surface energy and diffusion barrier.[150,151] Yang et al. were amongst the first to synthesize anatase TiO_{2} single crystals with a high percentage of reactive (001) facets compared to the more energetically preferred (101) facets, which have surface energies of 0.9 and 0.44 J m^{-2}, respectively.[152] This discrepancy in the energy values was proven experimentally by reversing the relative stability of the facets by terminating the surface with fluorine through the use of hydrofluoric acid. The fluorine terminated surfaces were later cleaned by heat treatment, whereupon the crystal structure and morphology were retained. Many investiga-tions have since been conducted that analyze the novel properties of these faceted structures for environmental, energy storage, biomedical, and catalytic applications.[153]

Of particular interest for such tailored materials is the increased lithium ion storage potential of the exposed high energy facets. Lithium insertion occurs faster on the (001) TiO_{2} surface rather than the (101) surface because of a higher charge transfer rate constant (10^{-8} vs. 2×10^{-9} cm s^{-1}) and chemical diffusion coefficient (7×10^{-14} vs. 2×10^{-13} cm^{2} s^{-1}) for Li^{+} insertion.[151] The charge transfer and chemical diffusion coefficient for TiO_{2} is greatest along the (001) facet, and exposing these facets can result in a lower energy barrier for faster and more Li^{+} intercalation. Despite the relatively high percentage of (001) facets, the specific surface area of the TiO_{2} crystals was low because they were relatively thick along the [001] direction. With these considerations in mind, Wu et al. set out to improve electrochemical performance by reducing the [001] direction thickness and increasing the two-dimensional lateral size of the (001) plane by synthesizing TiO_{2} nanosheets
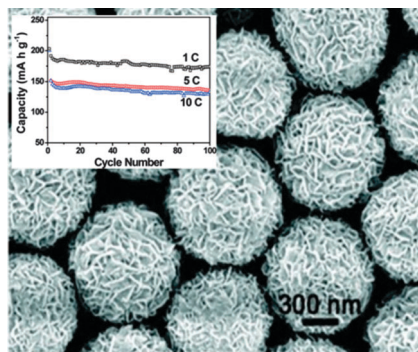
Fig. 22 FESEM image of spontaneously assembled anatase TiO$_2$ nanosheet microspheres synthesized under solvothermal conditions, and (inset) cycle stability at various current rates.[159] Reprinted with permission from Chen et al., J. Am. Chem. Soc., 2010, **132**(17), 6124–6130. Copyright 2010 American Chemical Society.

with high-energy facets.[154] While the nanosheet surfaces were dominated by (001) facets, they were initially stabilized by oleylamine which was then removed by calcination; however, this approach led to agglomeration and coarsening of the nanosheets. Chen et al. circumvented this issue by synthesizing hierarchical spheres from large ultrathin anatase TiO$_2$ nanosheets with nearly 100% exposed (001) facets.[155,156] Even at a high current rate of 20 C (3400 mA g^{-1}), a reversible capacity of 95 mA h g^{-1} could still be delivered, as evidenced in Fig. 22. Similar results for analogous morphologies have been demonstrated by several other groups as well.[157,158]

The individual nanosheets adopted a random orientation, which resulted in a three-dimensional highly nanoporous structure with a specific surface area of $\sim$170 m^2 g^{-1}. The nanosheet hierarchical structures showed excellent cycle and rate performance when investigated as anode material for Li-ion batteries; the specific capacity was 140 and 100 mA h g^{-1} when the electrode was discharged at the high current rate of 10 and 20 C, respectively, as seen in the inset of Fig. 22. The high Coulombic efficiency, excellent capacity retention, and superior rate behavior were ascribed to the inherently short transport path lengths, preferential orientation of the nanosheets, and size confinement of the nanosheets themselves.

Dylla et al. went on to demonstrate that the intercalation of Li$^+$ in TiO$_2$(B) nanosheets is superior to TiO$_2$(B) nanoparticles due to the exposure of highly reactive facets that decrease the diffusion barrier during lithium intercalation.[150] Differential capacity plots revealed that the TiO$_2$(B) nanosheets have a greater influence from surface effects that would change the overall charge–discharge behavior, and the nanoparticles displayed a more discrete redox behavior. Density functional theory with energy penalty (DFT+U) calculations were then performed, and elucidated the varying lithiation mechanisms for the different morphologies. For the TiO$_2$(B) nanoparticles, the A2 sites near the equatorial TiO$_6$ octahedra are initially filled, followed by A1 sites near the axial TiO$_6$ octahedra. Conversely, the TiO$_2$(B) nanosheets incrementally fill the C sites, followed by the A2 and A1 sites. This variance in the method of lithiation is attributed to the elongated geometry of the

nanosheet that effectively reduces lithium interaction between the C and A2 sites. Overall, this study further verifies that the exposure of specific high energy facets can be advantageous towards achieving enhanced lithiation dynamics. Similar calculations have also yielded the same conclusions for spinel Li$_{4+x}$Ti$_5$O$_{12}$.[160]

The benefits of faceting have also been observed for other metal oxide electrode materials. LiMn$_2$O$_4$ nanosheets composed of single-crystalline nanorods with exposed (111) facets demonstrated favorable attributes for energy storage applications because of their two-dimensional nanoporosity and exposed (111) facets.[161] From a Li-insertion performance standpoint, nearly 100% of the initial capacity can be retained after 500 cycles at a 1 C discharge rate using the nanoporous nanosheets as a cathode; at a discharge rate of 25 C, the capacity retention is about 86% of the initial capacity after 500 cycles. These discharge values were approximately 2.5 times better than solid state synthesized LiMn$_2$O$_4$ particles. The enhancement in capacity was ascribed to a more uniform, thin, and stable solid electrolyte interphase (SEI) layer forming on the (111) facets that could suppress structural and volumetric changes.

Liang et al. successfully synthesized hierarchical LiV$_3$O$_8$ nanofibers from nanosheets composed of exposed (100) facets using electrospinning combined with calcination, which showed great potential as anode materials for aqueous Li-ion batteries.[162] An issue that plagues aqueous lithium ion battery systems is the potential of proton intercalation in place of Li$^+$ intercalation, and is responsible for the capacity fading typically seen in such set-ups. The (100) facet of the LiV$_3$O$_8$ structure has smaller and less numerous channels to accommodate Li$^+$ insertion, which makes it more difficult for H$^+$ to intercalate into the anode host. Therefore, the enhancement in electrochemical performance is a result of the high percentage of exposed (100) facets that may effectively alleviate proton co-intercalation into the electrode materials. Correspondingly, the LiV$_3$O$_8$ nanofibers from nanosheets composed of exposed (100) and bulk LiV$_3$O$_8$ materials exhibited a discharge capacity of 105 and 62 mA h g^{-1}, respectively, when cycled at 60 mA g^{-1}.

Li$^+$ insertion dependence on exposed crystal facets has also been observed in metal phosphates. LiFePO$_4$ nanoplates with crystal orientation along the (101) facet and (011) facet present similar reversible capacities at low current densities, but the (011) facet shows inferior performance at higher rate.[163] The approximate values of the (101) and (011) faceted structures were 160 mA h g^{-1}, but then differentiated at 148 and 28 mA h g^{-1} at 10 C, respectively. The results indicate that Fe$^\bullet_{Li}$ anti-site defect concentration may account for the availability of electrochemically active LiFePO$_4$, while the crystal orientation contributes for rate capability only, further verifying that control of faceted surfaces is a powerful means of enhancing electrode performance. LiMnPO$_4$ microspheres with different crystallographic orientations were assembled from plates, wedges, and prisms. The Li$^+$ insertion performance of the LiMnPO$_4$ microspheres assembled with plates was far better than the other primary nanoparticle units due to the exposure of (010) facets as well as the confined thickness along the [010] direction allowing for fast Li$^+$ diffusion

and a short diffusion length.[164] The plate-assembled microspheres ultimately demonstrated discharge capacities of 130.3 mA h g^{-1} at 0.05 C, 114.9 mA h g^{-1} at 0.1 C, and 96.8 mA h g^{-1} at 0.2 C, values which were far superior compared to the microspheres composed of wedge or prism nanoparticles.

Additionally, the effects of surface facet control can be seen for lithium alloying elements as well. For Si insertion materials, Jung et al. revealed through DFT calculations, with a slab representation of the surfaces, that once the Li$^+$ is incorporated into the Si surface, it diffuses faster by at least two orders of magnitude along the [100] direction than along the [111] direction.[165] The notable difference between the Li$^+$ insertion behaviors in the (100) and (111) surfaces is a distinct rate-determining step; more explicitly, these limitations are the surface incorporation for (100) and subsurface diffusion for (111). These results were then assessed experimentally, where it was determined that a phase boundary separating the crystalline silicon from the amorphous lithiated phase was faster for (110) silicon than along the (100) and (111) orientations.[166] These results imply that subsurface diffusion can play a more important role than surface incorporation in determining the overall intercalation rate, and that the kinetics of Li$^+$ surface incorporation must be enhanced by metal doping or modification of the SEI to reduce the surface incorporation barrier.

3.3 Micro/nano-structured electrode materials

While nanosized electrode materials are advantageous in terms of kinetics and capacity, their practical application suffers from low thermodynamic stability and a high propensity to undergo secondary reactions because of their confined size and high surface energy. Therefore, the use of kinetically stabilized nanostructures should be considered. Over the past several years, significant studies have been conducted examining the synthesis and performance of heterogeneous structures. While heterogeneous structures typically refer to the combination of two or more materials, in this case it refers to architectures displaying more than one size scale (i.e., micro/nano). The design of micro-structurally composed nanoparticles, for instance, can circumvent the thermodynamic instability, undesired side reactions, high processing costs, and potential nano-toxicity effects associated with nanoparticle synthesis and processing.[130,167,168]

For example, micro/nano-structures of the metastable monoclinic (B) phase of vanadium dioxide were synthesized by Zhang et al. using a polymer capping reagent and hydrothermal processing conditions.[169] The final product displayed a flower-like morphology assembled of single-crystalline nanosheets, as shown in Fig. 23a. It was determined that the flower-like morphology was developed through a self-assembly and Ostwald ripening process, where the overall flower-like structure was approximately 1–1.5 μm in diameter composed of nanosheets (the petals of the flower in this case) 20–30 nm thick. The obtained material was employed as the active electrode material for an aqueous Li-ion battery system paired with a LiMn$_2$O$_4$ counter electrode. The VO$_2$/LiMn$_2$O$_4$ cell showed an excellent initial capacity when cycled at 60 mA g^{-1}, but suffered from significant capacity fading upon cycling, as seen in Fig. 23b.
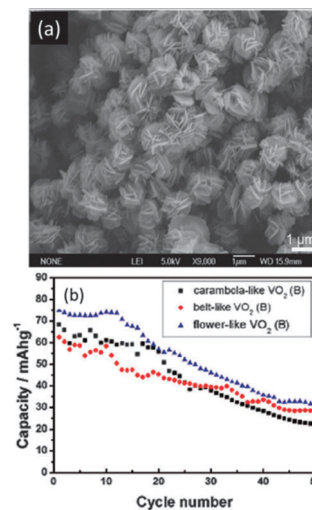

Fig. 23 (a) FESEM image of the as-prepared flower-like VO$_2$ synthesized via a hydrothermal route using a polymer capping agent, and (b) corresponding cyclic stability of the VO$_2$/LiMn$_2$O$_4$ aqueous cell operating at 60 mA g^{-1} within the voltage range of 1.65–0.5 V.[169] Reprinted with permission from Zhang et al., J. Phys. Chem. C, 2009, 113(33), 15058–15067. Copyright 2009 American Chemical Society.

The high initial Li$^+$ intercalation performance was attributed to the interconnecting single crystalline nanosheets, which decreased the charge and mass transfer diffusion paths.

Similar flower-like morphologies composed of single crystalline nanosheets were also observed in other electrode material systems, such as LiMnPO$_4$, SnO$_2$, and LiFePO$_4$.[159,170,171] All of these reported studies stated that their respective morphology evolved through the capping of the primary nanoparticles with surfactant followed by the formation of preferential arrangements and subsequent growth. The LiMnPO$_4$ product showed notable capacity retention, but the specific capacity values were not good. The low Li$^+$ intercalation potentials could be overcome by modifying the nanosheets to grow along the [010] axis that exhibits a preferential Li$^+$ diffusion pathway. The other flower-like morphology systems showed outstanding electrochemical performance both for prolonged cycling and at high current rates.

3.3.1 Hollow micro/nano-structures. A great deal of recent research efforts have also focused on the study of hollow nanostructured materials, such as nanotubes and hollow spheres, that demonstrate unique characteristics due to their morphology.[172] Hollow nanostructured materials have been known to exhibit large surface area, low density, and enhanced surface permeability because of their inner cavities; such materials have been used in a wide range of applications such as Li-ion batteries, catalysts, optoelectronic sensors, and drug-delivery systems.[173] The morphology of hollow nanostructured materials is responsible for increasing the electrochemical performance of Li-ion batteries in two ways. First, the void within hollow nanostructured material can serve as a buffer against any localized volume change experienced during the Li$^+$ intercalation–deintercalation process, thereby improving the cyclic stability; and secondly, the large surface area and
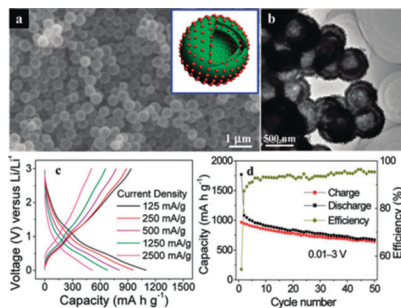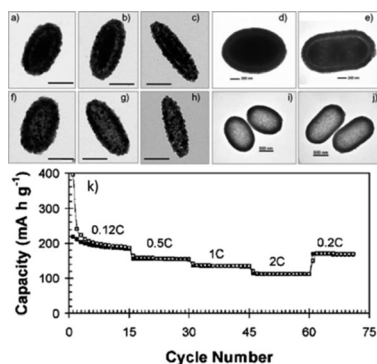
Fig. 24 (a) SEM and (b) TEM image of V$_2$O$_5$–SnO$_2$ double-shelled nanocapsules chemically assembled *via* a one-pot solution method. The inset in (a) shows a schematic structure of a double-shelled nanocapsule. The red spheres represent SnO$_2$ nanocrystals, and the green double shells represent the V$_2$O$_5$ matrix. (c) Charge–discharge curves at different current densities. (d) Capacity (left) and efficiency (right) *versus* cycle number at a current density of 250 mA g^{-1}, showing the capacity retention upon cycling.[177] Reprinted with permission from Liu *et al.*, *J. Am. Chem. Soc.*, 2009, **131**(34), 12086–12087. Copyright 2009 American Chemical Society.

decreased Li$^+$ diffusion distance in hollow nanostructured electrodes greatly enhances the specific capacity while decreasing the packing density.[174–176]

Liu *et al.* synthesized SnO$_2$–V$_2$O$_5$ nanocapsules approximately 400 nm in diameter through a combination of Ostwald ripening processes.[177] Fig. 24a and b display the double-shelled structure and hollow interior as confirmed by SEM and TEM characterization, respectively. When tested as an anode material, the nanocapsules exhibited an excellent cycle stability of 673 mA h g^{-1} over the course of 50 cycles at a discharge rate of 250 mA g^{-1}; the rate capability of the nanocapsules also provided encouraging results (Fig. 24c and d).[177]

Lou and Archer established a templating scheme based on monodisperse nonspherical hematite (α-Fe$_2$O$_3$) colloids that yielded nonspherical (ellipsoidal) metal oxide hollow or core–shell particles as exhibited in Fig. 25.[178] Additionally, the hematite cores surrounded by the TiO$_2$ shell could be converted to magnetite (Fe$_3$O$_4$) cores to produce tailored magnetic multi-functional particles. It was also revealed that the processing
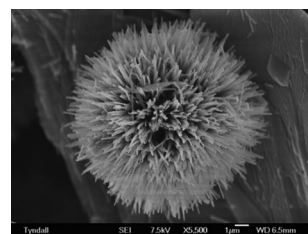
conditions could be altered to adjust the aspect ratio of the as-synthesized product. The as-prepared hematite–TiO$_2$ core–shell particles were investigated as anode material for Li-ion batteries. Fig. 25k shows the commendable cycle life and rate capability of the core–shell TiO$_2$ particles.

More recently, Wu *et al.* synthesized double-walled silicon nanotubes that demonstrated superb intercalation and lifetime performance when tested as anode material.[179] The inner wall of the double-walled nanotube structure consisted of an active silicon nanotube surrounded by an ion-permeable silicon oxide shell. Due to the novel design, the electrolyte solution is only in contact with the outer surface, and cannot enter the hollow inner space, through which Li$^+$ permeates to reach the active material. The outer oxide shell also constrained the Si expansion to the inner void, eliminating pulverization and capacity degradation. This unique feature also worked to stabilize the SEI film. The material was cycled over 6000 times in the half cell configuration while retaining a capacity greater than 600 mA h g^{-1} when cycled at 12 C. The excellent electro-chemical properties were ascribed to the novel engineered nanostructure that exploits the inherent Li$^+$ intercalation capability of Si while maintaining battery performance.

While the current literature is full of studies detailing the results of spherical and tubular hollow nanostructures, hollow assemblies are in no way limited to these morphologies. The so-called 'urchin' structure is one such morphology, and is characterized by a microscale spherical core (solid or hollow) from which numerous nanotubes (hollow) or nanofibers (solid) are extruded.[180,181] A representative image of such a structure is presented in Fig. 26. The protruding nanoparticles comprising the urchin-like morphology can potentially enhance the conductivity of the electrode, and ultimately the electrochemical response, by forming a three-dimensional network of interconnected nanoparticles. The void spaces formed between these interconnects can also enhance the contact between the electrode material and the electrolyte.[182]

An even more novel derivation of hollow nanostructured electrode materials is those where the central cavity is filled with nanoparticles of some secondary material, such as a hollow nanosphere loaded with electroactive nanoparticles. As revealed in Fig. 27, Zhang *et al.* successfully encapsulated Sn nanoparticles in hollow elastic carbon spheres approximately

Fig. 25 TEM images of five types of hematite–TiO$_2$ core–shell particles (a–e) and their corresponding TiO$_2$ hollow particles after removal of hematite cores (f–j), respectively, scale bars in (i) and (j) are 500 nm, all others are 200 nm. (k) Cycling performance at various discharge rates.[178] Reprinted with permission from Lou *et al.*, *Adv. Mater.*, 2008, **20**, 1853–1858. Copyright 2008 Wiley-VCH.

Fig. 26 SEM of an individual nano-urchin synthesized by a simple chemical route using an ethanolic solution of vanadium tri-isopropoxide and alkylamine hexadecylamine for 7 days at 180 °C.[180] Reprinted with permission from O'Dwyer *et al.*, *Chem. Mater.*, 2006, **18**(13), 3016–3022. Copyright 2006 American Chemical Society.

3150 | *Chem. Soc. Rev.*, 2013, **42**, 3127–3171

This journal is © The Royal Society of Chemistry 2013

500 nm in diameter and 20 nm thick.[183] Each carbon nanosphere contained approximately 5–10 Sn nanoparticles. The remaining void space within each nanosphere combined with the confining carbon shell meant that the Sn nanoparticles would not experience pulverization (and accompanying cyclic fading) due to volume expansion and contraction experienced during lithiation. Fig. 27c displays the moderate cycle stability and good initial discharge capacity. Lee et al. also reported the synthesis of single Sn nanoparticles loaded in hollow carbon nanospheres; however, the capacity and cycle stability suffered, most likely due to the low tap density of the electrode material.[184]
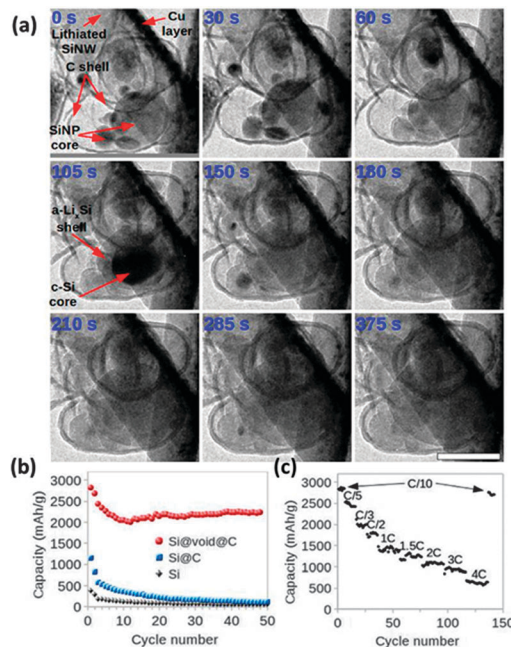
Zheng et al. also developed templated hollow carbon nanofiber encapsulated sulfur as cathode material.[185] The template structure facilitated sulfur infusion into the hollow fibers and prevented sulfur from coming into contact with the exterior carbon wall. The high aspect ratio of the carbon nanofibers provided an ideal structure for trapping polysulfides while the thin carbon wall permitted rapid Li$^+$ kinetics. The confined nanoscale dimensions of the nanofibers lead to a large surface area per unit mass for Li$_2$S deposition during cycling and reduced electrode material pulverization. A high specific capacity of approximately 730 mA h g^{-1} was recorded after 150 cycles at a rate of 0.2 C.

Liu et al. have recently investigated carbon coated single Si nanoparticles with an inherent void space.[186] Single Si nanoparticles with an average size of 100 nm were coated with a 5–10 nm thick amorphous carbon shell, with an 80–100 nm void space surrounding the Si nanoparticle (Si@void@C). The main advantages of this adopted morphology was that the carbon shell acted as a framework that allocated for the growth of a stable SEI layer while preventing fracture of the Si nanoparticles due to volume expansion; lithiation of the Si occurred by Li diffusion through the carbon shell into the Si core. Fig. 28 shows a sequence of images collected from the in situ TEM investigation of the Si@void@C particles at various times.

Prior to lithiation, pristine Si nanoparticles were clearly observed and contained within a carbon shell. Subsequently,

Fig. 28 (a) In situ TEM characterization of Si@void@C expansion during electrochemical lithiation, where the silicon particles are observed to expand within the outer carbon shell. Scale bar: 200 nm. (b) Galvanostatic cycling of different silicon nanostructures (PVDF binder). All samples were cycled at 0.02 C for the first cycle, 0.5 C for the second cycle, and 0.1 C for the later cycles. (c) Delithiation capacity of Si@void@C with alginate binder cycled at various rates from 0.1 C to 4 C.[186] Reprinted with permission from Liu et al., Nano Lett., 2012, **12**(4), 3315–3321. Copyright 2012 American Chemical Society.

the Si particles experienced significant volume expansion as Li$^+$ diffused through the carbon coating and intercalated the Si particles. After 105 s of charging, an amorphous Li$_x$Si shell–crystalline Si core structure was formed as the Si particles were partially lithiated. The diameter of a typical Si particle increased from ∼185 to ∼300 nm after lithiation was complete (375 s charge time). The thickness of the carbon layer also increased from 5–10 nm to 20 nm, indicating that the carbon coating was also storing Li$^+$. In situ TEM clearly demonstrated that fractures were not observed during electrochemical cycling of these particles, which resulted in their excellent electrochemical properties as derived from the yolk–shell structure. It is evident from Fig. 28b that the yolk–shell morphology was far superior to simply coating Si nanoparticles with carbon; the Si@void@C particles also demonstrated a moderate capacity of 630 mA h g^{-1}, while the initial capacity is relatively maintained even after 150 cycles.

3.3.2 Mesocrystals. Over the past several decades, nanoparticle formation and application integration has been the subject of much academic and industrial research. Nanoparticles are the focus of such intrigue due to their novel properties and tunable functions that can be utilized in a wide range of applications.[187] Recently, there has been much effort in the formation and subsequent understanding of ordered nanoparticle superstructures with a vast range of architectures, particularly mesocrystals. Mesocrystals, short for mesoscopically structured crystals, are crystallographically oriented nanoparticle superstructures

Fig. 27 (a) SEM and (b) TEM image of Sn encapsulated carbon spheres. The inset in (a) is a close view of a single broken carbon spherical shell studded with Sn particles. (c) The discharge–charge capacity profiles of Sn encapsulated carbon spheres in the 5 mV–3 V (vs. Li$^+$/Li) voltage window and 0.2 C; the inset shows the initial cycle.[183] Reprinted with permission from Zhang et al., Adv. Mater., 2008, **20**, 1160–1165. Copyright 2008 Wiley-VCH.

and have received much attention since first being introduced by Cölfen and Antonietti.[188–190] Until recently, mesocrystals were only studied in biomineral materials, but current research efforts have shifted to the development of mesocrystalline organic molecules, metal oxides, and other functional materials.[191]

Colloidal crystals and supercrystals or nanocrystal superlattices offer novel nanoparticle arrangement; however, such assemblies do not take into account individual nanoparticle orientation. Mesocrystals can be classified by their high degree of crystallinity, high porosity, and subunit alignment along a crystallographic register. These highly desirable properties are due in part to mesocrystal formation mechanisms, which are still poorly understood, and make mesocrystals the ideal material candidates for catalysis, sensing, and energy storage and conversion applications. Porous materials with large specific surface areas have been shown to enhance the performance of lithium ion battery electrode materials because of more prevalent and uniform pores that ease intercalation by decreasing the Li^+ diffusion distance. Secondary battery cathodes constructed out of mesocrystalline materials could benefit tremendously from the inherent and uniform porosity of the well-defined crystallographic register with which the nanoparticles orient themselves.[187]

Mesocrystal growth often proceeds via the aggregation of precursor units, rather than by the classical ion-by-ion growth mechanism. This non-classical growth process can be attributed to the generation of crystals with hierarchical structures and complex morphologies.[189] Organic additives are commonly used to facilitate this process, but are not required by any means.[192] The oriented assembly of nanoparticles leads to the formation of mesocrystals where the constituting crystallites are arranged in a crystallographic register and the product particles demonstrate single crystal behavior. Identification of mesocrystals has proven to be difficult but can be achieved via the detection of a number of features including high porosity/large surface area and evidence of mesoscopic subunits as viewed from transmission electron microscopy.[193]

3.3.2.1 Vanadium oxide. Several studies focusing on the synthesis and performance of mesocrystalline materials as either anode or cathode in lithium ion batteries have already been reported. Cao et al. synthesized hollow V_2O_5 microspheres composed of nanorods via self-assembly (Fig. 29).[194]
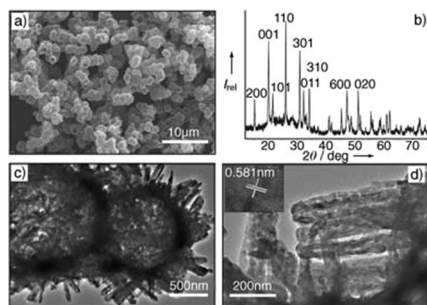
Hollow microsphere precursors of vanadyl glycolate composed of assembled nanorods were first synthesized utilizing the polyol process, and were then transformed to V_2O_5 with a simple annealing step. No change in the morphology was observed upon annealing. The individual nanorods comprising the structure were approximately 200 nm in diameter and varied in length, while the overall spherical structures were approximately 2 μm in diameter. The structures were successfully able to intercalate up to one Li^+ per V_2O_5 formula unit, and showed moderate capacity retention up to 15 cycles with an initial discharge capacity of 286 mA h g^{-1}.[194] It was determined that interconnecting nanoparticles between the self-assembled nanorods lead to a reduction in the Li^+ diffusion distance, thereby increasing the kinetics of the material and the overall electrochemical performance. It has since been revealed that hollow structures can result in favorable enhancements in capacity retention with cycling due to the presence of the inner cavity that can accommodate cycling induced strain due to the (de)intercalation of Li^+.[173]

3.3.2.2 Titanium oxide. Ye et al. synthesized ellipsoidal anatase TiO_2 mesocrystals approximately 380 nm in length and 280 nm in diameter though the solvothermal reaction of acetic acid and tetrabutyl titanite, the end result of which is shown in Fig. 30.[195] The mesocrystalline structures were composed of oriented nanoparticles ranging between 10–20 nm in diameter. Selected area electron diffraction (SAED) measurements confirmed the single crystalline characteristics of the mesocrystal and revealed that the elongated ellipsoid direction corresponded to the [001] direction as observed in the inset of Fig. 30c.

The mesocrystalline nature of the particles was most likely achieved through the oriented attachment mechanism and infusion between the TiO_2 nanoparticles, leading to a decrease of the interfacial nucleation sites for the rutile phase.
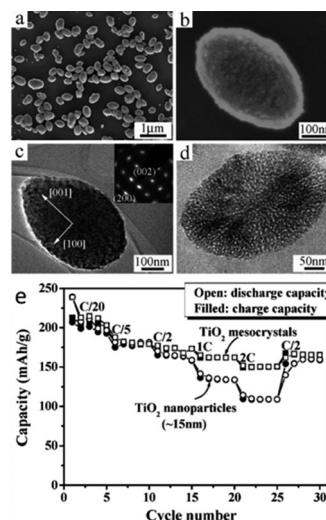

Fig. 29 (a) SEM image, (b) XRD spectrum, and (c, d) TEM images of self-assembled V_2O_5 microspheres composed of nanorods synthesized using a mediated polyol process.[194] Reprinted with permission from Cao et al., *Angew. Chem., Int. Ed.*, 2005, **44**, 4391–4395. Copyright 2005 Wiley-VCH.

Fig. 30 SEM (a, b) TEM, (c, d) HRTEM images, and (e) electrochemical performance of nanoporous anatase TiO_2 mesocrystals synthesized through mesoscale assembly in the tetrabutyl titanate–acetic acid system without any additives under solvothermal conditions.[195] Reprinted with permission from Ye et al., *J. Am. Chem. Soc.*, 2011, **133**(4), 933–940. Copyright 2011 American Chemical Society.

3152 | *Chem. Soc. Rev.*, 2013, **42**, 3127–3171

This journal is © The Royal Society of Chemistry 2013

The formation of the TiO_2 mesocrystals through the oriented attachment mechanism also decreased the number of grain boundaries existing between individual TiO_2 nanoparticles, thus resulting in facile electronic conduction and fast Li^+ transport between the electrolyte and the mesocrystal electrode. This speculation was validated when the mesocrystal TiO_2 anode was compared to a TiO_2 anode composed of nanoparticles of approximately the same size as the mesocrystalline subunits (Fig. 30e). The mesocrystalline anode demonstrated good rate capability and outperformed its nanoparticle counterpart at higher current rates. The uniformly dispersed nanopores throughout the structure of the mesocrystals can facilitate their contact with the electrolyte, hence increasing the electrode/electrolyte interface which favors fast Li^+ transport.

Other, more novel mesocrystal architectures for TiO_2 have also been synthesized. For instance, Hong et al. synthesized dumbbell-shaped rutile and quasi-octahedral anatase TiO_2 mesocrystals using a hydrothermal approach.[196] The dumbbell-shaped rutile TiO_2 mesocrystals were constructed from ultrathin nanowires oriented along the [001] crystallographic axis, and quasi-octahedral anatase TiO_2 mesocrystals built from tiny nanoparticles that had a fine microporous structure and large surface area. The galvanostatic charge–discharge performance as a function of current density for both the rutile and anatase mesocrystals were compared to nanoparticles of their corresponding material, and both mesocrystal specimens demonstrated their superiority. At a discharge rate of 5 C, the rutile mesocrystals had a discharge capacity of 103 mA h g^{-1}, while the rutile nanoparticles only exhibited 28 mA h g^{-1}. Similarly, the anatase mesocrystals exhibited a discharge capacity of 124 mA h g^{-1}, while the anatase nanoparticles only exhibited 32 mA h g^{-1} at a discharge rate of 5 C. The improved Li^+ intercalation rate performance was attributed to the intrinsic characteristics of the mesoscopic TiO_2 superstructures, which had a single crystal-like and porous nature which facilitated fast electron transport and relieved the strain from volumetric change.

3.3.2.3 Lithium iron phosphate. Bilecka et al. synthesized $LiFePO_4$ (LFP) mesocrystals *via* an extremely efficient microwave-assisted route.[197] Fig. 31 portrays the as obtained product which was composed of slightly elongated nanoparticles ($\sim$100 nm) nearly fused together into discs approximately 1 μm in diameter. The LFP mesocrystals were tested as cathode
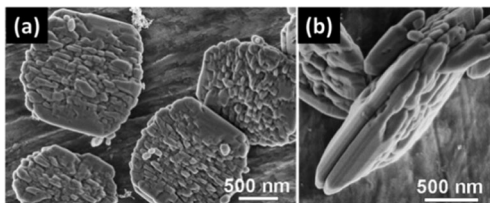
Fig. 31 SEM images of $LiFePO_4$, (a) top-view and (b) side-view, mesocrystals synthesized using a microwave-directed non-aqueous liquid phase synthesis approach under ambient conditions within several minutes.[197] Reproduced from ref. 197 with permission from The Royal Society of Chemistry.
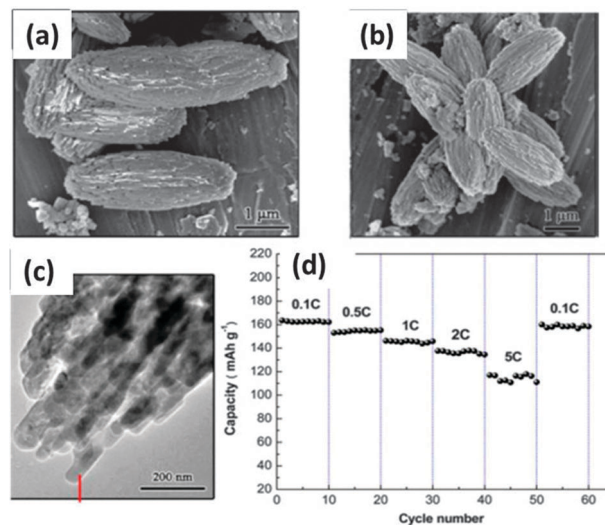
Fig. 32 Spindle-like LFP structure synthesized *via* a hydrothermal method obtained with a growth period of (a) 20 h, (b) pH of 10, and (c) the HRTEM image. (d) The charge–discharge profiles of the spindle-like LFP architecture in the voltage range from 2.5 to 4.2 V at various current rates.[198] Reproduced from ref. 198 with permission from Elsevier.

material for Li-ion batteries, and exhibited an initially moderate capacity of 150 mA h g^{-1} that was extremely stable upon cycling. The LFP mesocrystals also show modest rate capability (81%) up to a discharge rate of 8 C. However, the study did not clarify the relationship between the unique structural features and the performance of the LFP mesocrystals, and only suggested that the implementation of mesocrystals as electrode material may be the linking factor.[197]

In an attempt to compensate for the low electronic conductivity of LFP, carbon coated LFP mesocrystals were later studied by Xia et al., where they were synthesized using a solvothermal and post-growth annealing route.[198] The annealing route was required in order to convert the L-ascorbic acid into the carbon that coated the surface of the primary nanoparticles. Spindle-like structures approximately 2 μm in length and 1 μm in width, composed of nanoparticles approximately 100 nm in length and 50 nm in width, were observed with SEM and are depicted in Fig. 32. TEM analysis revealed the mesocrystalline nature of the obtained product; it was later determined that the product formed through standard non-classical crystallization techniques using a nanoparticle surface modifier as determined from time interval growth studies.

The spindle-like LFP mesocrystals demonstrated an incredibly stable cycling stability of approximately 165 mA h g^{-1} over the course of 50 cycles, and a moderate rate capability that terminated at 120 mA h g^{-1} at a rate of 5 C (Fig. 32d). The electrochemical performance was attributed to the porous structure that shortened the Li^+ diffusion length, enhanced electrolyte penetration, and increased the electrochemical reaction surface, thus alleviating electrode polarization. The incorporation of the uniform carbon coating throughout the structure also aided the electrochemical capability by enhancing the electronic conductivity.

3.4 Surface chemistry and defects in nanostructures relevant to lithium ion battery applications

As material structure was the main focus of study when the use of intercalation compounds as Li-ion battery electrodes was initially reported, current research efforts have begun to focus on surface modification.[199] Surface chemistry can be controlled through the presence of surface coatings, modifiers, or the introduction of defects. It is possible to manipulate the formation and characteristics of the SEI by altering the surface chemistry of the electrode in contact with the electrolyte, which can directly dictate redox processes and the electrochemical performance of the material. A desirable surface structure leads to a uniform and compact SEI film that may enhance the efficiency and cycling performance of Li-ion batteries.

3.4.1 Surface modification. Park *et al.* were able to enhance the electrochemical properties of $Li_4Ti_5O_{12}$ by modifying the surface structure and chemistry using a thermal nitridation process.[200] $Li_4Ti_5O_{12}$ was annealed in an NH_3 atmosphere to form a surface coating layer of TiN with metallic conductivity that could increase the overall conductivity of the electrode. The NH_3 surface modified $Li_4Ti_5O_{12}$ specimen demonstrated better capacity retention upon cycling compared to the pristine $Li_4Ti_5O_{12}$ specimen due to surface defects, which serve as a buffer against surface decomposition. Surface modified $Li_4Ti_5O_{12}$ also showed a greater capacity than the pristine sample at higher current rate, an enhancement factor of 6 at 10 C. The ammonia gas decomposed the surface of the $Li_4Ti_5O_{12}$ to form the conductive $TiN–Li_2CO_3$ core–shell morphology on the surface without altering the bulk lattice parameters.

Abel *et al.* recently demonstrated that introducing a small amount of bulk and surface oxygen (>20 at%), introduced during synthesis and post-synthesis low temperature annealing, into nanostructured silicon thin films can increase the cycling stability and rate performance, as demonstrated in Fig. 33.[201] Virtually no capacity loss was observed up to 150 cycles when both bulk and surface oxides were present in an annealed film, and only a slight capacity fade was seen between 150–300 cycles. The capacity measured at the 1 C rate was 1450 mA h g^{-1}, signifying that the specific capacity was somewhat sacrificed in order to enhance the cycling stability. An investigation on silicon nanowires with hydride, methylated, and siloxane terminated surfaces was also conducted by Xu *et al.*[202] The gathered results revealed that the methyl terminated nanowires were relatively unreactive and tended to passivate the silicon surface, while nanowires terminated with hydride formed SEI layers composed of carbonates, lithium salts, P–F species, and fluorocarbon compounds that enhanced the electrochemical properties. The specific capacity values of the hydrated Si nanowires were approximately 800–1300 mA h g^{-1} greater than the other treated nanowires, even after 15 cycles. These results advocate that surface terminations can be tuned and play a key role in the chemical and mechanical behaviors that dictate the electrochemical properties.

Coating the surface of the electrode material is a common technique used for tailoring the functionality or performance of the electro-active material. Carbon coating is one of the most popular means of easily enhancing the electronic conductivity of electrode materials, and can also stabilize SEI films.[134] For transition metal cathode materials such as $LiCoO_2$, $LiNiO_2$, and $LiMnO_4$, surface coatings with oxides such as MgO or Al_2O_3 can essentially shield the cathode material from direct exposure to the electrolyte solution, improving the structural integrity of the cathode material and suppressing phase transitions.[203] Another application of oxide coatings is for the removal of hydrogen fluoride (HF) from the electrolyte solution. HF is a by-product resulting from the decomposition of $LiPF_6$ in the presence of moisture. The presence of HF in the electrolyte solution is detrimental to the electrochemical performance of electrode materials because it can dissolve the transition metals and is responsible for surface corrosion of the cathode materials. Oxide coatings such as ZnO or Al_2O_3 can serve as HF scavengers and neutralize or reduce the active concentration of HF in the electrolyte solution by reducing the local acidity of the electrolyte near the material surface.[204]

3.4.2 Role of defects. Surface defects present at the electrode–electrolyte interface are expected to serve as nucleation sites that promote phase transitions between the redox and charge/mass transfer processes. As nucleation sites, surface defects may lead to the propagation of the transitioning phases into the bulk of the electrode upon cycling or potentially enhance the charge transfer. Surface defects have been documented as having the ability to dominate the electrochemical properties.[205]

Electrode materials displaying surface defects have commonly been synthesized by annealing the pristine materials with reactive gas or through substitutional doping techniques. The difficulty introduced with such techniques is to maintain the desired local chemistry while controlling the physical features at the same time. Suitable manipulation of the surface chemistry and introduced defects may also serve as a buffer zone to protect the electrode material from the electrolyte when submitted to prolonged cycling, or in such cases where the charging process is discontinuous (*i.e.*, frequency regulation); however, the principle aims of employing surface defects are to enhance the Li$^+$ storage capacity and improve the overall electrode kinetics.
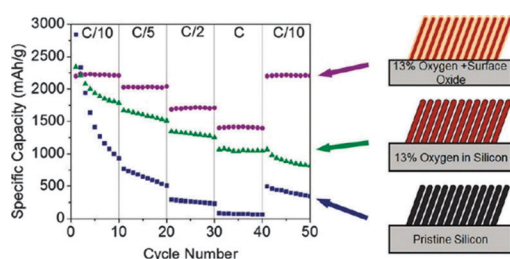
Fig. 33 The cycling rate performance of pristine silicon and partially oxidized silicon thin films with nanocolumnar morphology synthesized by evaporative deposition at a glancing angle. The incorporated oxygen concentration was controlled by varying the partial pressure of water during the deposition and monitored to vary the amount of bulk and surface oxygen.[201] Reprinted with permission from Abel *et al.*, *ACS Nano*, 2012, **6**(3), 2506–2516. Copyright 2012 American Chemical Society.

3154 | *Chem. Soc. Rev.*, 2013, **42**, 3127–3171

This journal is © The Royal Society of Chemistry 2013

Liu *et al.* recently investigated the effects of surface defects on the electrochemical performance by annealing V_2O_5 aerogels in different reactive environments (N_2 and air).[206,207] The N_2 annealed films adopted a less crystalline structure composed of particles with smaller grain size. The N_2 annealed films also had a narrower bandgap than the air annealed films, and the color indicated that the vanadium valence state was a mix of V^{3+} and V^{4+}. Both of these effects could be attributed to the existence of defects in lower valence states. Electrochemical impedance spectroscopy confirmed an improved electrical conductivity in the N_2 annealed V_2O_5 films with defects such as V^{4+}, V^{3+}, and oxygen vacancies. The N_2 annealed films also showed considerably enhanced capacity and cycle stability when compared to the air annealed films. The discrepancy between the two films was also attributed to the presence of surface defects which can act as nucleation centers in the phase transition during Li^+ (de)intercalation. The same general trend was observed for TiO_2 nanotube arrays annealed in CO and N_2; the improved intercalation capacity and rate capability of the CO annealed arrays was attributed to the presence of surface defects and cation groups with oxygen vacancies, which not only improved the charge-transfer conductivity of the arrays but also promoted the phase transition.[208] Another group also confirmed this finding by comparing the Li^+ capacity of pristine and O_2/H_2O treated V_2O_5, and attributed the difference in the electrochemistry of the two materials to the nonstoichiometric and surface point defects, which serve as additional charge storage sites.[209]

Sun *et al.* also explored the role of defects on electrochemical performance by synthesizing highly ordered and defect-rich vanadium oxide nanorolls, further corroborating the importance of defects in improving the electrode material performance.[210] The VO nanorolls with defects exhibited superior capacity and cycle stability compared to the pristine VO nanorolls, results that were related to the V^{4+}/V^{5+} ratio, detectable cracks in the wall surfaces, and residual organic surfactant. The electrochemical enhancement was attributed to the additional redox sites resulting from the atomic-scale disorder and the enhanced accessibility of Li^+ to the nanorolls because of cracks in between the layers and present due to defects. The results suggest that perfectly ordered materials may not be the ideal structure for electrochemical applications due to the limited ion diffusion rate.[210]

In studies less focused on defect formation and characterization, Guo *et al.* synthesized carbon–carbon nanotube composites *via* a soft-templated self-assembly process.[211] The porous and defect-rich structure was initially frozen into the sample by carbonization, but both effects were lost due to solid state amorphization upon cycling. This loss was accompanied by a steep drop in the capacity after the initial cycle and noticeable capacity fading upon cycling. Reddy *et al.* demonstrated that the Li^+ capacity and cycle stability were greater in nitrogen-doped graphene than in un-doped graphene, and ascribed the discrepancy to the introduction of surface defects into the system.[212] Disordered graphene nanosheets have also been shown to enrich Li^+ capacity due to additional reversible storage sites such as edges and other defects.[213]

More recently, it has been demonstrated that anion surface modification of $LiFePO_4$ particles can reduce the electrode–electrolyte charge transfer resistance, thereby preventing irreversible capacity at higher rates.[214] This anion surface modification was accomplished by substituting nitrogen or sulfur for surface oxygen on the (010) surface plane of $LiFePO_4$ nanoplates. DFT calculations show that the barrier for Li-ion transfer is decreased by strong Li^+ binding on surface sites when nitrogen or sulfur is substituted for surface oxygen. Calculations have indicated the activation energy for Li^+ surface diffusion along the surface (010) plane is quite high. Because of the strong covalent nature of the $(PO_4)^{3-}$ anion, it is reasonable to assume that the Li or Fe sites become under-coordinated at the surface and that they can be easily replaced with substitutional anions. Nitrogen and sulfur are of considerable interest towards replacing surface oxygen or $(PO_4)^{3-}$ anions because of their discrepancy in ionic size, formal charge, and electronegativity. Nitrogen can stabilize Li^+ in both the a- and b-sites because it affects the binding energies both electronically and ionically (more stable 2p state and more negative charge); whereas sulfur binds directly to a surface Fe atom, providing full coordination of the Fe center. Sulfur substitution increases the binding of Li^+ in the b- and c- subsurface sites with respect to the surface a-site. Ultimately, surface modification can be exploited to engineer the surface energy levels and adjust the charge transfer kinetics. As expected, both N- and S-substitution exhibited considerably enhanced electrode performance compared to bare $LiFePO_4$ particles of the same size.

3.5 Limitations of nanostructured electrode materials for Li-ion batteries

Given all the benefits of nanostructuring, the synthesis and characterization of nanostructured electrode materials of various chemistries have been extensively investigated. However, the use of nanostructures is not a panacea, and there are several performance issues, either lingering or deriving from nanostructuring, that still need to be addressed. One of the more noticeable effects incurred from nanoscaling is the increased relevancy of the surface chemistry and energy. For nanoscale materials, the surface free energy involves an extra contribution that need be taken into consideration for the chemical potential, and can be approximated by:

$$\mu^o(r) = \mu^o(r = \infty) + 2\left(\frac{\gamma}{r}\right)V \qquad (10)$$

where γ is the surface tension, r the particle radius, and V the partial molar volume. The capability of nano-insertion materials to surpass the theoretical capacity limits of their bulk counterparts has already been discussed; the larger storage capacity has been attributed to the large and energetically relevant surface area of the nanoparticles that contributes to the high electro-activity toward Li^+ storage. However, the excess free surface energy can also result in several disadvantages. Too high a Li-ion surface insertion leads to passivation of the surface region by surface reconstruction or mechanical failure, and accompanying irreversible capacity loss is inevitable.

Thus, there exists an optimal particle range for nanomaterials where cracks resulting from non-surface related volume expansion will not propagate, and surface reconstruction will not occur.

Morphology also plays a pivotal role in the electrochemical performance; the observation of curved voltage profiles with diminished voltage plateaus has been attributed to the strain and interfacial energy from coexisting lattice terminations within electrode nanoparticles. However, it has been revealed to be the consequence of different structural environments in the near-surface region that result in a distribution of redox potentials. These varying structural environments depend on the distance from the surface and the surface orientation itself, verifying that morphology plays an important role in the particle stability.[215] Hence, the irreversible capacity will be larger for smaller particles with a large surface area greater than some critical value, where the optimal particle size is dictated by the voltage window.[141]

Electronic conductivity and ionic diffusivity have long been limiting factors to the development of electrode materials for Li-ion batteries. These barriers stem from several fundamental issues: (1) the metal oxide materials typically employed as cathodes have relatively low electronic conductivity values, (2) an unclear relationship between the electrical and ionic conductivities in electrodes, and (3) phase transformations upon lithiation that can change the conductive properties. Additionally, it has been well established that nanomaterials suffer from resistivity values much greater than their corresponding bulk material; nanowires, for example, typically display resistivity values that are $\sim$20% greater than what is seen in the bulk regime, and can extend up to several orders of magnitude.[216] The reason for the drastic increase in the resistivity of nanomaterials is the sheer increase in the relative surface area and the number of grain boundaries that is strongly dependent on the particle size and morphology. These physical parameters negatively impact the conduction mechanisms because of the inelastic scattering of conduction electrons at particle surfaces and the reflection of electrons at grain boundaries. These effects are also more pronounced in the electrode materials with smaller mean particle size. To compensate for these effects, conductive additives, such as carbon, are typically added to electrodes, but such inclusions decrease the already low packing density of nanostructured electrode materials even further.

The high surface area and corresponding high surface energy of nanoparticles also increases the potential for secondary or side reactions at the particle surface. The main reaction at risk exists between the electrode and electrolyte, and involves electrolyte decomposition which would lead to a considerable degree of irreversibility and capacity fade upon cycling. The SEI layer is a film that typically forms on the anode through the decomposition of the electrolyte into lithium containing organics and inorganics that deposit onto the electrode–electrolyte interface in an attempt to reduce the contact area and thereby prevent further electrolyte decomposition.[217] It should be noted that SEI films formed on graphitic anodes acting as an interfacial stabilizer have also contributed towards

improving the capacity retention of the anode over long cycle lifetimes at the expense of a large irreversible capacity drop associated with film formation.[218] In this regard, the formation of a stable SEI layer can be desired, but thicker and unstable SEI films can negatively impact electrode performance. Regardless, SEI film formation is often unstable, and its ionic and electronic conductivities are relatively low and it effectively intercepts and stores Li$^+$ that would otherwise be intercalated by the electrode. These mechanisms tremendously decrease the electrochemical performance of the cell by limiting the intercalation capacity and supporting capacity degradation, respectively. Heat generation often accompanies SEI film formation, thereby causing thermal shifting away from the previously established stable conditions.[219] Thus, the formation of an SEI layer could potentially be the cause of thermal instability, which in turn could result in an irreversible loss in the capacity by hindering the intercalation kinetics.[220,221] One of the more important factors that dictates SEI layer formation is the morphology and overall size of the electrode material particles.[222] SEI layer formation is therefore more prevalent and evident on nanostructured electrodes, compared to the bulk, because of their inherently large surface area and corresponding energy at the electrode–electrolyte interface. This often results in thicker and denser SEI layers that produce more heat during formation, factors all of which negatively impact electrochemical performance.[223] Past studies have clearly demonstrated the deleterious effects of SEI layer formation on nanostructured electrodes. It was confirmed that a thicker SEI layer would form on LiCoO$_2$ as the particle size decreased.[224] The thicker layers negated the positive effects of nanostructuring the electrode material by severely impeding Li-ion diffusion, and diminishing the electrode performance at higher current densities. Similar results were seen for LiMn$_2$O$_4$ where the SEI layer thickness on a cycled electrode increased in a near linear fashion with the number of cycles, and the cycle stability was the performance parameter most impacted.[225] However, thick SEI films formed on nanostructured transition metal oxides during Li$^+$ intercalation have been shown to disappear completely during deintercalation due to a catalysis reaction involving the transition metal, leading to a continuously reiterative capacity fade upon repetitive cycling.[130]

Processing conditions are also heavily impacted by the high reactivity of nanoparticles. Many nanomaterials exhibit poor stability when exposed to ambient atmosphere; such is the case for olivine LiFePO$_4$ due to the reactivity of Fe^{2+} in the presence of atmospheric oxygen and water. This undesired reaction under ambient exposure is known to be more pronounced for smaller particles because of their increased surface/exposure area, and can result in spontaneous lithium extraction and surface oxidation.[226] It has also been revealed that nanostructured electrode materials with poor adherence to the current collector will agglomerate during cycling; nano-SnSb undergoes successive agglomeration during Li$^+$ insertion and extraction, and experiences quick capacity fade as a result.[227] Thus, the application of some electro-active materials may be limited due to the high processing costs associated with avoiding these secondary reactions and stability issues.

3156 | Chem. Soc. Rev., 2013, 42, 3127–3171

This journal is © The Royal Society of Chemistry 2013

Another size-stability issue with transition metal oxide nanoparticles is their propensity of the electro-active metal ion to dissolve in the electrolyte, further resulting in capacity degradation. Electro-active metal ion dissolution has been well documented for $LiMn_2O_4$, where Mn-ions in the electrode easily dissolved into the electrolyte as induced by acids generated *via* oxidation of the solvent molecules.[228,229] To date, this issue has been resolved by coating the nanoparticles with oxides and non-oxide systems to decrease the surface area and terminate the side reactions.[230] Despite the implementation of such strides to eliminate these performance issues, the cyclic stability remains a serious problem for nanostructured $LiMn_2O_4$, and related manganese oxide electrodes. The stabilized electrochemical operating voltage range for nano-structured electrode materials also becomes narrower, compared with bulk materials, for similar reasons.

3.6 Remarks

This contribution highlights a wide range of recent advances in the synthesis and implementation of functional nanomaterials used as electrodes for Li-ion battery applications. Several general strategies towards the synthesis of advanced energy storage materials have been emphasized, such as the use of nanomaterials, micro/nano-structured architectures, hollow architectures, mesocrystals, and the manipulation of surface chemistry. The nanostructuring of electrode materials for Li-ion batteries results in enhanced Li^+ kinetics and the alleviation of localized strain, which leads to an improved rate capability and cycling performance. However, the Coulombic efficiency of nanostructured electrodes is decreased due to the large surface area of the nanomaterials. The design of micro/nano-heterostructures overcomes these issues by exploiting the nanostructure traits in a microstructured assembly. Such architectures exhibit enhanced thermodynamic stability and the elimination of undesired side reactions and nano-toxicity effects while being inexpensive to produce. Hollow nanostructured electrodes also demonstrate enhanced rate capability and cycling stability, but suffer from reduced volumetric energy density because of the presence of the inner cavity. It may be possible to compensate for this trade-off by optimizing the shell thickness and void size. Mesocrystals, on the other hand, exhibit near single crystalline behavior and can be classified by their high degree of crystallinity, high porosity, and subunit alignment along a crystallographic register – all of which have been proven to increase electrochemical performance. Recent advances have also demonstrated that thermodynamic non-equilibrium effects can be exploited towards optimizing electrode performance. The presence of surface defects has also demonstrated the ability to modify the surface thermodynamics and facilitate the phase transition boundaries. Surface chemistry modifications and surface defects may enhance the storage capacity by shifting the phase transition boundary and introducing a fast mass and charge transport path. Further development and optimization of these materials can still be achieved through the synergy of these techniques. These energy storage materials with high capacity, long cycling life, and a high degree of safety will certainly improve the performance of energy storage devices and facilitate their wide application.

4. Nanostructured materials for supercapacitor applications

4.1 Introduction

Supercapacitors, also referred to as electrochemical capacitors or ultracapacitors, are energy storage devices that have high power density, long cyclic stability, and can be charged and discharged rapidly. They have storage capacities that are several orders of magnitude higher than that of conventional dielectric capacitors. They are also environmentally friendly, safe, and can operate in a wide range of temperatures. Supercapacitors can be used alone or in combination with batteries or fuel cells. Applications include back-up power supplies, industrial equipment, and hybrid/electric vehicles, where supercapacitors can provide high power during acceleration and recover energy during braking.[231–233] Many excellent reviews detailing the fundamental considerations of supercapacitors can be found in the literature.[234–238]

In general, there are two classes of supercapacitor, each defined by the charge storage mechanism. The first is electrical double layer capacitors (EDLC), which operate by adsorbing–desorbing charged ions from an electrolyte onto high surface area electrodes forming a double layer structure. The other type of electrochemical capacitor, known as pseudocapacitors or redox supercapacitors, uses transition metal oxides or electrical conducting polymers as electrode materials, with the charge storage depending on fast *Faradaic* redox reactions. Compared with other electrical energy storage devices, electrochemical capacitors can be fully charged or discharged in seconds. Although their energy density (~ 5 W h kg^{-1}) is lower than that of batteries, they have high power density (10 kW kg^{-1}), which is about 10 times larger than in secondary batteries.[235,239]

For EDLCs, the capacitance (C) is related to the surface area, the effective dielectric constant (ε) and the double layer thickness (d) by an inverse linear relationship ($C = \varepsilon A/d$). The combination of high surface area and small charge separation is necessary for high capacitance. A typical smooth surface will have a double layer capacitance of about 10–20 μF cm^{-2}, but if a high surface area electrode is used, the capacitance can be increased to 100 F g^{-1} for conducting materials with a specific surface area of 1000 m^2 g^{-1}.[240] In traditional dielectric capacitors, the capacitance is limited by the thickness of the dielectric material, which separates the charge. The thinnest dielectric materials are 2–5 μm thick.[241] However, in the case of EDLCs, charging is achieved by dissociation of ions in the electrolyte salts, resulting in charge separation distances on the order of 1 nm. Carbon materials are used the most often because of their low electrical resistance, easy processability, chemical inertness, stability, and low cost. Typical materials include activated carbon, carbon aerogels, carbide-derived carbon/ordered mesoporous carbon, carbon nanotubes, and graphene.

For pseudocapacitors, the capacitance involves voltage dependent reversible *Faradaic* reactions between the electrode

and the electrolyte, either in the form of surface adsorption–desorption of ions, redox reactions with the electrolyte, or doping–undoping of the electrode materials. Common materials for pseudocapacitors include conducting polymers and metal oxides or nitrides. Redox reactions occur in the electro-active material because of several oxidation states. Often, reactions do not propagate into the bulk material, and occur only at the electrode–electrolyte interface.[237] Typical pseudocapacitive materials include conducting polymers, such as polypyrrole, polythiophene, and polyaniline, and metal oxides, such as RuO_2, MnO_2, Co_3O_4, *etc.* A large amount of current research focuses on the development of nanostructured materials for use as supercapacitor electrodes. Nanostructures provide a high surface area, making more active material available to the electrolyte for double-layer formation and/or pseudocapacitive reactions.[242,243] In addition, tuning the morphology leads to easier access of the electrolyte ions and reduced diffusion distances.[232] This allows for higher current density and faster response time.[244,245] As a result, higher capacitance and better charging–discharging performance can be obtained for these materials than with bulk materials.[244]

However, it is important to keep in mind the challenges that arise by using nanostructured materials. While significant research effort has been made to achieve a higher capacitance by maximizing the surface area, the correlation between surface area and capacitance cannot be strictly established. Above 1500 m^2 g^{-1}, capacitance no longer increases linearly with surface area. One explanation for this is that the increased pore volume at very high surface areas results in pore walls that are too thin. As the thickness of the pore walls decreases, it approaches the screening length of the electric field created by the electric double layer. If the walls are too thin, the electric field and charge density will not decay to zero within the pore walls. Therefore, a thinner pore wall cannot accommodate the same amount of charge as a thicker pore wall can at a given potential. Further increases in surface area will be accompanied by a decrease in capacitance.[247] Another reason for the leveling off of capacitance is that the number of small micropores (~1 nm) increases for high surface area samples. Micropores of this size could be too small to allow electrolyte ions to diffuse inside, resulting in inaccessible surface area that is not available for charge storage. Therefore, surface area measurements can overestimate the actual surface area available for ion adsorption.[247,248]

The traditional understanding is that pores need to be larger than the size of the electrolyte ion and its solvation shell to maximize the specific capacitance. As the pore size decreases to a critical value nearing 1 nm, the specific capacitance will likewise decrease. However, recent research has shown that below this critical value, there is a sudden sharp increase in the capacitance with decreasing pore size. Fig. 34 illustrates this trend. In region I, the largest contribution is from mesopores that are substantially larger than twice the size of solvated ions. The larger pore size means greater accessibility of the electrolyte ions into the pores and less overlapping of the double layer structure as seen in Fig. 34b. Double layer formation on both adjacent pore walls will contribute to the
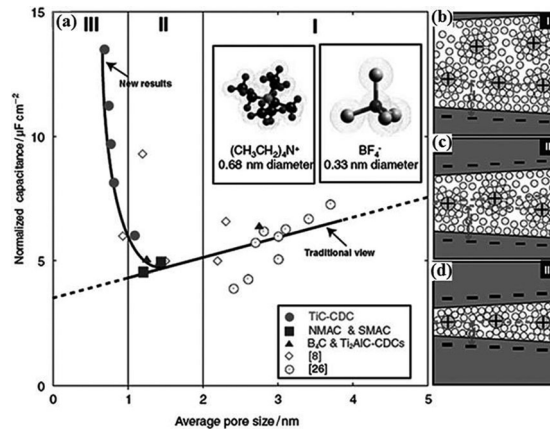
Fig. 34 (a) Effect of average pore size on capacitance normalized to specific surface area. (b) Double layer formation in pores more than twice the size of solvated electrolyte ions. (c) Ionic layer overlap in pores less than twice the size of solvated electrolyte ions. (d) Distortion of solvation shells in small micropores.[246] Reprinted from J. Chmiola *et al.*, *Science*, 2006, **313**, 1760–1763, with permission from AAAS.

capacitance. In region II, where the pore size decreases to less than twice the diameter of the solvated electrolyte ions, the capacitance decreases due to overlap of ion layers on adjacent pore walls and a decrease in usable surface area as shown in Fig. 34c. Finally, in region III, the capacitance increases sharply with decreasing pore sizes due to the distortion of the solvation shells surrounding the electrolyte ions. As seen in Fig. 34d, this allows the ion center to more closely approach the electrode surface and decreasing the charge separation d as seen in Fig. 34d.[246,249] However, micropores have been shown to have a pronounced effect on the power density, leading to decreased capacitance at increased discharge rates.[237] In larger pores, electrolyte ions are less likely to crash into pore walls, reducing the ion transport resistance. In general, smaller pore sizes correlate with higher energy density while larger pore sizes correlate with higher power density.[238] This correlation demonstrates the importance of tailoring the nanostructure to fit the specific requirements of an application. The remainder of this section will highlight some recent advances in controlling novel nanostructures for improved properties in supercapacitors.

## 4.2 Nanomaterials for supercapacitors

4.2.1 High surface area porous carbon. Activated carbons have long been the most widely used material for EDLCs because they have high surface area, low cost, and are easily processed.[250] Current EDLCs on the market are produced by pyrolyzing and activating wood, plant matter, petroleum sources, and phenolic resins (including aerogels and cryogels), among others.[251,252] Naturally derived electrodes contain great amounts of impurities or ash content, which can compromise the EDLC performance[253] due to degradation of the electrolyte. In addition, the pore size is limited by what nature provides and may vary from source to source. Synthetic carbons, on the other hand, have good conductivity, high surface area, controlled bulk and surface chemistry, and tunable porous

structure, rendering them excellent candidates as electrodes for supercapacitors with high energy density and long cyclic stability.[254–257] A higher capacitance can be achieved by careful thermal, chemical, or electrochemical treatment to increase the accessible surface area and surface functional groups, or by extending the operating voltage range beyond the limit of an aqueous electrolyte solution.

Templated carbon is synthesized through carbonization of an organic precursor impregnated in an inorganic template followed by removal of the template. Common template materials include clay, where the carbon precursor is infiltrated between the lamellae, and mesoporous molecular sieves, which are often made from mesoporous silica. Yet another material is zeolites, which possess long-range order, three-dimensional channels, and an open microporous structure.[258] Since the pores of the resulting carbons are uniform and ordered, all of the pores are expected to be accessible to the electrolyte. Additionally, the precise control of the pore size can create carbons with microporosity and only a very small amount of mesoporosity, leading to surface areas that can reach over 4000 m^2 g^{-1}.[259] Fuertes et al. obtained porous carbon from the carbon precursor furfuryl alcohol using SBA-16 silica as a template.[260] The resulting carbon has a morphology that replicates that of the silica template and unimodal pore size distribution. When used in supercapacitors, the template carbon exhibited excellent performance at high charge–discharge rate due to tailored pore size that allows easy diffusion of the electrolyte ions. Xu et al. prepared hierarchical porous carbon from a zeolite template.[261] Pore structures were controlled by varying the time during chemical vapor deposition of the carbon precursor. Pretreatment of the zeolite with NaOH before precursor deposition also resulted in a different pore structure of the final template carbon. Samples with the highest surface area accessibility resulted in the best electrochemical performance, reaching 215 F g^{-1} in 6 M KOH aqueous electrolyte. A new family of synthetic mesoporous carbon called carbide-derived carbon (CDC) has been developed recently through selective removal of non-carbon atoms from carbides upon high-temperature treatment (i.e., chlorination).[262,263] The porous structure, including average pore size, pore size distribution, pore volume, and specific surface area of CDC can be tailored through selection of the precursor (i.e., the composition and structure of carbides) and the chlorination conditions. CDC with a specific surface area > 3100 m^2 g^{-1} and pores of ∼0.3–10 nm makes a promising material for supercapacitor electrodes.[246,264–266]

Presser et al. reported nano-fibrous felts (nanofelts) of CDC developed from electrospun titanium carbide (TiC) nanofelts as the precursor.[267] Conformal transformation of TiC into CDC conserves the main features of the precursor, including the high interconnectivity and structural integrity; the developed TiC–CDC nanofelts are mechanically flexible and resilient, and can be used as an electrode material for supercapacitor applications without the addition of a binder. After synthesis through chlorination of the precursor at 600 °C, the TiC–CDC nanofelts show an average pore size of ∼1 nm and a high
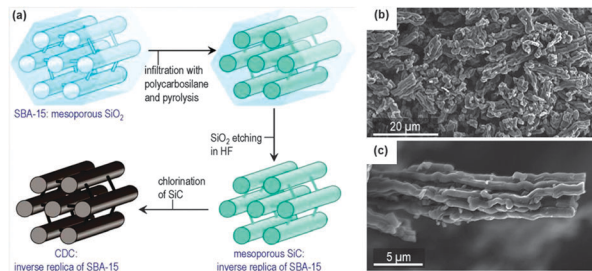
Fig. 35 (a) Schematic illustration of the fabrication of SiC–CDC. (b) and (c) SEM images of the particle morphology.[232] Reprinted with permission from Korenblit et al., ACS Nano, 2010, **4**(3), 1337–1344. Copyright 2010 American Chemical Society.

specific surface area of 1390 m^2 g^{-1}, and the nanofibers have graphitic carbon ribbons embedded in a highly disordered carbon matrix. Electrochemical measurements show a high gravimetric capacitance of 110 F g^{-1} in aqueous electrolyte and 65 F g^{-1} in organic electrolyte. Korenblit et al. were able to prepare CDC from SiC.[232] An ordered mesoporous SiO$_2$ template was infiltrated with the precursor polycarbosilane and the template was then etched away, leaving mesoporous SiC. The technique produced porous CDC nanorods with aligned mesopores between the particles, as shown in Fig. 35. Pore sizes were less than 4 nm and the BET specific surface area was 2250–2430 m^2 g^{-1}, which is higher than previous studies of SiC–CDC. This resulted in a specific capacitance of 170 F g^{-1} in TEATFB/AN (tetraethylammonium tetrafluoroborate in acetonitrile). The ordered mesopores allow for fast ion conductivity into the bulk CDC particles, leading to fast frequency response and capacitance retention at high current densities.

4.2.2 Carbon nanotubes (CNTs) and graphene. Carbon nanotubes and graphene have also been used in the manufacturing of supercapacitors because of their high conductivity.[252,268] They are highly conductive and have an accessible pore network of mesopores, allowing for fast ion transport for EDLCs. However, the lack of micropores leads to only a moderate surface area of 100–400 m^2 g^{-1}. However, it has been found that a higher capacitance can be achieved with more defected outer CNT walls and the presence of a thin layer of amorphous carbon on the outer walls results in better charge accumulation.[269] Additionally, increasing the surface area through activation processes can also increase the capacitance. An et al. obtained a maximum specific capacitance of 180 F g^{-1} with a large power density of 20 kW kg^{-1} by heating CNTs to enhance their specific surface area and pore distribution.[270] However, the specific surface area of CNTs still remains low compared to other activated carbon electrodes (specific surface area up to 3000 m^2 g^{-1}) or mesoporous carbons (up to 1730 m^2 g^{-1}).[271,272] Researchers have also treated the surfaces of CNTs with ammonia, aqueous NaOH–KOH solution, or nitric acid to introduce oxygen functional groups (carboxyl, phenolic, lactone, aldehyde, ether groups, etc.), and thus improve the electrochemical properties of the electrodes.[273–275] For example, Niu et al. treated MWNTs with nitric acid, showing a specific capacitance of 113 F g^{-1} using a solution of 38 wt% H$_2$SO$_4$ as the electrolyte.[276]

Yoon et al. increased the capacitance of the CNT electrode from 38.7 to 207.3 F g^{-1} through surface treatment using ammonia plasma.[273] However, the oxygen groups can lead to capacitor instability with an increased resistance and deterioration of capacitance.[277,278] In addition, the introduction of surface oxygen groups to the CNT electrode would be detrimental in an organic electrolyte.

The specific power of supercapacitors is $P_{max} = V^2/4R$, where V is the working voltage and R is the equivalent series resistance. The resistance is comprised of the electronic resistance of the electrode material, the interfacial resistance between the electrode and the current-collector, the diffusion resistance of ions moving in small pores of the electrode material, or other resistances.[277,279] That is, the characteristics of the electrode materials and the type of fabricated electrode become the key factors for excellent performance, such as the density of CNT arrays.[280] To enhance supercapacitors energy storage properties of a CNT supercapacitor, CNTs can be directly deposited on the current collector (Ni, Al, alloy or other metals) as electrodes, reducing the contact resistance.[270,273,276,281–283] For example, Dörfler et al. used a scalable technique to grow vertically aligned carbon nanotubes between 5 to 20 nm in thickness directly on metal foil substrates, as shown in Fig. 36.[284] The resulting resistance was very low (53.6–232 mΩ cm^{-2}) with a capacitance approaching that of the theoretical value for single walled CNTs. Forming this binder-free CNT film electrode would enhance its electrochemical performance as it has fewer impurities introduced by the polymer binders. Some groups even designed lightweight electrodes using dense CNT networks as both the current collector and the active electrode material for ECs.[285]

The theoretical surface area of graphene is 2675 m^2 g^{-1}, leading to a possible specific capacitance of 550 F g^{-1}. However, this has yet to be achieved due to agglomeration of the graphene sheets, decreasing the accessible surface area and leading to capacitances a little over 100 F g^{-1}.[286–288] Wang et al. used a

gas–solid reduction process to avoid aggregation and achieved a maximum specific capacitance of 205 F g^{-1} at 1.0 V in aqueous electrolyte with an energy density of 28.5 W h kg^{-1}.[289] Liu et al. fabricated supercapacitors with curved graphene to prevent the sheets from restacking, obtaining a very high energy density (85.6 W h kg^{-1} at 1 A g^{-1} at room temperature or 136 W h kg^{-1} at 80 °C) using an ionic liquid electrolyte.[290] Several groups reported the effectiveness of using CNTs as a spacer in between the graphene sheets, preventing agglomeration and also acting as a conductive additive and binder.[291,292] The specific capacitance can reach 326 F g^{-1} with a graphene sheet to CNT weight ratio of 9 to 1.[292]

4.2.3 Porous conducting polymers. Conducting polymers are an attractive pseudocapacitive material because they have a high charge density and relatively low cost, and are easily manufactured, especially as thin films. These materials have the ability to be reversibly oxidized and reduced. The redox reactions in the bulk of the material allow for high energy storage and reduced self-discharge, but the power density often suffers due to slow diffusion.[293] Polyaniline is perhaps the most frequently researched conducting polymer because it exhibits multiple redox states,[242] but some other common polymers include polypyrrole and polythiophene and its derivatives. The capacitance is often highly dependent on the preparation conditions, including synthetic route and monomer structure.

Sharma et al. utilized a novel pulsed polymerization technique to prepare highly porous polypyrrole films.[294] A shorter pulse time formed films with 10 μm flakes with short polymer chain lengths and high degrees of conjugation. The capacitance obtained was 400 F g^{-1} with an energy density of 250 W h kg^{-1} and good cyclic stability attributed to reduced chain defects and a high degree of doping. Poly(3,4-ethylenedioxythiophene) nanotubes grown using an alumina template were shown to have a high power density due to the fast charge–discharge capability. The hollow structure allows easy transport of counter-ions into the polymer and the thin nanotube walls provide a short diffusion distance.[295] Similarly, Wang et al. recently synthesized aligned polyaniline nanowire arrays with a high specific surface area and ordered nanostructures. The electrochemical performance is shown in Fig. 37. The capacitance in aqueous solution was 950 F g^{-1}, which is higher than previous reports for polyaniline nanowire networks (742 F g^{-1}) and polyaniline nanowire arrays grown from a template method (700 F g^{-1}). A capacitance of 780 F g^{-1}
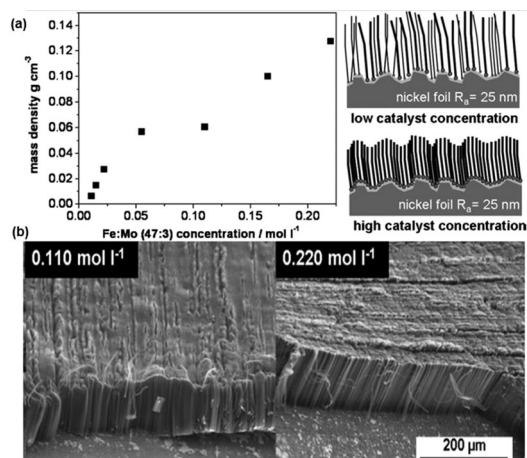
Fig. 36 (a) CNT mass density with increasing catalyst concentration and schematic showing how CNT growth is influenced by different catalyst concentrations. (b) SEM images of CNT films grown with different catalyst concentrations on Ni foil.[284] Reproduced from ref. 284 with permission from Elsevier.
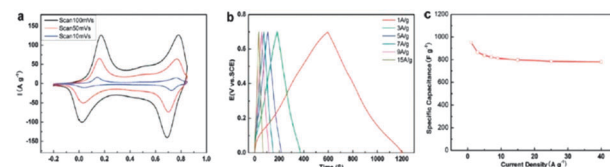
Fig. 37 Electrochemical capacitance behavior of PANI nanowire arrays in HClO$_4$ aqueous solution: (a) cyclic voltammetry at different scan rates, (b) typical galvanostatic charge–discharge curves at several current densities, and (c) specific capacitance in different current densities.[242] Reprinted with permission from Wang et al., J. Phys. Chem. C, 2010, **114**, 8062–8067. Copyright 2010 American Chemical Society.

was retained at high current density, as the narrow nanowire diameter helps the electrolyte ions penetrate into the polymer easily.[242]

4.2.4 Nanostructured metal oxides. The best example of redox pseudocapacitance is hydrous RuO_2, with a reported capacitance of 850 F g^{-1}.[296] The material shows high conductivity, continuous redox activity over a relatively wide voltage range, and high reversibility.[237] However, applications of RuO_2 are limited due to its high cost. Recent work focuses on replacing RuO_2 with more inexpensive transition metal oxides and nitrides, such as Mn, Fe, Co, Ni, V, Mo, In, *etc.*, and the development of nanostructures from these materials. For example, cobalt oxide is a promising alternative to RuO_2 because it has high redox activity and good reversibility at relatively low cost.[244,245] Gao *et al.* used a template-free growth method to prepare Co_3O_4 nanowire arrays on nickel foam.[243] The nanowires were 250 nm in diameter, 15 μm long, and were composed of layered nanoplatelets. A longer growth time allowed for higher nanowire loading. The binderless electrodes had a capacitance of 746 F g^{-1} in aqueous KOH electrolyte with a reduction in capacitance of less than 15% after 500 cycles. Tummala *et al.* used a plasma spray technique to make nano-structured porous and flexible Co_3O_4 electrodes.[245] The material was deposited directly on the stainless steel current collector, without the use of a binder or carbon additive. Deng *et al.* demonstrated that a capacitance as high as 2200 F g^{-1} can be achieved with nanostructured cobalt oxide, whereas the capacitance of bulk cobalt oxide is 209 F g^{-1}.[244] A thin layer of cobalt oxide is coated on a current collector film composed of nickel nanopetals shown in Fig. 38, resulting in a high surface area nanostructure that provides more active sites for pseudocapacitive reactions and minimizes ionic and electronic transport distances, thereby improving electrode kinetics.

However, one drawback is the decreased conductivity of alternative metal oxides when compared to RuO_2. To overcome this limitation, many groups have focused on nanocomposites. For example, composites of MnO_2 and CNT or conductive polymers can range from 210 F g^{-1} to 415 F g^{-1}. Lang *et al.* plated nanocrystalline MnO_2 onto nanoporous gold substrates to improve the conductivity, achieving a capacitance as high as 601 F g^{-1} at slow scan rates and 170 F g^{-1} at higher current density.[297] In a study by Kim *et al.*, $NiO–TiO_2$ nanotube arrays with large surface area, high packing density, and ordered pore

networks were constructed as electrodes.[231] The capacitance was estimated to be 100–300 F g^{-1} for the NiO component of the nanotube arrays. These electrodes also showed a higher rate capability than nanoparticle film electrodes owing to the ordered film architecture, which is expected to allow for fast electron and ion transport. Composites of intertwined V_2O_5 nanowires and CNTs can obtain a capacitance above 300 F g^{-1} in aqueous electrolyte and an energy density of 40 W h kg^{-1} at a power density 210 W kg^{-1} in organic electrolyte.[298] Fe_3O_4 is a promising electrode material because of its low cost and environmental impact, but it has low electronic conductivity. However, forming composites of Fe_3O_4 nanoparticles with reduced graphene oxide sheets shows a capacitance of 480 F g^{-1} with an energy density of 67 W h kg^{-1} at a power density of 5506 W kg^{-1}.[299] Combining metal oxides with carbon-based materials also creates the possibility of a large capacitance from combination of dual storage mechanisms from EDLC and pseudocapacitance.[300]

4.3 Remarks

In general, nanostructures provide higher surface area, easier access of electrolyte to the active material, and shorter diffusion distances, leading to improved energy storage and performance in supercapacitors. There are two types of supercapacitor, each based on their charge storage mechanisms: EDLCs physically separate charge at the active material/electrolyte interface to form a double layer structure, and pseudocapacitors rely on fast redox reactions between the electrolyte and the active material. Carbon materials, including activated carbon, carbon aerogels, carbide-derived carbon, CNTs, and graphene, are the most widely used for EDLCs because they are low cost, easily processed, chemically inert, stable, and have low electrical resistance. The capacitance is enhanced by increasing the surface area through activation processes, templating, or preventing agglomeration in the case of graphene. However, there is a limit to how much the surface area can be increased, as the pore structure must be carefully tuned to accommodate electrolyte ion diffusion. Typical pseudocapacitive materials are conducting polymers, such as polypyrrole, polythiophene, and polyaniline, and metal oxides, such as RuO_2, MnO_2, and Co_3O_4. While pseudocapacitive materials can achieve a much higher capacitance than EDLCs, they suffer from decreased cyclic stability. One emerging research direction is combining pseudocapacitive materials with carbon-based materials in order to utilize capacitance contributions from both double layer formation and pseudocapacitance.
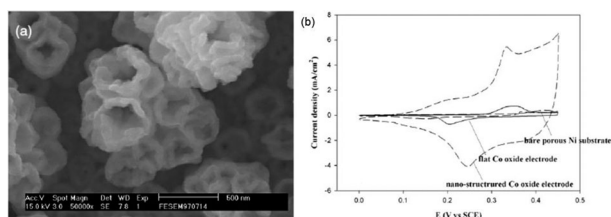
Fig. 38 (a) SEM micrograph of a thin layer of anodically deposited Co oxide on a nanostructured porous Ni substrate. (b) Cyclic voltammograms of the Co oxide nanostructure as compared to flat Co oxide and the bare Ni substrate, measured in 1 M KOH solution with a potential scan rate of 10 mV s^{-1}.[244]

5. Nanostructured materials for hydrogen storage applications

Currently, a variety of solid-state hydrogen storage materials are the subject of intensive investigation and research, and several reviews exist on the topic.[238,301–303] However, no material has yet been discovered that simultaneously meets all of the following criteria: relatively high storage density of 3 kW h kg^{-1} at 9 wt% and 2.7 kW h L^{-1}, moderate decomposition temperatures of

60–120 °C, good reversibility, low manufacturing cost that can support $2 per kW h end-use pricing, and fast kinetics of the hydrogen absorption and desorption process.[304] Research in solid-state hydrogen storage appears to provide the highest probability of producing a material that can satisfy these generic criteria for hydrogen storage.

Nanostructures are attracting a lot of attention as sorbents for hydrogen storage.[305–310] Storage occurs through a process called physisorption, where the forces involved are weak intermolecular forces, generally resulting in fast kinetics and reversibility. But challenges associated with hydrogen physisorption also result from these weak forces. H_2 is the smallest molecule and only has two electrons, hence it is hard to polarize, and in the absence of relatively strong polarizing centers, interaction between the adsorbent and the non-polar hydrogen molecules relies on the weak dispersion forces. These are created by temporarily induced dipoles and are typically of the order of 3–6 kJ mol^{-1}.[311] Thus, significant hydrogen adsorption often takes place only at a cryogenic temperature.

Nanostructured materials may offer advantages over bulk materials for molecular hydrogen storage by providing high surface areas, or by encapsulating or trapping hydrogen in microporous media. Using porous nanostructured materials, in general, can reduce the gravimetric and volumetric storage densities. Additionally, the increased surface area and porosity in nanostructures offer additional binding sites on the surface and in the pores that could increase storage. The possibility of storing a significant amount of hydrogen on high surface area materials has been a key driver in the investigation of hydrogen sorption properties of nanostructured materials, including porous carbons, CNTs, graphene, zeolites, metal–organic frameworks, and polymers with intrinsic microporosity.

5.1 Nanomaterials for hydrogen storage

5.1.1 Carbon-based nanostructures for hydrogen storage. Early reports[312,313] on hydrogen storage in carbon nanotubes and graphitic nanofibers proposed high storage capacities (up to 67 wt%) and started an extensive worldwide surge of research. Since then many succeeding experiments have been carried out with different methods, but such high values have not yet been reproduced by other groups.[314] Furthermore, no hypothesis could support the unusually high storage capacities and therefore, the high storage capacity results were thought to be more related to the faults of experiment.[315,316] Nevertheless, hydrogen adsorption on carbon materials is still an attractive and improving field. The results of several investigations propose that the amount of adsorbed hydrogen is proportional to the specific surface area of the carbon material.[317,318] In the case of activated carbons and activated carbon fibers, the hydrogen absorption of 5 wt% is obtained at low temperature (77 K) and high pressure (30 to 60 bar).[319] For graphite nanofibers (GNFs), single walled nanotubes (SWNTs), and multi-walled nanotubes (MWNTs), the reversible hydrogen uptake of 1.5 wt% per 1000 m^2 g^{-1} under ambient conditions is reported.[320] Hydrogen capacity of 7 wt% at 77 K and 20 bar is observed for ordered porous carbon with a surface area
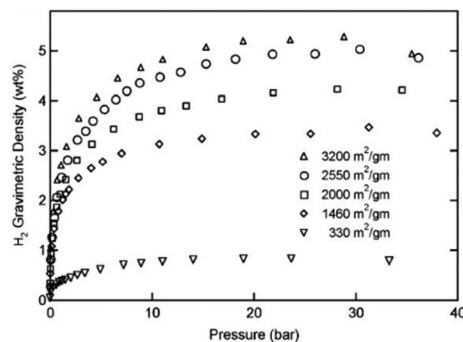

Fig. 39 Adsorption isotherms at 77 K for carbon aerogels show the linear dependency of hydrogen adsorption on the surface area.[321] Reprinted with permission from Kabbour et al., Chem. Mater., 2006, **18**(26), 6085–6087. Copyright 2006 American Chemical Society.

of 3200 m^2 g^{-1} prepared by template.[308] Recent studies on carbon aerogels (CAs), another class of amorphous porous carbon structures with high surface area, shows 5 wt% of hydrogen adsorption for a surface area of 3200 m^2 g^{-1} at 77 K and pressure 20–30 bar (Fig. 39).[321]

The recent increase in research of graphene for energy applications has also extended to hydrogen storage. Srinivas et al. showed that graphene-like nanosheets from exfoliated graphite oxide, shown in Fig. 40a, have an isosteric heat of adsorption (5.9 kJ mol^{-1}) comparable to high surface area carbons, indicating favorable interaction between hydrogen and the graphene sheets.[322] Subrahmanyam et al. achieved a hydrogen uptake of 3 wt% at 100 bar using exfoliated graphitic oxide with a specific surface area of 925 m^2 g^{-1}.[323] Increasing the surface area should increase the hydrogen storage capacity. However, while the theoretical surface area of graphene is above 2600 m^2 g^{-1}, the binding capacity of a single layer of graphene is very low, making a stacked structure necessary. Theoretical studies show that a layer of hydrogen can be stored in between two graphene sheets separated by a distance of 6 Å. It is believed that increasing the separation distance to 8 Å could result in the storage of two layers of hydrogen between graphene sheets, leading to a storage capacity of 5–6.5 wt% at 5 bar.[324]

Another way to use graphene is as support for metal nanoparticles. H_2 interactions with transition metals such as titanium
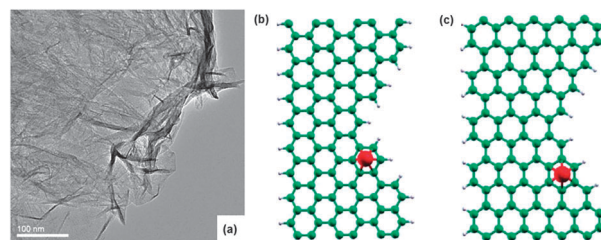
Fig. 40 (a) TEM image of graphene powder showing the crumpled morphology of a few layer graphene sheets.[322] Reproduced from ref. 322 with permission from Elsevier. (b) The optimized atomic structures of a Ca atom adsorbed on the armchair edge of a zigzag-armchair-edged graphene nanoribbon (GNR) and (c) the zigzag edge of an armchair-zigzag-edged GNR.[325] Reprinted with permission from Lee et al., Nano Lett., 2010, **10**(3), 793–798. Copyright 2010 American Chemical Society.

have been predicted to be strong enough to provide high hydrogen storage capacity. However, metal nanoparticles form clusters, lowering their accessibility to adsorb hydrogen effectively.[324,325] Calcium is emerging as an alternative because of the low cohesive energy (1.8 eV) in bulk. Lee *et al.* showed that calcium preferentially adsorbs onto the zigzag edge and boron-doped armchair edge of graphene, which suppresses clustering. The preferred structures for calcium on graphene are shown in Fig. 40b and c. Up to 6 H_2 molecules can attach to each calcium atom, leading to a gravimetric capacity of 5 wt% hydrogen.[325]

5.1.2 Zeolites, metal–organic frameworks, polymers. Zeolites are highly crystalline aluminosilicates with surface areas up to 1000 m^2 g^{-1} due to their open and rigid 3D structure.[326] Important parameters to consider when designing zeolites are pore volume and channel diameter, which ideally should be close to the kinetic diameter of the hydrogen molecule (2.98 Å).[327] Dong *et al.* prepared a series of zeolites with various channel diameters and pore volumes. Na-LEV, with a channel diameter of 3.6–4.8 Å, was shown to have a hydrogen uptake of approximately 2 wt% at 77 K and 16 bar, as seen in Fig. 41.[327] Because of the narrow pore distribution, zeolites have also been used as templates for forming porous carbon with surface areas up to 3200 m^2 g^{-1}, which leads to high storage capacity.[233]

There has been a recent increase in research concerning metal–organic frameworks (MOFs), which are microporous materials consisting of metal cluster building units connected by organic ligands. These materials have high crystallinity, high purity, and very high specific surface areas (up to 6240 m^2 g^{-1})[328] with controllable pore sizes.[233,303] The structure and chemistry can be easily tuned by varying the metal clusters and length and functionalization of the organic ligands.[329] For hydrogen storage, increasing the number of adsorptive sites in a material will increase the hydrogen uptake. In MOFs, this can be accomplished by using thin organic ligands with constituents available for gas adsorption. However, this may result in fragile frameworks,[328] in which case specialized drying techniques can be used, such as supercritical drying and freeze drying. These techniques prevent pore collapse, resulting in materials with very

high porosity.[303] Unsaturated metal sites are also helpful in increasing hydrogen storage due to their high hydrogen binding affinities. Often, these result in materials with high adsorptions enthalpies.[303] Several excellent reviews list recently developed MOFs and their hydrogen storage performance.[303,329]

Polymers with intrinsic porosity are also attractive for hydrogen storage because of their narrow pore size distribution and they have shown storage capacities that are comparable to other porous materials.[330,331] The intrinsic porosity arises from the shape and rigidity of the component macromolecules and is different from "extrinsic" templated porosity, in which a polymer matrix is molded around a rigid template.[332] The surface area and pore size distribution can be controlled by careful selection of the co-monomers, where decreasing the size of the monomer often results in smaller pores and increased surface area.[330] Polymers with intrinsic porosity can have specific surface areas of 400–1050 m^2 g^{-1}, and a narrow distribution of micropores that are 0.6–0.7 nm in diameter, which is favorable for hydrogen storage because of multiwall interactions.[233,332] The hydrogen storage capacity can reach 1.65 wt% at 1 bar and 77 K and 2.71 wt% at 10 bar for a polymer with a surface area of 1065 m^2 g^{-1}.[333]

5.1.3 Nanocomposites for hydrogen storage. The concept of a dual phase coherent nanocomposite hydrogen storage material has been developed and studied, where the two phases consist of a highly porous support material and a hydride hydrogen storage material.[206,248,334–336] Examples of hydride materials include sodium aluminum hydride ($NaAlH_4$), ammonia borane (NH_3BH_3), lithium borohydride ($LiBH_4$), *etc.* Often it is difficult to produce stable nanosized hydride materials, so the use of a nanoscaffold is attractive as it provides a tunable nanostructure with stabilized morphology.[233] Porous materials with a high surface area and pore volume can contribute significantly to a solid-state hydride-based hydrogen storage composite material by providing a structural support matrix, as well as size confinement for hydrides and a percolated heat conduction network.

Incorporation of $LiBH_4$ into carbon aerogels (CAs) has been shown to enhance the dehydrogenation kinetics and lower the dehydrogenating temperature of $LiBH_4$. Fig. 42 shows the thermo-gravimetric analysis for hydrogen release from $LiBH_4$ confined in two aerogels with pore sizes of 13 and 26 nm,
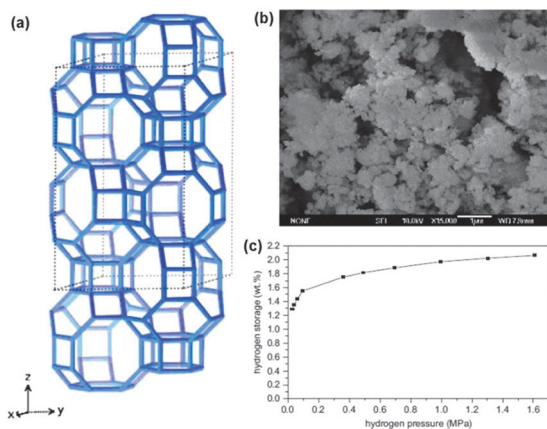
Fig. 41 Na-LEV zeolite: (a) schematic representation of a super cell, (b) SEM showing irregular crystal morphology, and (c) hydrogen desorption isotherm at 77 K.[327] Reproduced from ref. 327 with permission from Elsevier.
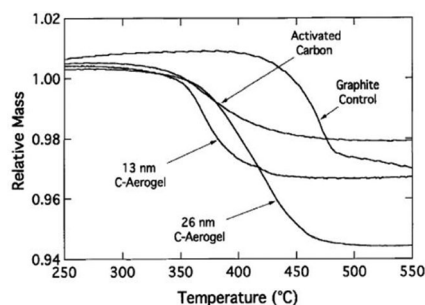
Fig. 42 Thermogravimetric analysis of $LiBH_4$ dehydrogenation, shows that the reaction temperatures decrease with decreasing scaffold pore size.[337] Reprinted with permission from Gross *et al.*, *J. Phys. Chem. C*, 2008, **112**(14), 5651–5657. Copyright 2008 American Chemical Society.
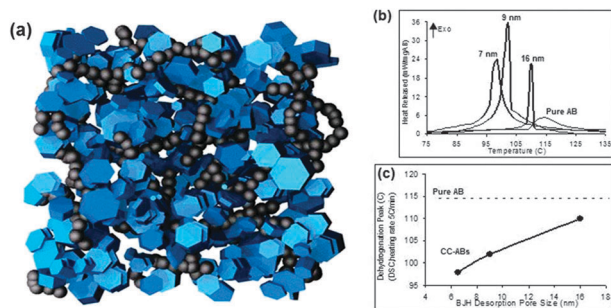
Fig. 43 (a) Illustration of the anticipated structure of a coherent nanocomposite consisting of a carbon cryogel network and hydride.[338] (b) Differential scanning calorimetry exotherms and (c) comparison of dehydration peaks for CC–AB nanocomposites with different pore size taken at 5 °C min^{-1}.[339] Reprinted with permission from Feaver *et al.*, *J. Phys. Chem. B*, 2007, **111**(26), 7469–7472. Copyright 2007 American Chemical Society. Reproduced from ref. 339 with permission from The Royal Society of Chemistry.

activated carbon with pore sizes of <2 nm, and a non-porous graphite control sample.[337] This study shows that incorporation of LiBH$_4$ into the CA accelerates the dehydrogenation, reduces the energy barrier to release hydrogen, and decreases the hydrogen release temperature, with a lower dehydrogenation temperature observed for the CA with smaller pore size.

Fig. 43a is a schematic illustrating a coherent nanocomposite of ammonia borane (AB) within a carbon cryogel network. AB has high gravimetric and volumetric hydrogen content, as well as a reasonable decomposition temperature. The addition of AB to the carbon cryogel resulted in hydrogen release at a much lower temperature than pure AB, showing evidence of faster kinetics. Fig. 43b and c show how the differential scanning calorimetry exotherms and dehydration peaks change with pore size, respectively. It can be seen that the dehydrogenation temperature decreases almost linearly with pore size. The carbon matrix reduces hydrogen diffusion distances, increases the frequency of reaction, which effectively accelerates the dehydrogenation process, and serves as efficient pathways for heat transfer. The nanocrystallite AB possesses a huge surface to volume ratio, resulting in significantly larger surface energy. This destabilizes the hydrogen bonding network of AB and lowers the barrier to hydrogen release.[338,339]

Nanosize confinement has been observed in silica–AB nanocomposites as well. Infusing AB in a nanoporous silica scaffold also lowers the activation barrier for hydrogen release, significantly improves the dehydrogenation kinetics, lowers the dehydrogenation temperature, and suppresses unwanted volatile products.[340] Gutowska *et al.* formed a nanocomposite by introducing an AB solution into a mesoporous silica SBA-15 scaffold. This resulted in a lower temperature threshold for H$_2$ release in the nanocomposite than pure ammonia borane, indicating an increased rate of H$_2$ release. Additionally, the amount of borazine, an unwanted volatile side product that affects the H$_2$ purity, was reduced.[340] In another study by Kim *et al.*, the AB incorporated into mesoporous silica MCM-41 experienced stabilization of its high-temperature disordered tetragonal phase at a much lower temperature than pure AB. The mesoporous silica changes the intermolecular interaction of the AB, greatly modifying the dehydration properties.[341]

5.2 Remarks

Nanostructured materials offer advantages for molecular hydrogen storage by reducing the gravimetric and the volumetric storage densities. Additionally, the increased surface area and porosity in nanostructures provide additional binding sites on the surface and in the pores that could increase storage. Typical hydrogen storage materials include highly porous carbon, CNTs, graphene, zeolites, metal–organic frameworks, and polymers with intrinsic microporosity. For carbon materials, it has been shown that hydrogen adsorption is linearly dependent on the surface area. Graphene can be used as a support for metal nanoparticles, but preventing clustering of the nanoparticles is necessary to retain effective hydrogen adsorption. For zeolites, some important parameters are pore volume and channel diameter. MOFs show great promise because of their high crystallinity, high purity, and extremely high surface area. However, the high surface area may result in fragile frameworks. For polymers with intrinsic porosity, the surface area and pore size distribution can be controlled by careful selection of the co-monomers, where decreasing the size of the monomer often results in smaller pores and increased surface area. Finally, forming nanocomposites of hydrides such as NaAlH$_4$, NH$_3$BH$_3$, and LiBH$_4$ on porous scaffold materials also represents a new promising area of research.

6. General conclusions and remarks

This review summarizes some of representative applications of nanostructured materials for solar cells, lithium ion batteries, supercapacitors, and hydrogen storage. As illustrated throughout this paper, nanostructured materials have proven to be effective in enhancing the performance of these devices in view of their novel geometrical characteristics and unique optical and electronic properties. In brief, nanostructures benefit these devices by (i) providing a large surface area to boost the electrochemical reaction or molecular adsorption occurring at the solid–liquid or solid–gas interface, (ii) generating optical effects that improve the optical absorption in solar cells, (iii) giving rise to high crystallinity and/or porous structure to facilitate both electron and ion transport and electrolyte diffusion, so as to ensure the electrochemical process occurs highly efficiently, and (iv) delivering new mechanisms, for example, the quantum confinement effect, which lead to nanostructured materials achieving energy conversion and storage more efficiently. However, while the advantages of nanostructured materials have been well documented, there are still several aspects of nanomaterials that need to be addressed.

(1) The *technology for material synthesis* is still facing a challenge in establishing controllable fabrication of nanostructures with the fully desired morphology, structure, facets, surface chemistry, *etc.* The feasibility of large-scale production and the cost relevant to both the materials themselves and the manufacturing process are also points of concern regarding material synthesis. A current trend is to use earth-abundant and nontoxic materials for the development of devices for

3164 | *Chem. Soc. Rev.*, 2013, **42**, 3127–3171

This journal is © The Royal Society of Chemistry 2013

renewable energy out of pivotal economic and environmental considerations.

(2) *More insightful understanding* of the relationship between the device performance and the material structure, including the chemical properties, with the aim to further develop the merits of nanostructured materials for enhancing the device performance in terms of reaction activity, optical absorption, electron or ion transport, *etc.*, is needed. An *optimization of the existing nanostructures* to maximize the contribution resulting from nanostructures is also necessary. For example, regarding the porous materials being used in electrochemical devices such as lithium ion batteries and supercapacitors, further work is anticipated to achieve more ideal structures that can well satisfy conflicting requirements for large internal surface area to provide sufficient reaction interface and large pore size for ease of electrolyte diffusion.

(3) *New mechanisms* relying on nanostructures are anticipated to increase the optical absorption and reduce the charge recombination, as well as other energy losses related to the electron transport in solar cells, and improve both the energy and power densities of lithium ion batteries. Developing *new material and structures* is always expected. For example, for lithium ion batteries, seeking reliable materials and suitable structures that can conduct the intercalation–deintercalation of lithium ions with high efficiency and meanwhile possess excellent cycling stability is one of key research themes in this field. In regard to the supercapacitors and hydrogen storage systems, current interests focus on composite materials and polymer-based materials that aim at achieving high storage density with low cost.

Acknowledgements

Notes and references

1 L. Banyai and S. W. Koch, *Semiconductor quantum dots*, World Scientific Publishing Company Incorporated, 1993.
2 A. P. Alivisatos, *Science*, 1996, **271**, 933–937.
3 Y. Wang and N. Herron, *J. Phys. Chem.*, 1991, **95**, 525–532.
4 V. I. Klimov, *Semiconductor and metal nanocrystals: synthesis and electronic and optical properties*, CRC, 2003.
5 S. K. Ghosh and T. Pal, *Chem. Rev.*, 2007, **107**, 4797–4862.
6 N. Felidj, J. Aubard, G. Levi, J. Krenn, A. Hohenau, G. Schider, A. Leitner and F. Aussenegg, *Appl. Phys. Lett.*, 2003, **82**, 3095–3097.
7 K. Kneipp, M. Moskovits and H. Kneipp, *Surface-enhanced Raman scattering: physics and applications*, Springer, 2006.
8 R. Sardar, A. M. Funston, P. Mulvaney and R. W. Murray, *Langmuir*, 2009, **25**, 13840–13851.
9 M. Haruta and M. Daté, *Appl. Catal., A*, 2001, **222**, 427–437.

10 M. Cortie and E. Van der Lingen, *Mater. Forum*, 2002, **26**, 1–14.
11 E. Roduner, *Chem. Soc. Rev.*, 2006, **35**, 583–592.
12 G. Cao, *Nanostructures & nanomaterials: synthesis, properties & applications*, World Scientific Publishing Company, 2004.
13 K. Koga, T. Ikeshoji and K. Sugawara, *Phys. Rev. Lett.*, 2004, **92**, 115507.
14 H. Petrova, M. Hu and G. V. Hartland, *Z. Phys. Chem.*, 2007, **221**, 361–376.
15 D. L. Leslie-Pelecky and R. D. Rieke, *Chem. Mater.*, 1996, **8**, 1770–1783.
16 R. Singh and J. W. Lillard Jr, *Exp. Mol. Pathol.*, 2009, **86**, 215–223.
17 J. K. Vasir, M. K. Reddy and V. D. Labhasetwar, *Curr. Nanosci.*, 2005, **1**, 47–64.
18 M. Terrones, *Annu. Rev. Mater. Res.*, 2003, **33**, 419–501.
19 M. Endo, M. Strano and P. Ajayan, *Top. Appl. Phys.*, 2008, **111**, 13–61.
20 M. Barati and E. Sadeghi, *Nanotechnology*, 2001, **12**, 277.
21 A. J. Frank, N. Kopidakis and J. Lagemaat, *Coord. Chem. Rev.*, 2004, **248**, 1165–1179.
22 D. Cahen, G. Hodes, M. Graetzel, J. F. Guillemoles and I. Riess, *J. Phys. Chem. B*, 2000, **104**, 2053–2059.
23 N. Robertson, *Angew. Chem., Int. Ed.*, 2006, **45**, 2338–2345.
24 G. Wang, L. Zhang and J. Zhang, *Chem. Soc. Rev.*, 2012, **41**, 797–828.
25 J. Fernandez, S. Tennison, O. Kozynchenko, F. Rubiera, F. Stoeckli and T. Centeno, *Carbon*, 2009, **47**, 1598–1604.
26 A. S. Edelstein and R. Cammaratra, *Nanomaterials: synthesis, properties and applications*, Taylor & Francis, 1998.
27 G. A. Ozin, A. C. Arsenault and L. Cademartiri, *Nanochemistry: a chemical approach to nanomaterials*, Royal Society of Chemistry, 2008.
28 H. Hosono, Y. Mishima, H. Takezoe and K. J. D. MacKenzie, *Nanomaterials: Research Towards Applications*, Elsevier Science, 2006.
29 J. A. Rodriguez and M. Fernández-García, *Synthesis, properties, and applications of oxide nanomaterials*, Wiley-Interscience, 2007.
30 P. Balbuena and J. M. Seminario, *Nanomaterials: Design and Simulation: Design and Simulation*, Elsevier Science, 2006.
31 M. U. Niemann, S. S. Srinivasan, A. R. Phani, A. Kumar, D. Y. Goswami and E. K. Stefanakos, *J. Nanomater.*, 2008, **2008**, 950967–950975.
32 P. G. Bruce, B. Scrosati and J. M. Tarascon, *Angew. Chem., Int. Ed.*, 2008, **47**, 2930–2946.
33 J. Davenas, A. Ltaief, V. Barlier, G. Boiteux and A. Bouazizi, *Mater. Sci. Eng., C*, 2008, **28**, 744–750.
34 X. Hu, G. Li and J. C. Yu, *Langmuir*, 2009, **26**, 3031–3039.
35 Y. Li and G. A. Somorjai, *Nano Lett.*, 2010, **10**, 2289–2295.
36 S. S. Srinivasan, A. R. Phani, A. Kumar, D. Y. Goswami and E. K. Stefanakos, *J. Nanomater.*, 2008, **2008**, 950967.
37 Z. Y. Zhou, N. Tian, J. T. Li, I. Broadwell and S. G. Sun, *Chem. Soc. Rev.*, 2011, **40**, 4167–4185.

38 P. Balaya, *Energy Environ. Sci.*, 2008, **1**, 645–654.

39 M. O. Manasreh, *Introduction to Nanomaterials and Devices*, Wiley Online Library, 2012.

40 M. F. Ashby, P. J. S. G. Ferreira and D. L. Schodek, *Nanomaterials, nanotechnologies and design: an introduction for engineers and architects*, Elsevier, 2009.

41 H. T. Grahn, *Introduction to semiconductor physics*, World Scientific Pub Co Inc, 1999.

42 B. D. Fahlman, *Materials Chemistry*, Springer, 2011.

43 I. Kang and F. W. Wise, *J. Opt. Soc. Am. B*, 1997, **14**, 1632–1646.

44 H. Du, C. Chen, R. Krishnan, T. D. Krauss, J. M. Harbold, F. W. Wise, M. G. Thomas and J. Silcox, *Nano Lett.*, 2002, **2**, 1321–1324.

45 T. H. Kim, K. S. Cho, E. K. Lee, S. J. Lee, J. Chae, J. W. Kim, J. Y. Kwon, G. Amaratunga, S. Y. Lee and B. L. Choi, *Nat. Photonics*, 2011, **5**, 176–182.

46 J. Kwak, W. K. Bae, D. Lee, I. Park, J. Lim, M. Park, H. Cho, H. Woo, D. Y. Yoon and K. Char, *Nano Lett.*, 2012, **12**, 2362–2366.

47 P. V. Kamat, *Acc. Chem. Res.*, 2012, **45**, 1906–1915.

48 Z. Yang, C. Y. Chen, P. Roy and H. T. Chang, *Chem. Commun.*, 2011, **47**, 9561–9571.

49 Q. Zhang, X. Guo, X. Huang, S. Huang, D. Li, Y. Luo, Q. Shen, T. Toyoda and Q. Meng, *Phys. Chem. Chem. Phys.*, 2011, **13**, 4659–4667.

50 J. A. Chang, J. H. Rhee, S. H. Im, Y. H. Lee, H. Kim, S. I. Seok, M. K. Nazeeruddin and M. Gratzel, *Nano Lett.*, 2010, **10**, 2609–2612.

51 M. C. Beard, A. G. Midgett, M. C. Hanna, J. M. Luther, B. K. Hughes and A. J. Nozik, *Nano Lett.*, 2010, **10**, 3019–3027.

52 M. C. Beard and R. J. Ellingson, *Laser Photonics Rev.*, 2008, **2**, 377–399.

53 J. A. McGuire, J. Joo, J. M. Pietryga, R. D. Schaller and V. I. Klimov, *Acc. Chem. Res.*, 2008, **41**, 1810–1819.

54 J. Pijpers, R. Ulbricht, K. Tielrooij, A. Osherov, Y. Golan, C. Delerue, G. Allan and M. Bonn, *Nat. Phys.*, 2009, **5**, 811–814.

55 N. Gupta, G. Alapatt, R. Podila, R. Singh and K. Poole, *Int. J. Photoenergy*, 2009, **2009**, 154059.

56 A. J. Nozik, *Chem. Phys. Lett.*, 2008, **457**, 3–11.

57 M. Hanna and A. J. Nozik, *J. Appl. Phys.*, 2006, **100**, 074510.

58 W. Shockley and H. J. Queisser, *J. Appl. Phys.*, 1961, **32**, 510–519.

59 O. E. Semonin, J. M. Luther, S. Choi, H. Y. Chen, J. Gao, A. J. Nozik and M. C. Beard, *Science*, 2011, **334**, 1530–1533.

60 M. Grätzel and J. R. Durrant, in *Series on Photoconversion of Solar Energy: Nanostructured and Photoelectrochemical Systems for Solar Photon Conversion*, ed. M. D. Archer and A. J. Nozik, 2008, vol. 3, pp. 503–536.

61 B. O'Regan and M. Grätzel, *Nature*, 1991, **353**, 737–740.

62 M. Grätzel, *J. Photochem. Photobiol., A*, 2004, **164**, 3–14.

63 M. Grätzel, *J. Photochem. Photobiol., C*, 2003, **4**, 145–153.

64 Q. F. Zhang and G. Z. Cao, *Nano Today*, 2011, **6**, 91–109.

65 Q. F. Zhang, C. S. Dandeneau, X. Y. Zhou and G. Z. Cao, *Adv. Mater.*, 2009, **21**, 4087–4108.

66 Q. F. Zhang, S. Yodyingyong, J. T. Xi, D. Myers and G. Z. Cao, *Nanoscale*, 2012, **4**, 1436–1445.

67 J. Kroon, N. Bakker, H. Smit, P. Liska, K. Thampi, P. Wang, S. Zakeeruddin, M. Grätzel, A. Hinsch and S. Hore, *Prog. Photovoltaics*, 2007, **15**, 1–18.

68 A. Yella, H. W. Lee, H. N. Tsao, C. Yi, A. K. Chandiran, M. K. Nazeeruddin, E. W. G. Diau, C. Y. Yeh, S. M. Zakeeruddin and M. Grätzel, *Science*, 2011, **334**, 629–634.

69 B. E. Hardin, H. J. Snaith and M. D. McGehee, *Nat. Photonics*, 2012, **6**, 162–169.

70 J. Tang, J. Shi, L. Zhou and Z. Ma, *Nano-Micro Lett.*, 2011, **3**, 129–134.

71 S. L. Diedenhofen, G. Vecchi, R. E. Algra, A. Hartsuiker, O. L. Muskens, G. Immink, E. P. A. M. Bakkers, W. L. Vos and J. G. Rivas, *Adv. Mater.*, 2009, **21**, 973–978.

72 J. Y. Jung, Z. Guo, S. W. Jee, H. D. Um, K. T. Park and J. H. Lee, *Opt. Express*, 2010, **18**, A286–A292.

73 K. Nishioka, T. Sueto and N. Saito, *Appl. Surf. Sci.*, 2009, **255**, 9504–9507.

74 J. Zhu, Z. Yu, G. F. Burkhard, C. M. Hsu, S. T. Connor, Y. Xu, Q. Wang, M. McGehee, S. Fan and Y. Cui, *Nano Lett.*, 2008, **9**, 279–282.

75 Y. Lee, K. Koh, H. Na, K. Kim, J. J. Kang and J. Kim, *Nanoscale Res. Lett.*, 2009, **4**, 364–370.

76 C. M. Hsu, S. T. Connor, M. X. Tang and Y. Cui, *Appl. Phys. Lett.*, 2008, **93**, 133109.

77 J. Zhu, Z. Yu, S. Fan and Y. Cui, *Mater. Sci. Eng., R*, 2010, **70**, 330–340.

78 L. Vayssieres, K. Keis, S. E. Lindquist and A. Hagfeldt, *J. Phys. Chem. B*, 2001, **105**, 3350–3352.

79 L. Vayssieres, *Adv. Mater.*, 2003, **15**, 464–466.

80 Y. J. Lee, D. S. Ruby, D. W. Peters, B. B. McKenzie and J. W. P. Hsu, *Nano Lett.*, 2008, **8**, 1501–1505.

81 Y. C. Chao, C. Y. Chen, C. A. Lin, Y. A. Dai and J. H. He, *J. Mater. Chem.*, 2010, **20**, 8134–8138.

82 J. Q. Xi, M. F. Schubert, J. K. Kim, E. F. Schubert, M. Chen, S. Y. Lin, W. Liu and J. A. Smart, *Nat. Photonics*, 2007, **1**, 176–179.

83 P. Bharadwaj, B. Deutsch and L. Novotny, *Adv. Opt. Photonics*, 2009, **1**, 438–483.

84 V. E. Ferry, J. N. Munday and H. A. Atwater, *Adv. Mater.*, 2010, **22**, 4794–4808.

85 K. Catchpole and A. Polman, *Appl. Phys. Lett.*, 2008, **93**, 191113.

86 S. Varlamov, Z. Ouyang, X. Zhao and D. Jung, *Photonics Global Conference (PGC), 2010*, 2010.

87 D. Derkacs, S. Lim, P. Matheu, W. Mar and E. Yu, *Appl. Phys. Lett.*, 2006, **89**, 093103.

88 K. Nakayama, K. Tanabe and H. A. Atwater, *Appl. Phys. Lett.*, 2008, **93**, 121904.

89 L. Qiao, D. Wang, L. Zuo, Y. Ye, J. Qian, H. Chen and S. He, *Appl. Energy*, 2011, **88**, 848–852.

90 S. S. Kim, S. I. Na, J. Jo, D. Y. Kim and Y. C. Nah, *Appl. Phys. Lett.*, 2008, **93**, 073307.

91 N. C. Jeong, C. Prasittichai and J. Hupp, *Langmuir*, 2011, **27**, 14609–14614.

3166 | *Chem. Soc. Rev.*, 2013, **42**, 3127–3171

This journal is © The Royal Society of Chemistry 2013

92 C. Photiphitak, P. Rakkwamsuk, P. Muthitamongkol, C. Sae-Kung and C. Thanachayanont, *Int. J. Photoenergy*, 2011, **2011**, 258635.

93 B. Ding, B. J. Lee, M. Yang, H. S. Jung and J. K. Lee, *Adv. Energy Mater.*, 2011, **1**, 415–421.

94 M. Heo, H. Cho, J. W. Jung, J. R. Jeong, S. Park and J. Y. Kim, *Adv. Mater.*, 2011, **23**, 5689–5693.

95 S. Pillai and M. Green, *Sol. Energy Mater. Sol. Cells*, 2010, **94**, 1481–1486.

96 H. A. Atwater and A. Polman, *Nat. Mater.*, 2010, **9**, 205–213.

97 Y. H. Su, Y. F. Ke, S. L. Cai and Q. Y. Yao, *Light: Sci. Appl.*, 2012, **1**, e14.

98 A. Furube, L. Du, K. Hara, R. Katoh and M. Tachiya, *J. Am. Chem. Soc.*, 2007, **129**, 14852–14853.

99 Q. F. Zhang, T. R. Chou, B. Russo, S. A. Jenekhe and G. Z. Cao, *Angew. Chem., Int. Ed.*, 2008, **47**, 2402–2406.

100 Q. F. Zhang, T. P. Chou, B. Russo, S. A. Jenekhe and G. Cao, *Adv. Funct. Mater.*, 2008, **18**, 1654–1660.

101 T. P. Chou, Q. F. Zhang, G. E. Fryxell and G. Z. Cao, *Adv. Mater.*, 2007, **19**, 2588–2592.

102 J. T. Xi, Q. F. Zhang, S. H. Xie, S. Yodyingyong, K. Park, Y. M. Sun, J. Y. Li and G. Z. Cao, *Nanosci. Nanotechnol. Lett.*, 2011, **3**, 690–696.

103 Q. F. Zhang, K. Park, J. T. Xi, D. Myers and G. Z. Cao, *Adv. Energy Mater.*, 2011, **1**, 988–1001.

104 L. Loeb, A. Kip, G. Hudson and W. Bennett, *Phys. Rev.*, 1941, **60**, 714.

105 N. G. Park, J. Van de Lagemaat and A. Frank, *J. Phys. Chem. B*, 2000, **104**, 8989–8994.

106 D. Chen, L. Cao, F. Huang, P. Imperia, Y. B. Cheng and R. A. Caruso, *J. Am. Chem. Soc.*, 2010, **132**, 4438–4444.

107 D. Chen, F. Huang, Y. B. Cheng and R. A. Caruso, *Adv. Mater.*, 2009, **21**, 2206–2210.

108 F. Sauvage, D. Chen, P. Comte, F. Huang, L. P. Heiniger, Y. B. Cheng, R. A. Caruso and M. Graetzel, *ACS Nano*, 2010, **4**, 4420–4425.

109 J. Qian, P. Liu, Y. Xiao, Y. Jiang, Y. Cao, X. Ai and H. Yang, *Adv. Mater.*, 2009, **21**, 3663–3667.

110 X. Wu, G. Q. M. Lu and L. Wang, *Energy Environ. Sci.*, 2011, **4**, 3565–3572.

111 X. Lai, J. E. Halpert and D. Wang, *Energy Environ. Sci.*, 2012, **5**, 5604–5618.

112 M. Law, L. E. Greene, J. C. Johnson, R. Saykally and P. Yang, *Nat. Mater.*, 2005, **4**, 455–459.

113 S. Yodyingyong, Q. Zhang, K. Park, C. S. Dandeneau, X. Zhou, D. Triampo and G. Cao, *Appl. Phys. Lett.*, 2010, **96**, 073115.

114 J. B. Baxter, A. Walker, K. Van Ommering and E. Aydil, *Nanotechnology*, 2006, **17**, S304.

115 J. Qiu, X. Li, F. Zhuge, X. Gan, X. Gao, W. He, S. J. Park, H. K. Kim and Y. H. Hwang, *Nanotechnology*, 2010, **21**, 195602.

116 C. Xu, P. Shin, L. Cao and D. Gao, *J. Phys. Chem. C*, 2009, **114**, 125–129.

117 M. Law, L. E. Greene, A. Radenovic, T. Kuykendall, J. Liphardt and P. Yang, *J. Phys. Chem. B*, 2006, **110**, 22652–22663.

118 A. Irannejad, K. Janghorban, O. K. Tan, H. Huang, C. K. Lim, P. Y. Tan, X. Fang, C. S. Chua, S. Maleksaeedi, S. M. H. Hejazi, M. M. Shahjamali and M. Ghaffari, *Electrochim. Acta*, 2011, **58**, 19–24.

119 K. Shankar, G. K. Mor, H. E. Prakasam, S. Yoriya, M. Paulose, O. K. Varghese and C. A. Grimes, *Nanotechnology*, 2007, **18**, 065707.

120 J. Wang and Z. Lin, *Chem. Mater.*, 2009, **22**, 579–584.

121 X. Pan, C. Chen, K. Zhu and Z. Fan, *Nanotechnology*, 2011, **22**, 235402.

122 O. Wiranwetchayan, Q. F. Zhang, X. Y. Zhou, Z. Q. Liang, P. Singjai and G. Z. Cao, *Chalcogenide Lett.*, 2012, **9**, 157–163.

123 Z. Q. Liang, Q. F. Zhang, O. Wiranwetchayan, J. T. Xi, Z. Yang, K. Park, C. D. Li and G. Z. Cao, *Adv. Funct. Mater.*, 2012, **22**, 2194–2201.

124 J. Xi, O. Wiranwetchayan, Q. Zhang, Z. Liang, Y. Sun and G. Cao, *J. Mater. Sci.: Mater. Electron.*, 2012, 1–7.

125 S. Yodyingyong, X. Zhou, Q. Zhang, D. Triampo, J. Xi, K. Park, B. Limketkai and G. Cao, *J. Phys. Chem. C*, 2010, **114**, 21851–21855.

126 T. P. Chou, Q. F. Zhang and G. Z. Cao, *J. Phys. Chem. C*, 2007, **111**, 18804–18811.

127 Q. Zhang, C. S. Dandeneau, X. Zhou and G. Cao, *Adv. Mater.*, 2009, **21**, 4087–4108.

128 N. Tetreault, E. Arsenault, L. P. Heiniger, N. Soheilnia, J. Brillet, T. Moehl, S. Zakeeruddin, G. A. Ozin and M. Grätzel, *Nano Lett.*, 2011, **11**, 4579–4584.

129 J. B. Goodenough and Y. Kim, *Chem. Mater.*, 2010, **22**, 587–603.

130 Y.-G. Guo, J.-S. Hu and L.-J. Wan, *Adv. Mater.*, 2008, **20**, 2878–2887.

131 D. Liu and G. Cao, *Energy Environ. Sci.*, 2010, **3**, 1218–1237.

132 B. Scrosati and J. Garche, *J. Power Sources*, 2010, **195**, 2419–2430.

133 P. Balaya, A. J. Bhattacharyya, J. Jamnik, Y. F. Zhukovskii, E. A. Kotomin and J. Maier, *J. Power Sources*, 2006, **159**, 171–178.

134 Y. Liu, D. Liu, Q. Zhang, D. Yu, J. Liu and G. Cao, *Electrochim. Acta*, 2011, **56**, 2559–2565.

135 P. G. Bruce, B. Scrosati and J.-M. Tarascon, *Angew. Chem., Int. Ed.*, 2008, **47**, 2930–2946.

136 C. Delmas, H. Cognacauradou, J. M. Cocciantelli, M. Menetrier and J. P. Doumerc, *Solid State Ionics*, 1994, **69**, 257–264.

137 M. Wagemaker, W. J. H. Borghols and F. M. Mulder, *J. Am. Chem. Soc.*, 2007, **129**, 4323–4327.

138 M. Wagemaker, A. P. M. Kentgens and F. M. Mulder, *Nature*, 2002, **418**, 397–399.

139 S. Ganapathy, E. R. van Eck, A. P. M. Kentgens, F. M. Mulder and M. Wagemaker, *Chem.–Eur. J.*, 2011, **17**, 14811–14816.

140 Y. S. Hu, L. Kienle, Y. G. Guo and J. Maier, *Adv. Mater.*, 2006, **18**, 1421–1426.

141 W. J. H. Borghols, M. Wagemaker, U. Lafont, E. M. Kelder and F. M. Mulder, *J. Am. Chem. Soc.*, 2009, **131**, 17786–17792.

142 Y. Liu, M. Clark, Q. Zhang, D. Yu, D. Liu, J. Liu and G. Cao, *Adv. Energy Mater.*, 2011, **1**, 194–202.

143 Y. Y. Liu, J. G. Li, Q. F. Zhang, N. Zhou, E. Uchaker and G. Z. Cao, *Electrochem. Commun.*, 2011, **13**, 1276–1279.

144 R. A. Huggins and W. D. Nix, *Ionics*, 2000, **6**, 57–63.

145 H. Li, *Electrochem. Solid-State Lett.*, 1999, **2**, 547.

146 C. K. Chan, H. Peng, G. Liu, K. McIlwrath, X. F. Zhang, R. A. Huggins and Y. Cui, *Nat. Nanotechnol.*, 2008, **3**, 31–35.

147 N. Meethong, H.-Y. S. Huang, W. C. Carter and Y.-M. Chiang, *Electrochem. Solid-State Lett.*, 2007, **10**, A134.

148 G. Kobayashi, S.-i. Nishimura, M.-S. Park, R. Kanno, M. Yashima, T. Ida and A. Yamada, *Adv. Funct. Mater.*, 2009, **19**, 395–403.

149 M. Wagemaker, D. P. Singh, W. J. Borghols, U. Lafont, L. Haverkate, V. K. Peterson and F. M. Mulder, *J. Am. Chem. Soc.*, 2011, **133**, 10222–10228.

150 A. G. Dylla, P. Xiao, G. Henkelman and K. J. Stevenson, *J. Phys. Chem. Lett.*, 2012, **3**, 2015–2019.

151 W. Q. Fang, X.-Q. Gong and H. G. Yang, *J. Phys. Chem. Lett.*, 2011, **2**, 725–734.

152 H. G. Yang, C. H. Sun, S. Z. Qiao, J. Zou, G. Liu, S. C. Smith, H. M. Cheng and G. Q. Lu, *Nature*, 2008, **453**, 638–641.

153 J. Liu and X. W. Liu, *Adv. Mater.*, 2012, **24**, 4097–4111.

154 B. Wu, C. Guo, N. Zheng, Z. Xie and G. D. Stucky, *J. Am. Chem. Soc.*, 2008, **130**, 17563–17567.

155 J. S. Chen, Y. L. Tan, C. M. Li, Y. L. Cheah, D. Luan, S. Madhavi, F. Y. C. Boey, L. A. Archer and X. W. Lou, *J. Am. Chem. Soc.*, 2010, **132**, 6124–6130.

156 S. Ding, J. S. Chen, Z. Wang, Y. L. Cheah, S. Madhavi, X. Hu and X. W. Lou, *J. Mater. Chem.*, 2011, **21**, 1677.

157 Y. Yu, X. Wang, H. Sun and M. Ahmad, *RSC Adv.*, 2012, **2**, 7901.

158 L. Liu, Q. Fan, C. Sun, X. Gu, H. Li, F. Gao, Y. Chen and L. Dong, *J. Power Sources*, 2013, **221**, 141–148.

159 J. S. Chen, Y. L. Tan, C. M. Li, Y. L. Cheah, D. Luan, S. Madhavi, F. Y. C. Boey, L. A. Archer and X. W. Lou, *J. Am. Chem. Soc.*, 2010, **132**, 6124–6130.

160 S. Ganapathy and M. Wagemaker, *ACS Nano*, 2012, **6**, 8702–8712.

161 W. Sun, F. Cao, Y. Liu, X. Zhao, X. Liu and J. Yuan, *J. Mater. Chem.*, 2012, **22**, 20952.

162 L. Liang, M. Zhou and Y. Xie, *Chem.–Asian J.*, 2012, **7**, 565–571.

163 L. Wang, X. He, W. Sun, J. Wang, Y. Li and S. Fan, *Nano Lett.*, 2012, **12**, 5632–5636.

164 X.-L. Pan, C.-Y. Xu and L. Zhen, *CrystEngComm*, 2012, **14**, 6412.

165 S. C. Jung and Y. K. Han, *Phys. Chem. Chem. Phys.*, 2011, **13**, 21282–21287.

166 M. Pharr, K. Zhao, X. Wang, Z. Suo and J. J. Vlassak, *Nano Lett.*, 2012, **12**, 5039–5047.

167 A. Nel, T. Xia, L. Madler and N. Li, *Science*, 2006, **311**, 622–627.

168 V. L. Colvin, *Nat. Biotechnol.*, 2003, **21**, 1166–1170.

169 S. Zhang, Y. Li, C. Wu, F. Zheng and Y. Xie, *J. Phys. Chem. C*, 2009, **113**, 15058–15067.

170 P. Nie, L. F. Shen, H. F. Zhang, L. Chen, H. Denga and X. G. Zhang, *CrystEngComm*, 2012, **14**, 4284–4288.

171 Q. Wang, W. Zhang, Z. Yang, S. Weng and Z. Jin, *J. Power Sources*, 2011, **196**, 10176–10182.

172 F. Caruso, R. A. Caruso and H. Mohwald, *Science*, 1998, **282**, 1111–1114.

173 J. Liu and D. Xue, *Nanoscale Res. Lett.*, 2010, **5**, 1525–1534.

174 D. Zhu, H. Liu, H. Lv, Y. D. Yao and W. Z. Yang, *Scr. Mater.*, 2008, **59**, 642–645.

175 S. Wang, Z. Lu, D. Wang, C. Li, C. Chen and Y. Yin, *J. Mater. Chem.*, 2011, **21**, 6365–6369.

176 J. Luo, L. Cheng and Y. Xia, *Electrochem. Commun.*, 2007, **9**, 1404–1409.

177 J. Liu, H. Xia, D. Xue and L. Lu, *J. Am. Chem. Soc.*, 2009, **131**, 12086.

178 X. W. Lou and L. A. Archer, *Adv. Mater.*, 2008, **20**, 1853.

179 G. C. Hui Wu, J. W. Choi, I. Ryu, Y. Yao, M. T. McDowell, S. W. Lee, A. Jackson, Y. Yang, L. Hu and Y. Cui, *Nat. Nanotechnol.*, 2012, **7**, 310–315.

180 C. O'Dwyer, D. Navas, V. Lavayen, E. Benavente, M. A. Santa Ana, G. Gonzalez, S. B. Newcomb and C. M. S. Torres, *Chem. Mater.*, 2006, **18**, 3016–3022.

181 G. Li, K. Chao, C. Zhang, Q. Zhang, H. Peng and K. Chen, *Inorg. Chem.*, 2009, **48**, 1168–1172.

182 C. Liu, F. Li, L.-P. Ma and H.-M. Cheng, *Adv. Mater.*, 2010, **22**, E28.

183 W.-M. Zhang, J.-S. Hu, Y.-G. Guo, S.-F. Zheng, L.-S. Zhong, W.-G. Song and L.-J. Wan, *Adv. Mater.*, 2008, **20**, 1160.

184 K. T. Lee, Y. S. Jung and S. M. Oh, *J. Am. Chem. Soc.*, 2003, **125**, 5652–5653.

185 G. Zheng, Y. Yang, J. J. Cha, S. S. Hong and Y. Cui, *Nano Lett.*, 2011, **11**, 4462–4467.

186 N. Liu, H. Wu, M. T. McDowell, Y. Yao, C. Wang and Y. Cui, *Nano Lett.*, 2012, **12**, 3315–3321.

187 Y. Wang and G. Z. Cao, *Chem. Mater.*, 2006, **18**, 2787–2804.

188 H. Colfen and M. Antonietti, *Angew. Chem., Int. Ed.*, 2005, **44**, 5576–5591.

189 M. Niederberger and H. Coelfen, *Phys. Chem. Chem. Phys.*, 2006, **8**, 3271–3287.

190 R.-Q. Song and H. Coelfen, *Adv. Mater.*, 2010, **22**, 1301–1330.

191 F. C. Meldrum and H. Coelfen, *Nanoscale*, 2010, **2**, 2326–2327.

192 R.-Q. Song and H. Coelfen, *CrystEngComm*, 2011, **13**, 1249–1276.

193 V. M. Yuwono, N. D. Burrows, J. A. Soltis and R. L. Penn, *J. Am. Chem. Soc.*, 2010, **132**, 2163–2165.

194 A. M. Cao, J. S. Hu, H. P. Liang and L. J. Wan, *Angew. Chem., Int. Ed.*, 2005, **44**, 4391–4395.

195 J. Ye, W. Liu, J. Cai, S. Chen, X. Zhao, H. Zhou and L. Qi, *J. Am. Chem. Soc.*, 2011, **133**, 933–940.

196 Z. Hong, Y. Xu, Y. Liu and M. Wei, *Chem.–Eur. J.*, 2012, **18**, 10753–10760.

197 I. Bilecka, A. Hintennach, I. Djerdj, P. Novak and M. Niederberger, *J. Mater. Chem.*, 2009, **19**, 5125–5128.

198 Y. Xia, W. K. Zhang, H. Huang, Y. P. Gan, J. Tian and X. Y. Tao, *J. Power Sources*, 2011, **196**, 5651–5658.

3168 | *Chem. Soc. Rev.*, 2013, **42**, 3127–3171

This journal is © The Royal Society of Chemistry 2013

199 M. S. Whittingham, *Science*, 1976, **192**, 1126–1127.

200 K.-S. Park, A. Benayad, D.-J. Kang and S.-G. Doo, *J. Am. Chem. Soc.*, 2008, **130**, 14930.

201 P. R. Abel, Y. M. Lin, H. Celio, A. Heller and C. B. Mullins, *ACS Nano*, 2012, **6**, 2506–2516.

202 W. Xu, S. S. S. Vegunta and J. C. Flake, *J. Power Sources*, 2011, **196**, 8583–8589.

203 L. J. Fu, H. Liu, C. Li, Y. P. Wu, E. Rahm, R. Holze and H. Q. Wu, *Solid State Sci.*, 2006, **8**, 113–128.

204 Z. Chen, Y. Qin, K. Amine and Y. K. Sun, *J. Mater. Chem.*, 2010, **20**, 7606.

205 D. R. Rolison and B. Dunn, *J. Mater. Chem.*, 2001, **11**, 963–980.

206 A. F. Gross, C. C. Ahn, S. L. Van Atta, P. Liu and J. J. Vajo, *Nanotechnology*, 2009, **20**, 204005–204010.

207 D. Liu, Y. Liu, A. Pan, K. P. Nagle, G. T. Seidler, Y.-H. Jeong and G. Cao, *J. Phys. Chem. C*, 2011, **115**, 4959–4965.

208 D. Liu, Y. Zhang, P. Xiao, B. B. Garcia, Q. Zhang, X. Zhou, Y.-H. Jeong and G. Cao, *Electrochim. Acta*, 2009, **54**, 6816–6820.

209 K. E. Swider-Lyons, C. T. Love and D. R. Rolison, *Solid State Ionics*, 2002, **152**, 99–104.

210 D. Sun, C. W. Kwon, G. Baure, E. Richman, J. MacLean, B. Dunn and S. H. Tolbert, *Adv. Funct. Mater.*, 2004, **14**, 1197–1204.

211 B. Guo, X. Wang, P. F. Fulvio, M. Chi, S. M. Mahurin, X.-G. Sun and S. Dai, *Adv. Mater.*, 2011, **23**, 4661.

212 A. L. M. Reddy, A. Srivastava, S. R. Gowda, H. Gullapalli, M. Dubey and P. M. Ajayan, *ACS Nano*, 2010, **4**, 6337–6342.

213 D. Y. Pan, S. Wang, B. Zhao, M. H. Wu, H. J. Zhang, Y. Wang and Z. Jiao, *Chem. Mater.*, 2009, **21**, 3136–3142.

214 K.-S. Park, P. Xiao, S.-Y. Kim, A. Dylla, Y.-M. Choi, G. Henkelman, K. J. Stevenson and J. B. Goodenough, *Chem. Mater.*, 2012, **24**, 3212–3218.

215 M. Wagemaker, F. M. Mulder and A. Van der Ven, *Adv. Mater.*, 2009, **21**, 2703–2709.

216 M. N. Ou, S. R. Harutyunyan, S. J. Lai, C. D. Chen, T. J. Yang and Y. Y. Chen, *Phys. Status Solidi B*, 2007, **244**, 4512–4517.

217 B. V. Ratnakumar, M. C. Smart and S. Surampudi, *J. Power Sources*, 2001, **97–98**, 137–139.

218 F. Béguin, F. Chevallier, C. Vix-Guterl, S. Saadallah, V. Bertagna, J. N. Rouzaud and E. Frackowiak, *Carbon*, 2005, **43**, 2160–2167.

219 J. Yamaki, H. Takatsuji, T. Kawamura and M. Egashira, *Solid State Ionics*, 2002, **148**, 241–245.

220 A. Lewandowski and A. Świderska-Mocek, *J. Power Sources*, 2009, **194**, 601–609.

221 S. S. Zhang, *J. Power Sources*, 2006, **162**, 1379–1394.

222 K. Edström, A. M. Andersson, A. Bishop, L. Fransson, J. Lindgren and A. Hussénius, *J. Power Sources*, 2001, **97–98**, 87–91.

223 Y.-S. Park and S.-M. Lee, *Electrochim. Acta*, 2009, **54**, 3339–3343.

224 M. Jo, Y.-S. Hong, J. Choo and J. Cho, *J. Electrochem. Soc.*, 2009, **156**, A430–A434.

225 J. L. Lei, L. J. Li, R. Kostecki, R. Muller and F. McLarnon, *J. Electrochem. Soc.*, 2005, **152**, A774–A777.

226 J. F. Martin, A. Yamada, G. Kobayashi, S.-i. Nishimura, R. Kanno, D. Guyomard and N. Dupré, *Electrochem. Solid-State Lett.*, 2008, **11**, A12.

227 H. Li, L. H. Shi, Q. Wang, L. Q. Chen and X. J. Huang, *Solid State Ionics*, 2002, **148**, 247–258.

228 D. H. Jang, Y. J. Shin and S. M. Oh, *J. Electrochem. Soc.*, 1996, **143**, 2204–2211.

229 D. H. Jang and S. M. Oh, *J. Electrochem. Soc.*, 1997, **144**, 3342–3348.

230 T.-F. Yi, Y.-R. Zhu, X.-D. Zhu, J. Shu, C.-B. Yue and A.-N. Zhou, *Ionics*, 2009, **15**, 779–784.

231 J. H. Kim, K. Zhu, Y. F. Yan, C. L. Perkins and A. J. Frank, *Nano Lett.*, 2010, **10**, 4099–4104.

232 Y. Korenblit, M. Rose, E. Kockrick, L. Borchardt, A. Kvit, S. Kaskel and G. Yushin, *ACS Nano*, 2010, **4**, 1337–1344.

233 C. Liu, F. Li, L. P. Ma and H. M. Cheng, *Adv. Mater.*, 2010, **22**, E28.

234 J. R. Miller, *IEEE Electr. Insul. Mag.*, 2010, **26**, 40–47.

235 P. Simon and Y. Gogotsi, *Nat. Mater.*, 2008, **7**, 845–854.

236 E. Frackowiak, *Phys. Chem. Chem. Phys.*, 2007, **9**, 1774–1785.

237 P. J. Hall, M. Mirzaeian, S. I. Fletcher, F. B. Sillars, A. J. R. Rennie, G. O. Shitta-Bey, G. Wilson, A. Cruden and R. Carter, *Energy Environ. Sci.*, 2010, **3**, 1238–1251.

238 C. Liu, F. Li, L. P. Ma and H. M. Cheng, *Adv. Mater.*, 2010, **22**, E28–E62.

239 C. Peng, S. W. Zhang, D. Jewell and G. Z. Chen, *Prog. Nat. Sci.*, 2008, **18**, 777–788.

240 R. Kotz and M. Carlen, *Electrochim. Acta*, 2000, **45**, 2483–2498.

241 Y. H. Kim, in *Electronic Component News*, 2002.

242 K. Wang, J. Y. Huang and Z. X. Wei, *J. Phys. Chem. C*, 2010, **114**, 8062–8067.

243 Y. Y. Gao, S. L. Chen, D. X. Cao, G. L. Wang and J. L. Yin, *J. Power Sources*, 2010, **195**, 1757–1760.

244 M. J. Deng, F. L. Huang, I. W. Sun, W. T. Tsai and J. K. Chang, *Nanotechnology*, 2009, **20**, 175602–175606.

245 R. Tummala, R. K. Guduru and P. S. Mohanty, *J. Power Sources*, 2012, **209**, 44–51.

246 J. Chmiola, G. Yushin, Y. Gogotsi, C. Portet, P. Simon and P. L. Taberna, *Science*, 2006, **313**, 1760–1763.

247 O. Barbieri, M. Hahn, A. Herzog and R. Kotz, *Carbon*, 2005, **43**, 1303–1310.

248 J. Biener, M. Stadermann, M. Suss, M. A. Worsley, M. M. Biener, K. A. Rose and T. F. Baumann, *Energy Environ. Sci.*, 2011, **4**, 656–667.

249 J. Liu, G. Z. Cao, Z. G. Yang, D. H. Wang, D. Dubois, X. D. Zhou, G. L. Graff, L. R. Pederson and J. G. Zhang, *ChemSusChem*, 2008, **1**, 676–697.

250 L. L. Zhang, R. Zhou and X. S. Zhao, *J. Mater. Chem.*, 2010, **20**, 5983–5992.

251 A. F. Burke, *Proc. IEEE*, 2007, **95**, 806–820.

252 V. V. N. Obreja, *Physica E*, 2008, **40**, 2596–2605.

253 B. E. Conway, *Electrochemical supercapacitors: scientific fundamentals and technological applications*, Plenum Press, 1999.

254 A. Garcia-Gomez, P. Miles, T. A. Centeno and J. M. Rojo, *Electrochim. Acta*, 2010, **55**, 8539–8544.

255 E. G. Calvo, C. O. Ania, L. Zubizarreta, J. A. Menendez and A. Arenillas, *Energy Fuels*, 2010, **24**, 3334–3339.

256 A. Szczurek, K. Jurewicz, G. Amaral-Labat, V. Fierro, A. Pizzi and A. Celzard, *Carbon*, 2010, **48**, 3874–3883.

257 M. Inagaki, H. Konno and O. Tanaike, *J. Power Sources*, 2010, **195**, 7880–7903.

258 J. Lee, J. Kim and T. Hyeon, *Adv. Mater.*, 2006, **18**, 2073–2094.

259 K. Matsuoka, Y. Yamagishi, T. Yamazaki, N. Setoyama, A. Tomita and T. Kyotani, *Carbon*, 2005, **43**, 876–879.

260 A. B. Fuertes, G. Lota, T. A. Centeno and E. Frackowiak, *Electrochim. Acta*, 2005, **50**, 2799–2805.

261 H. Xu, Q. M. Gao, H. L. Guo and H. L. Wang, *Microporous Mesoporous Mater.*, 2010, **133**, 106–114.

262 Y. Gogotsi, A. Nikitin, H. H. Ye, W. Zhou, J. E. Fischer, B. Yi, H. C. Foley and M. W. Barsoum, *Nat. Mater.*, 2003, **2**, 591–594.

263 V. Presser, M. Heon and Y. Gogotsi, *Adv. Funct. Mater.*, 2011, **21**, 810–833.

264 M. Rose, E. Kockrick, I. Senkovska and S. Kaskel, *Carbon*, 2010, **48**, 403–407.

265 R. Dash, J. Chmiola, G. Yushin, Y. Gogotsi, G. Laudisio, J. Singer, J. Fischer and S. Kucheyev, *Carbon*, 2006, **44**, 2489–2497.

266 J. Chmiola, G. Yushin, R. Dash and Y. Gogotsi, *J. Power Sources*, 2006, **158**, 765–772.

267 V. Presser, L. F. Zhang, J. J. Niu, J. McDonough, C. Perez, H. Fong and Y. Gogotsi, *Adv. Energy Mater.*, 2011, **1**, 423–430.

268 F. Wu and B. Xu, *New Carbon Mater.*, 2006, **21**, 176–184.

269 G. Lota, K. Fic and E. Frackowiak, *Energy Environ. Sci.*, 2011, **4**, 1592–1605.

270 K. H. An, W. S. Kim, Y. S. Park, Y. C. Choi, S. M. Lee, D. C. Chung, D. J. Bae, S. C. Lim and Y. H. Lee, *Adv. Mater.*, 2001, **13**, 497–500.

271 C. G. Liu, H. T. Fang, F. Li, M. Liu and H. M. Cheng, *J. Power Sources*, 2006, **160**, 758–761.

272 A. B. Fuertes, F. Pico and J. M. Rojo, *J. Power Sources*, 2004, **133**, 329–336.

273 B. J. Yoon, S. H. Jeong, K. H. Lee, H. S. Kim, C. G. Park and J. H. Han, *Chem. Phys. Lett.*, 2004, **388**, 170–174.

274 Z. P. Huang, J. W. Wu, Z. F. Ren, J. H. Wang, M. P. Siegal and P. N. Provencio, *Appl. Phys. Lett.*, 1998, **73**, 3845–3847.

275 E. Frackowiak and F. Beguin, *Carbon*, 2001, **39**, 937–950.

276 C. M. Niu, E. K. Sichel, R. Hoch, D. Moy and H. Tennent, *Appl. Phys. Lett.*, 1997, **70**, 1480–1482.

277 A. G. Pandolfo and A. F. Hollenkamp, *J. Power Sources*, 2006, **157**, 11–27.

278 P. Azais, L. Duclaux, P. Florian, D. Massiot, M. A. Lillo-Rodenas, A. Linares-Solano, J. P. Peres, C. Jehoulet and F. Beguin, *J. Power Sources*, 2007, **171**, 1046–1053.

279 A. K. Shukla, S. Sampath and K. Vijayamohanan, *Curr. Sci. India*, 2000, **79**, 1656–1661.

280 D. N. Futaba, K. Hata, T. Yamada, T. Hiraoka, Y. Hayamizu, Y. Kakudate, O. Tanaike, H. Hatori, M. Yumura and S. Iijima, *Nat. Mater.*, 2006, **5**, 987–994.

281 C. S. Du, J. Yeh and N. Pan, *Nanotechnology*, 2005, **16**, 350–353.

282 L. J. Gao, A. P. Peng, Z. Y. Wang, H. Zhang, Z. J. Shi, Z. N. Gu, G. P. Cao and B. Z. Ding, *Solid State Commun.*, 2008, **146**, 380–383.

283 C. Emmenegger, J. M. Bonard, P. Mauron, P. Sudan, A. Lepora, B. Grobety, A. Zuttel and L. Schlapbach, *Carbon*, 2003, **41**, 539–547.

284 S. Dorfler, I. Felhosi, I. Kek, T. Marek, H. Althues, S. Kaskel and L. Nyikos, *J. Power Sources*, 2012, **208**, 426–433.

285 M. Kaempgen, J. Ma, G. Gruner, G. Wee and S. G. Mhaisalkar, *Appl. Phys. Lett.*, 2007, **90**, 264104–264105.

286 M. D. Stoller, S. J. Park, Y. W. Zhu, J. H. An and R. S. Ruoff, *Nano Lett.*, 2008, **8**, 3498–3502.

287 S. R. C. Vivekchand, C. S. Rout, K. S. Subrahmanyam, A. Govindaraj and C. N. R. Rao, *J. Chem. Sci.*, 2008, **120**, 9–13.

288 A. P. Yu, I. Roes, A. Davies and Z. W. Chen, *Appl. Phys. Lett.*, 2010, **96**, 253105.

289 Y. Wang, Z. Q. Shi, Y. Huang, Y. F. Ma, C. Y. Wang, M. M. Chen and Y. S. Chen, *J. Phys. Chem. C*, 2009, **113**, 13103–13107.

290 C. G. Liu, Z. N. Yu, D. Neff, A. Zhamu and B. Z. Jang, *Nano Lett.*, 2010, **10**, 4863–4868.

291 Q. Cheng, J. Tang, J. Ma, H. Zhang, N. Shinya and L. C. Qin, *Phys. Chem. Chem. Phys.*, 2011, **13**, 17615–17624.

292 S. Y. Yang, K. H. Chang, H. W. Tien, Y. F. Lee, S. M. Li, Y. S. Wang, J. Y. Wang, C. C. M. Ma and C. C. Hu, *J. Mater. Chem.*, 2011, **21**, 2374–2380.

293 G. A. Snook, P. Kao and A. S. Best, *J. Power Sources*, 2011, **196**, 1–12.

294 R. K. Sharma, A. C. Rastogi and S. B. Desu, *Electrochem. Commun.*, 2008, **10**, 268–272.

295 R. Liu, S. Il Cho and S. B. Lee, *Nanotechnology*, 2008, **19**, 215710–215717.

296 W. Dmowski, T. Egami, K. E. Swider-Lyons, C. T. Love and D. R. Rolison, *J. Phys. Chem. B*, 2002, **106**, 12677–12683.

297 X. Y. Lang, A. Hirata, T. Fujita and M. W. Chen, *Nat. Nanotechnol.*, 2011, **6**, 232–236.

298 Z. Chen, V. Augustyn, J. Wen, Y. W. Zhang, M. Q. Shen, B. Dunn and Y. F. Lu, *Adv. Mater.*, 2011, **23**, 791.

299 W. H. Shi, J. X. Zhu, D. H. Sim, Y. Y. Tay, Z. Y. Lu, X. J. Zhang, Y. Sharma, M. Srinivasan, H. Zhang, H. H. Hng and Q. Y. Yan, *J. Mater. Chem.*, 2011, **21**, 3422–3427.

300 H. T. Liu, P. He, Z. Y. Li, Y. Liu and J. H. Li, *Electrochim. Acta*, 2006, **51**, 1925–1931.

301 A. W. C. van den Berg and C. O. Arean, *Chem. Commun.*, 2008, 668–681.

302 J. Yang, A. Sudik, C. Wolverton and D. J. Siegel, *Chem. Soc. Rev.*, 2010, **39**, 656–675.

303 J. Sculley, D. Q. Yuan and H. C. Zhou, *Energy Environ. Sci.*, 2011, **4**, 2721–2735.

304 W. Grochala and P. P. Edwards, *Chem. Rev.*, 2004, **104**, 1283–1315.

305 T. P. McNicholas, A. M. Wang, K. O'Neill, R. J. Anderson, N. P. Stadie, A. Kleinhammes, P. Parilla, L. Simpson,

3170 | *Chem. Soc. Rev.*, 2013, **42**, 3127–3171

This journal is © The Royal Society of Chemistry 2013

C. C. Ahn, Y. Q. Wang, Y. Wu and J. Liu, *J. Phys. Chem. C*, 2010, **114**, 13902–13908.

306 C. Guan, K. Wang, C. Yang and X. S. Zhao, *Microporous Mesoporous Mater.*, 2009, **118**, 503–507.

307 K. S. Xia, Q. M. Gao, C. D. Wu, S. Q. Song and M. L. Ruan, *Carbon*, 2007, **45**, 1989–1996.

308 Z. X. Yang, Y. D. Xia and R. Mokaya, *J. Am. Chem. Soc.*, 2007, **129**, 1673–1679.

309 B. Panella, M. Hirscher and S. Roth, *Carbon*, 2005, **43**, 2209–2214.

310 A. Feaver and G. Z. Cao, *Carbon*, 2006, **44**, 590–593.

311 K. M. Thomas, *Catal. Today*, 2007, **120**, 389–398.

312 A. Chambers, C. Park, R. T. K. Baker and N. M. Rodriguez, *J. Phys. Chem. B*, 1998, **102**, 4253–4256.

313 A. C. Dillon, K. M. Jones, T. A. Bekkedahl, C. H. Kiang, D. S. Bethune and M. J. Heben, *Nature*, 1997, **386**, 377–379.

314 Q. Y. Wang and J. K. Johnson, *J. Phys. Chem. B*, 1999, **103**, 277–281.

315 A. Zuttel, *Naturwissenschaften*, 2004, **91**, 157–172.

316 P. Kowalczyk, R. Holyst, M. Terrones and H. Terrones, *Phys. Chem. Chem. Phys.*, 2007, **9**, 1786–1792.

317 R. Strobel, J. Garche, P. T. Moseley, L. Jorissen and G. Wolf, *J. Power Sources*, 2006, **159**, 781–801.

318 H. G. Schimmel, G. J. Kearley, M. G. Nijkamp, C. T. Visserl, K. P. de Jong and F. M. Mulder, *Chem.–Eur. J.*, 2003, **9**, 4764–4770.

319 L. Zhou, Y. P. Zhou and Y. Sun, *Int. J. Hydrogen Energy*, 2004, **29**, 319–322.

320 A. Zuttel, P. Sudan, P. Mauron, T. Kiyobayashi, C. Emmenegger and L. Schlapbach, *Int. J. Hydrogen Energy*, 2002, **27**, 203–212.

321 H. Kabbour, T. F. Baumann, J. H. Satcher, A. Saulnier and C. C. Ahn, *Chem. Mater.*, 2006, **18**, 6085–6087.

322 G. Srinivas, Y. W. Zhu, R. Piner, N. Skipper, M. Ellerby and R. Ruoff, *Carbon*, 2010, **48**, 630–635.

323 K. S. Subrahmanyam, S. R. C. Vivekchand, A. Govindaraj and C. N. R. Rao, *J. Mater. Chem.*, 2008, **18**, 1517–1523.

324 M. Pumera, *Energy Environ. Sci.*, 2011, **4**, 668–674.

325 H. Lee, J. Ihm, M. L. Cohen and S. G. Louie, *Nano Lett.*, 2010, **10**, 793–798.

326 K. L. Lim, H. Kazemian, Z. Yaakob and W. R. W. Daud, *Chem. Eng. Technol.*, 2010, **33**, 213–226.

327 J. X. Dong, X. Y. Wang, H. Xu, Q. Zhao and J. P. Li, *Int. J. Hydrogen Energy*, 2007, **32**, 4998–5004.

328 H. Furukawa, N. Ko, Y. B. Go, N. Aratani, S. B. Choi, E. Choi, A. O. Yazaydin, R. Q. Snurr, M. O'Keeffe, J. Kim and O. M. Yaghi, *Science*, 2010, **329**, 424–428.

329 S. Q. Ma and H. C. Zhou, *Chem. Commun.*, 2010, **46**, 44–53.

330 F. Vilela, K. Zhang and M. Antonietti, *Energy Environ. Sci.*, 2012, **5**, 7819–7832.

331 N. B. McKeown, B. Gahnem, K. J. Msayib, P. M. Budd, C. E. Tattershall, K. Mahmood, S. Tan, D. Book, H. W. Langmi and A. Walton, *Angew. Chem., Int. Ed.*, 2006, **45**, 1804–1807.

332 N. B. McKeown and P. M. Budd, *Macromolecules*, 2010, **43**, 5163–5176.

333 B. S. Ghanem, K. J. Msayib, N. B. McKeown, K. D. M. Harris, Z. Pan, P. M. Budd, A. Butler, J. Selbie, D. Book and A. Walton, *Chem. Commun.*, 2007, 67–69.

334 C. Z. Wu and H. M. Cheng, *J. Mater. Chem.*, 2010, **20**, 5390–5400.

335 S. Cahen, J. B. Eymery, R. Janot and J. M. Tarascon, *J. Power Sources*, 2009, **189**, 902–908.

336 L. Li, X. Yao, C. H. Sun, A. J. Du, L. N. Cheng, Z. H. Zhu, C. Z. Yu, J. Zou, S. C. Smith, P. Wang, H. M. Cheng, R. L. Frost and G. Q. M. Lu, *Adv. Funct. Mater.*, 2009, **19**, 265–271.

337 A. F. Gross, J. J. Vajo, S. L. Van Atta and G. L. Olson, *J. Phys. Chem. C*, 2008, **112**, 5651–5657.

338 A. Feaver, S. Sepehri, P. Shamberger, A. Stowe, T. Autrey and G. Z. Cao, *J. Phys. Chem. B*, 2007, **111**, 7469–7472.

339 S. Sepehri, B. B. Garcia and G. Z. Cao, *J. Mater. Chem.*, 2008, **18**, 4034–4037.

340 A. Gutowska, L. Y. Li, Y. S. Shin, C. M. M. Wang, X. H. S. Li, J. C. Linehan, R. S. Smith, B. D. Kay, B. Schmid, W. Shaw, M. Gutowski and T. Autrey, *Angew. Chem., Int. Ed.*, 2005, **44**, 3578–3582.

341 H. Kim, A. Karkamkar, T. Autrey, P. Chupas and T. Proffen, *J. Am. Chem. Soc.*, 2009, **131**, 13749–13755.

This journal is © The Royal Society of Chemistry 2013

Chem. Soc. Rev., 2013, **42**, 3127–3171 | **3171**